Branched actin networks in dendritic cell biology

by

Alexander Leithner

April, 2018

A thesis presented to the
Graduate School
of the
Institute of Science and Technology Austria, Klosterneuburg, Austria
in partial fulfillment of the requirements
for the degree of
Doctor of Philosophy

The dissertation of Alexander Leithner, titled *Branched actin networks in dendritic cell biology*, is approved by:

Supervisor: Prof. Dr. **Michael Sixt**, IST Austria, Klosterneuburg, Austria

Signature: ______________________________________

Committee Member: Prof. Dr. **Daria Siekhaus**, IST Austria, Klosterneuburg, Austria

Signature: ______________________________________

Committee Member: Prof. Dr. **Federica Benvenuti**, International Centre for Genetic Engineering and Biotechnology, Trieste, Italy

Signature: ______________________________________

Exam Chair: Prof. Dr. **Simon Hippenmeyer**, IST Austria, Klosterneuburg, Austria

Signature: ______________________________________

I hereby declare that this dissertation is my own work and that it does not contain other people’s work without this being so stated; this thesis does not contain my previous work without this being stated, and the bibliography contains all the literature that I used in writing the dissertation.

I declare that this is a true copy of my thesis, including any final revisions, as approved by my thesis committee, and that this thesis has not been submitted for a higher degree to any other university or institution.

I certify that any republication of materials presented in this thesis has been approved by the relevant publishers and co-authors.

Signature: ______________________

Alexander Leithner

April 11, 2018

Abstract

In the here presented thesis, we explore the role of branched actin networks in cell migration and antigen presentation, the two most relevant processes in dendritic cell biology.

Branched actin networks construct lamellipodial protrusions at the leading edge of migrating cells. These are typically seen as adhesive structures, which mediate force transduction to the extracellular matrix that leads to forward locomotion. We ablated Arp2/3 nucleation promoting factor WAVE in DCs and found that the resulting cells lack lamellipodial protrusions. Instead, depending on the maturation state, one or multiple filopodia were formed. By challenging these cells in a variety of migration assays we found that lamellipodial protrusions are dispensable for the locomotion of leukocytes and actually dampen the speed of migration. However, lamellipodia are critically required to negotiate complex environments that DCs experience while they travel to the next draining lymph node. Taken together our results suggest that leukocyte lamellipodia have rather a sensory- than a force transducing function.

Furthermore, we show for the first time structure and dynamics of dendritic cell F-actin at the immunological synapse with naïve T cells. Dendritic cell F-actin appears as dynamic foci that are nucleated by the Arp2/3 complex. WAVE ablated dendritic cells show increased membrane tension, leading to an altered ultrastructure of the immunological synapse and severe T cell priming defects. These results point towards a previously unappreciated role of the cellular mechanics of dendritic cells in T cell activation.

Additionally, we present a novel cell culture based system for the differentiation of dendritic cells from conditionally immortalized hematopoietic precursors. These precursor cells are genetically tractable via the CRISPR/Cas9 system while they retain their ability to differentiate into highly migratory dendritic cells and other immune cells. This will foster the study of all aspects of dendritic cell biology and beyond.

Acknowledgments

First of all I would like to thank Michael Sixt for giving me the opportunity to work in his group and for his support throughout the years. He is a truly inspiring person and the best boss one can imagine. I would also like to thank all current and past members of the Sixt group for their help and the great working atmosphere in the lab. It is a true privilege to work with such a bright, funny and friendly group of people and I'm proud that I could be part of it. Furthermore, I would like to say 'thank you' to Daria Siekhaus for all the meetings and discussion we had throughout the years and to Federica Benvenuti for being part of my committee. I am also grateful to Jack Merrin in the nanofabrication facility and all the people working in the bioimaging-, the electron microscopy- and the preclinical facilities.

I dedicate this work to my future wife Isabella and our wonderful daughter Pauline.

I love you with all my heart.

About the Author

Alexander Leithner started his academic career with his bachelor studies in genetics and microbiology at the University of Vienna. He continued at the University of Vienna for an MSc in genetics and developmental biology. During his master studies he was working as a tutor for laboratory courses at the Vienna University of Applied Sciences and did an internship at the Stowers Institute for Medical Research in Kansas City, USA.

Alexander joined IST Austria in September 2012 and joined the laboratory of Prof. Michael Sixt. He was working on the research projects: ‘Branched actin networks in dendritic cell migration’, ‘Establishment of genome engineering in hematopoietic precursor cells’ and ‘Dendritic cell branched F-actin in immunological synapse formation’ and published results of the first two in *Nature Cell Biology* and the *European Journal of Immunology* respectively. Additionally, he provided help in several other projects and appears on several other publications. During his PhD, Alexander presented his work at the *International meeting of the German society for cell biology* 2014 in Regensburg, Germany; the *4th European Congress of Immunology* 2015 in Vienna, Austria and the conference *Imaging the immune system* 2016 at the Weizmann Institute, Israel. Furthermore, he participated in the *Actin dynamics* summer school 2014 in Regensburg, Germany and the workshop *Advanced electron microscopy for cell biologists* 2017 at the EMBL in Heidelberg, Germany.

List of Publications

Brown, M., Assen, FP., Leithner, A., Abe, J., Schachner, H., Asfour, G., Bago-Horvath, Z., Stein, JV., Uhrin, P., Sixt, M., Kerjaschki, D., 2018. **Lymph node vessels provide exit routes for metastatic tumor cell dissemination in mice.** *Science* 359,1408-1411. doi: 10.1126/science.aal3662

Leithner, A., Renkawitz, J., De Vries, I., Hauschild, R., Haecker, H., Sixt, M., 2018. **Fast and efficient genetic engineering of hematopoietic precursor cells for the study of dendritic cell migration.** *European Journal of Immunology* 0:1-4. doi: 10.1002/eji.201747358

Vaahtomeri, K., Brown, M., Hauschild, R., De Vries, I., Leithner, A., Mehling, M., Kaufmann, W.A., Sixt, M., 2017. **Locally Triggered Release of the Chemokine CCL21 Promotes Dendritic Cell Transmigration across Lymphatic Endothelia.** *Cell Reports* 19, 902–909. doi:10.1016/j.celrep.2017.04.027

Schwarz, J., Bierbaum, V., Vaahtomeri, K., Hauschild, R., Brown, M., de Vries, I., Leithner, A., Reversat, A., Merrin, J., Tarrant, T., Bollenbach, T., Sixt, M., 2017. **Dendritic Cells Interpret Haptotactic Chemokine Gradients in a Manner Governed by Signal-to-Noise Ratio and Dependent on GRK6.** *Current Biology* 27, 1314–1325. doi:10.1016/j.cub.2017.04.004

Leithner, A.*, Eichner, A.*, Müller, J., Reversat, A., Brown, M., Schwarz, J., Merrin, J., De Gorter, D.J.J., Schur, F., Bayerl, J., De Vries, I., Wieser, S., Hauschild, R., Lai, F.P.L., Moser, M., Kerjaschki, D., Rottner, K., Small, J.V., Stradal, T.E.B., Sixt, M., 2016. **Diversified actin protrusions promote environmental exploration but are dispensable for locomotion of leukocytes.** *Nature Cell Biology* 18, 1253–1259. doi:10.1038/ncb3426 *… contributed equally

Leithner, A., Merrin, J., Reversat, A., Sixt, M., 2016. **Geometrically complex microfluidic devices for the study of cell migration.** *Nature protocol exchange.* doi:10.1038/protex.2016.063

Table of Contents

1 List of Figures

Figures in 'Diversified actin protrusion promote environmental exploration but are dispensable for locomotion of leukocytes'

List of Symbols/Abbreviations

ADAP	adhesion- and degranulation-promoting adaptor protein
ADP	adenosindiphosphat
ALB	artificial lipid bilayer
APC	antigen presenting cell
Arp2/3	actin-related protein 2 and 3
ATP	adenosintriphosphat
BM	bone marrow
c/p/dSMAC	central/peripheral/distal supramolecular activation cluster
Cas	CRISPR associated
CCL19/21	C-C chemokine ligand 19/21
CCR7	C-C chemokine receptor 7
CD	cluster of differentiation
CP	capping protein
CRIB	Cdc42 and Rac interactive binding
CRISPR	clustered regularly interspersed short palindromic repeats
crRNA	CRISPR RNA
DAG	diacylglycerol
DSB	double strand break
EGF	epidermal growth factor
ELC	essential light chain
ER	endoplasmic reticulum
ES cell	embryonic stem cell
F-actin	filamentous Actin
FA	focal adhesion
FH	formin homology domain
Flt3	fms like tyrosine kinase 3
G-actin	globular Actin
GBD	GTPase-binding domain

GDP	guanosindiphosphat
GEF	guanine exchange factor
GM-CSF	granulocyte-macrophage colony stimulating factor
GPCR	G-protein coupled receptor
gRNA	guide RNA
GTP	guanosintriphosphat
HDR	homology directed repair
Hoxb8	homeobox transcription factor b8
i-/mDC	immature/mature dendritic cell
ICAM1	intercellular adhesion molecule 1
IL-3	interleukin 3
IP_3	inositol trisphosphate
IS	immunological synapse
ITAM	immunoreceptor tyrosine-based activation motif
LAT	linker for activation of T cells
Lck	lymphocyte-specific protein tyrosine kinase
LFA-1	lymphocyte function-associated antigen 1
LPS	lipopolysaccharide
MAPK	mitogen-activated protein kinase
mDia1	mammalian diaphanous related formin 1
MHC	Major histocompatibility complex
MLCK	myosin light chain kinase
MP-IVM	multiphoton-intravital microscopy
MTOC	microtubule organizing center
Nck1	non-catalytic region of tyrosine kinase adaptor protein 1
NFAT	nuclear factor of activated T cells
NHEJ	non-homologous end joining
NK-κB	nuclear factor kappa-light-chain-enhancer of activated B cells
NMII	non-muscle myosin II
NPF	nucleation promoting factor

PAM	protospacer adjacent motif
PDGF	platelet-derived growth factor
PH	plexstrin homology
PI3K	Phosphatidylinositol-3 kinase
PIP_2	phosphatidylinositol 4,5-bishosphate
PIP_3	phosphatidylinositol-3,4,5- triphosphate
PKCΦ	protein kinase C-theta
PLCγ1	Phospholipase C, gamma 1
PRD	proline rich domain
PSC	proximal signaling complex
PTEN	Phosphatase and tensin homolog
RLC	regulatory light chain
ROCK	Rho-associated protein kinase
SH3	SRC homology 3 domain
SHD	SCAR homology domain
SLP-76	SH2 domain–containing leukocyte phospho-protein of 76 kDa
SMIFH2	small molecule inhibitor of Formin homology 2 domain
SV40	simian-virus 40
TCR	T cell receptor
TCR-MC	T cell receptor microcluster
TF	transcription factor
TIRF	total internal reflection fluorescence
tracrRNA	trans-activating crRNA
VAMP	vesicle-associated membrane protein
VASP	vasodilator-stimulated phosphoprotein
Vav1	vav guanine nucleotide exchange factor 1
WASP	Wiskott-Aldrich syndrome protein
WAVE	WASP-family verprolin homologous protein
WH1	WASP homology 1
Zap-70	zeta-chain-associated protein kinase 70

α	alpha
β	beta
γ	gamma
δ	delta
ε	epsilon

2 Introduction

Dendritic cells (DCs) are sentinels of the innate immune system that serve as a pivotal link to the adaptive immune system. In their immature state, DCs reside in almost all tissues of the body where they are highly phagocytic and constantly sample their environment for antigens [1]. Upon antigen encounter, DCs start to mature and up-regulate the C-C chemokine receptor 7 (CCR7) that allows them to efficiently migrate along gradients of its ligands C-C chemokine ligand (CCL) 19 and 21 to the next draining lymph node [2]. Simultaneously phagocytosis ceases, antigen is processed and co-stimulatory molecules are up regulated. Once they arrive in the lymph node, DCs are highly competent to present antigen in the context of major histocompatibility complex (MHC) on their cell surface to the rare subset of T cells that express a suitable T cell receptor (TCR). Upon contact formation, DCs and T cells form an immunological synapse (IS) that leads to T cell activation, clonal expansion and eventually the mounting of an adaptive immune response (Fig.1) [1].

In the context of their role in the immune system **cell migration** and **antigen presentation** can be identified as two key properties of DCs. Actin polymerization stands at the base of both processes. Here, we focus on branched actin networks that not only construct sheet-like lamellipodia, implicated in migration but, which also have a role at the IS. To begin with, the basic properties, dynamics and structures of the actin cytoskeleton will be discussed. This will be followed by a more detailed discussion in the context of cell migration and immunological synapse formation in the respective chapters.

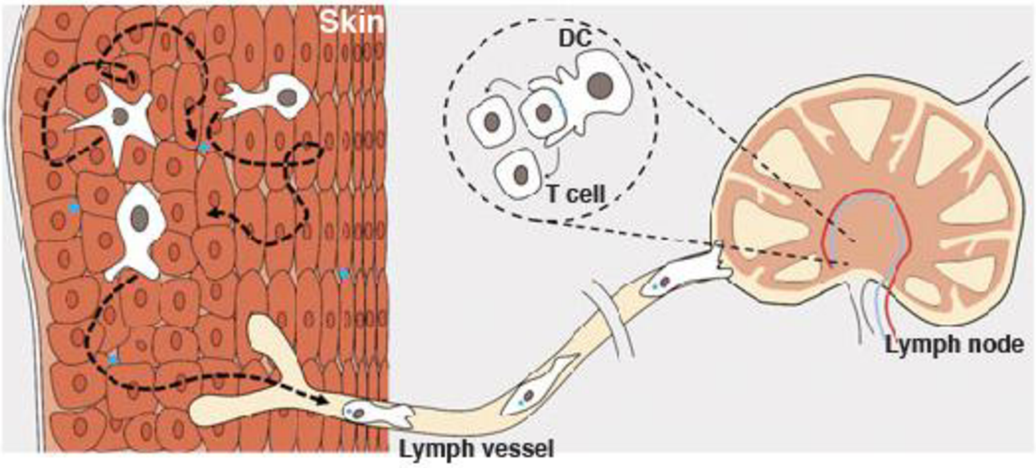

Figure 1. **Dendritic cells and their role in the immune system.** DCs in organs such as the skin constantly sample their environment for antigens (blue dots). Upon antigen encounter, DCs mature and migrate to lymph vessels to reach the next draining lymph node. There, antigen is presented to T cells with a matching T cell receptor, which eventually triggers an adaptive immune response. Modified after Heuze et al., 2013.

2.1 The actin cytoskeleton

Actin, a 42kDa globular ATP-binding monomer (G-actin) is the basic building block for the polymerization of double stranded, right-handed helical actin filaments (F-actin). Actin filaments have a polarity with a fast growing barbed- (+) and a slowly growing pointed (-) end, generated by the intrinsic polarity of G-actin. Above a critical concentration Actin-ATP monomers polymerize spontaneously and ATP is hydrolyzed to ADP (Fig.2A). In cells, the concentration of G-actin exceeds the critical concentration [3]. Consequently, the assembly and disassembly of F-actin and its dynamics has to be tightly regulated. Three highly interconnected modules, namely the *actin nucleation*, *actin severing* and *actin contraction* machinery, each defined by a set of proteins, ensure that at any given moment a cell can react to environmental cues by polymerizing or disassembling F-actin or by changing the properties of the actin network.

2.1.1 The actin nucleation machinery

To prevent spontaneous polymerization, G-actin is bound by the highly abundant actin monomer binding protein profilin at its barbed end, restricting polymerization to the barbed ends of filaments [4]. Additionally, it serves as a nucleotide exchange factor that exchanges adenosindiphosphat (ADP) with adenosintriphosphat (ATP) on actin monomers, thereby returning them to the polymerizable pool. Profilin bound G-actin only polymerizes through the activity of nucleation factors whose two most prominent classes are the actin-related protein 2 and 3 (Arp2/3), together with its nucleation promoting factors (NPFs), and formins. Although they strongly differ in their structure and function two common modules can be identified: (**1**) a module that responds to upstream receptor signaling by binding to signaling molecules such as phosphatidylinositol 4,5-bishosphate (PIP_2) or GTPases (e.g. Rac, Rho and Cdc42) and (**2**) a module that translates this signaling into actin polymerization. The function of Arp2/3 and formins will be discussed in the following sections in context of the characteristic structures they build, namely *lamellipodia* and *filopodia*.

2.1.1.1 Lamellipodia, branched actin networks and Arp2/3

Lamellipodia are thin, sheet-like structures typically found at the leading edge of migrating cells. Their underlying structure is a dense, branched actin network that is constructed by Arp2/3. Arp2/3 is a seven-subunit complex that consists of the proteins Arp2 and 3 and five other proteins named ARPC1, ARPC2, ARPC3, ARPC4 and ARPC5. It binds to the side of existing filaments where it branches of a new actin filament at a 70° angle with respect to the pre-existing filament. Arp2 and 3 are structurally highly similar to G-actin and simulate an actin dimer that is thermodynamically favorable to initiate nucleation (Fig.2A) [5].

However, Arp2/3 on its own is inactive and requires the activity of nucleation promoting factors (NPFs) of the Wiskott-Aldrich syndrome protein (WASP) superfamily whose most prominent members are WASP and WASP-family verprolin homologous protein (SCAR/WAVE). All members of the family share a similar domain structure with a C-terminal V region that binds profilin-actin monomers and a CA region that binds Arp2/3, providing a platform for actin polymerization [6].

In contrast to the conserved C-terminal domain the N-terminal regulatory domains differ between members of the WASP superfamily. However, their common function is to integrate upstream signaling and to link to adaptor proteins that confine Arp2/3-NPF activity to the plasma membrane. The N-terminal domain of WASP consist of a WASP homology 1 domain (WH1), a basic region, a Cdc42 and Rac interactive binding (CRIB) region, a GTPase-binding domain (GBD) and a proline rich domain (PRD) [6]. Under resting conditions, WASP is folded in an auto-inhibitory state by interaction of the VCA region with GBD. In response to upstream signaling Cdc42 binds to GBD, the protein unfolds and the VCA region becomes accessible for Arp2/3 and G-actin. This activation can be reinforced by PIP_2 or SRC homology 3 domain (SH3) containing proteins that bind to the basic region or the PRD respectively.

In contrast, the N-terminus of WAVE consists of a SCAR homology domain (SHD), a basic region and a PRD. WAVE does not appear as a monomer but together with four other proteins, namely BRICK1, ABI1, NAP1 and SRA1, forming the pentameric WAVE complex. Inhibition under resting conditions is mediated by binding of ABI1 and BRICK to the VCA. Upon binding of Rac1 to SRA1 the WAVE complex becomes activated, which again can be reinforced by binding of other factors to SH3 or PRD.

To build branched actin networks, Arp2/3 in concert with an NPF binds to an already existing filament and initiates actin polymerization on a new branch. However, in order to build dense networks, actin polymerization has to be limited to allow initiation of new branches. Therefore, actin filaments are soon bound by capping proteins (CPs) that prevent further polymerization, thereby allowing the cycle to start anew.

2.1.1.2 Filopodia, formins and parallel actin bundles

Filopodia are thin, spike-like protrusions that contain parallel bundles of actin filaments. Two non-exclusive mechanisms for their construction have been proposed. The first one proposes that Arp2/3 generated branches are not capped by CP but stabilized by vasodilator-stimulated phosphoprotein (VASP) that prevents capping. Linear filaments would then coalesce into a parallel bundle that is stabilized by the bundling protein Fascin [3]. The second model sees formin such as mammalian diaphanous related formin 1 (mDia1) as the prime constructor of parallel actin filaments. Formins appear as dimers, each consisting of an N-terminal regulatory-and a C-terminal active region. The N-terminal region binds to upstream signaling molecules such as GTPases and upon activation, recruits Formins to the plasma membrane. The active region consists of two formin homology domains (FH1 and FH2). FH1 contains binding sites for profilin-actin on a flexible, rope-like structure. The FH2 dimer is doughnut-shaped and wraps around- and moves with barbed ends of actin filaments (Fig.2A). There it stabilizes and protects the growing parallel filaments from CPs that are again bundled by Fascin [7].

2.1.2 The actin severing machinery

Actin filaments have to be disassembled and recycled to ensure constant availability of polymerizable G-actin to build new structures. Upon polymerization, ATP on actin is hydrolyzed to ADP. Cofilin, a depolymerization factor, binds to ADP-actin where it mediates the release of actin monomers from the pointed end. Additionally, it severs actin filaments, which increases the number of available branched ends for new rounds of polymerization.

2.1.3 The actin contraction machinery

Non-muscle myosin II (NMII) mediates contractility of the actin cytoskeleton. It consists of three pairs of molecules: two heavy chains of 230kDa, two essential light chains (ELC) of 17kDa that stabilize the heavy chain and two regulatory light chains (RLC) of 20kDa that regulate the activity of NMII through their phosphorylation. The two heavy chains form globular head domains that have ATPase activity and contain binding sites for ATP and actin (Fig.2B). Binding sites for RLC and ELC are located in the neck region, which is followed by a long coiled-coil rod domain that mediates dimerization and association with other NMII molecules to form bipolar filaments whose globular domains point in opposing directions (Fig.2C) [8]. NMII contracts actin filaments in the so-called ‘power stroke’ cycle. Upon ATP binding, actin bound NMII releases the actin filament and undergoes a conformational change in the head domain that bends it towards the barbed end of the actin filament. ATP is hydrolyzed to ADP and phosphate and myosin binds the actin filament. Upon phosphate release the power stroke is initiated, moving the head domain to its original position and releasing ADP so the cycle can start anew. Thereby, myosin moves toward the branched end of the actin filament while the actin filament moves in the direction of its pointed end. As a consequence, bipolar myosin filaments glide actin filaments past each other, leading to overall filament contraction [9]. NMII activity is regulated by phosphorylation of RLC by kinases such as myosin light chain kinase (MLCK) or Rho-associated protein kinase (ROCK), which increases the ATPase activity of NMII [8].

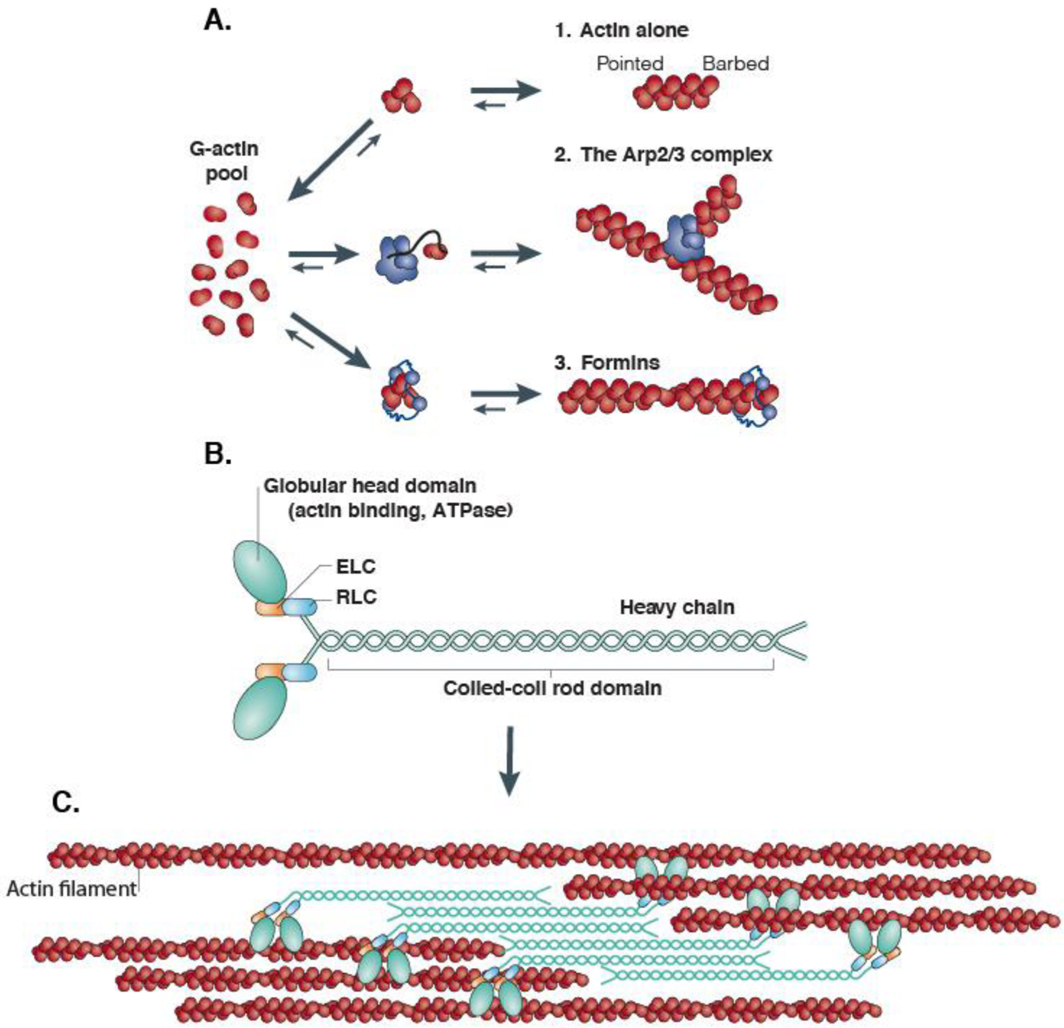

Figure 2. Actin assembly pathways and myosin filaments. (**A**) Above the critical concentration, G-actin assembles into bipolar filaments with a barbed- and a pointed end. In cells, G-actin is bound by profilin (not shown) to prevent spontaneous polymerization and is regulated by nucleation factors such as the Arp2/3 complex and Formins, which polymerize branched actin networks or linear filaments respectively. Modified after Goley and Welch, 2006. (**B**) Non-muscle myosin II consists of two heavy chains, two essential- and two regulatory light chains. Its globular head region binds actin and has ATPase activity while the coiled-coil rod domain mediates the (**C**) assembly of bipolar filaments that contract actin filaments. Modified after Vicente-Manzanares et al., 2009.

3 The role of leading edge protrusions in leukocyte cell migration

The ability of cells to migrate is key to a variety of biological processes such as immune responses, embryonic development, but also pathological processes like metastasis. Migrating cells are polarized and exhibit a clearly defined front and back, referred to as leading edge and uropod respectively. Underlying this morphological polarity is the non-uniform distribution of a set of molecules that has been mainly studied in *Dictyostelium* and neutrophils [10]. Downstream signaling of these molecules leads to actin polymerization at the front of the cell that pushes out the plasma membrane and generates protrusions in the form of lamellipodia and filopodia while myosin contracts the actin network at the back of the cell. In the typical model of cell migration the occurring forces are coupled to the extracellular environment via specific adhesions on the lamellipodium to achieve forward locomotion. However, this view has been recently challenged in DCs, which show unimpaired migration in the absence of specific adhesions [11] and we set out to resolve this controversy.

The following sections will give an overview of chemokine receptor signaling and the establishment of polarity. This will be followed by an overview of different modes of cell migration that will lead to the formulation of the aims of this study.

3.1 G-protein coupled receptor signaling and the establishment of polarity

Directed cell migration begins at the plasma membrane with binding of chemo attractants to their uniformly distributed respective receptors. In the case of leukocytes, these are G-protein coupled receptors (GPCRs), initiating guanosinediphosphat (GDP) to guanosintriphosphat (GTP) exchange on the trimeric G-protein. This leads to dissociation of the α- from the βγ subunit, which initiates downstream signaling [12]. Phosphatidylinositol-3 kinase (PI3K) and its antagonist Phosphatase and tensin homolog (PTEN), that acts as a phosphatidylinositol-3,4,5-trisphosphate 3-phosphatase, are segregated and accumulate at the future leading edge and uropod respectively. Thereby, PI3Ks product phosphatidylinositol-3,4,5-triphosphate (PIP_3) can locally accumulate in the plasma membrane where it recruits proteins that contain plexstrin homology (PH) domains such as protein kinase B or guanine exchange factors (GEFs). Additionally, WASP and WAVE are recruited as they contain PIP_3 binding domains. Furthermore, localized activation of GEFs at the future leading edge for the Rho GTPases Cdc42 and Rac in turn leads to activation of actin nucleation factors [13]. Taken together, these highly interconnected pathways lead to localized actin polarization and the formation of a leading edge that is maintained by feed-forward positive feedback loops [14]. At the same time the Rho GTPase Rho is confined to the back of the cell where it increases myosin contractility by phosphorylation of RLC via ROCK. Furthermore, Rho and Rac are mutually inhibitory, which maintains a clear front-back polarization.

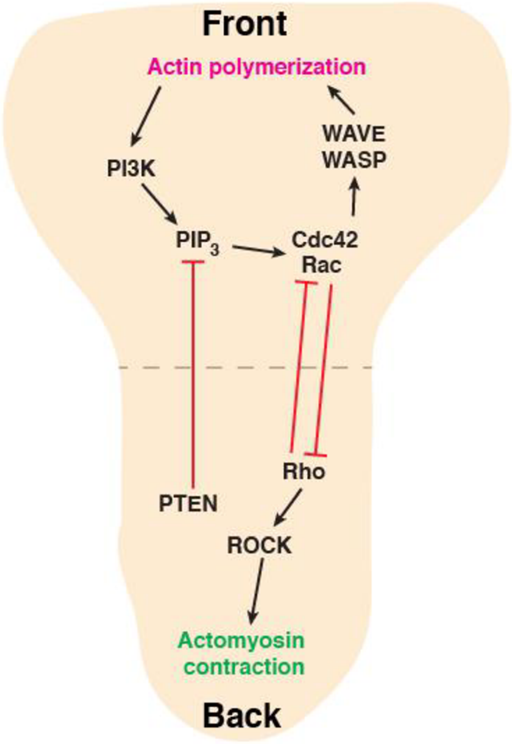

***Figure 3.* Simplified view of cellular polarity establishment in cell migration.** Upon chemo attractant receptor stimulation, PI3K and its agonist PTEN are segregated to the future front and back respectively. Thereby, PI3Ks product PIP_3 accumulates and leads to recruitment of Cdc42 and Rac. In turn, this leads to activation of WAVE and WASP that results in actin polymerization and leading edge formation. Rho is localized to the back of the cell where it mediates actomyosin contraction via ROCK. Activating and inhibiting feedback loops help to maintain front-back polarization.

3.2 A classic view on cell migration

The classic textbook view describes cell migration as a cyclic, multi-step process on a 2D substrate [15]. First, actin polymerizes against the plasma membrane, leading to lamellipodial *protrusion formation* in the front of the cell and retrograde actin flow towards the back. Next, *adhesions* to the environment are formed in the new protrusion by formation of focal adhesions (FAs), which are large assemblies of a variety of different molecules. At their core, transmembrane receptors of the integrin family mediate substrate adhesion through their extracellular domains. In mammals, 24 different integrin variants with different substrate specificity exist, assembled by heterodimer formation between 18 different α- and 8 different β subunits [16]. Their intracellular portion is bound by talin, vinculin and α-actinin that indirectly connect integrins to the actin cytoskeleton. Thereby, actin retrograde flow is coupled to the extracellular environment forming a molecular clutch [17]. Together with myosin contraction at the back, this leads to traction force on the substrate and forward *translocation* of the cell body. Finally, old adhesions at the back of the cell are resolved and the uropod is retracted before the next cycle starts.

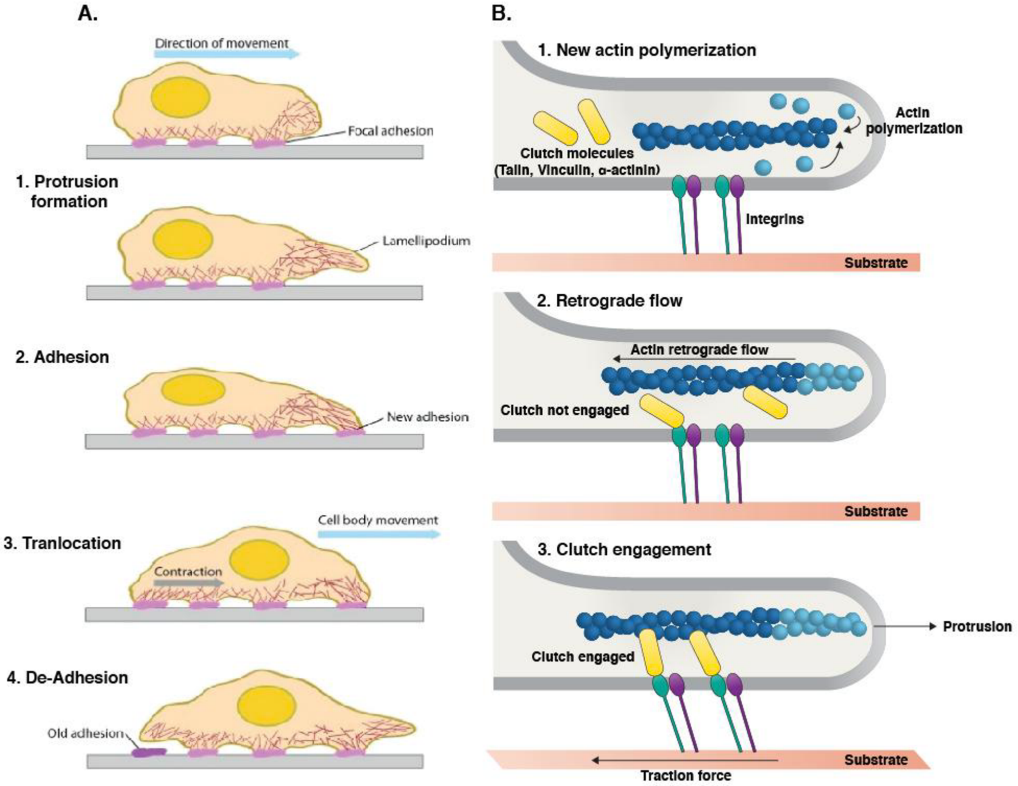

***Figure 4.* The classic protrusion-retraction cycle of 2D cell migration and the molecular clutch.** (**A**) Cell migration is a cyclic, multistep process that starts with lamellipodial protrusion formation, followed by focal adhesion formation. Contraction at the back of the cell leads to cell body translocation after which old adhesions at the back are resolved before the cycle starts anew. Modified after Ananthakrishnan and Ehrlicher, 2007. (**B**) Protrusion formation is achieved by coupling actin retrograde flow via the molecular clutch to substrate bound integrins. This leads to the occurrence of tractions forces and net membrane protrusion. Modified after Case and Waterman, 2015.

3.3 The lamellipodias role in cell migration

In the above-described model, the role of the lamellipodium is to mediate new substrate adhesions onto which force can be applied to propel the cell forward. To probe this model, different groups have inhibited Arp2/3 mediated branched actin polymerization in fibroblasts. Consequently, this leads to a drastic change in cell morphology that lacks lamellipodia but instead exhibits multiple filopodia. In one case, this leads to a reduction in migratory speed, persistence and defects in chemotaxis towards epidermal growth factor (EGF) [18]. In the other case, migratory speed is reduced but cells show intact chemotaxis towards platelet-derived growth factor (PDGF) while they are insufficient to interpret haptokinetic (surface immobilized) gradients [19]. The discrepancy between the two studies regarding chemotaxis could be resolved by the finding that Arp2/3 deficient cells secrete increased amount of growth factors. This perturbs chemotaxis towards EGF but not PDGF in closed migration chambers, suggesting that chemotaxis per se is Arp2/3 independent [20]. However, FAs show defects in morphology, dynamics and alignment along the axis of movement [19] and both studies report defects in cell spreading. Overall, these results are in line with a model of cell migration in which the lamellipodium is required to mediate substrate adhesion via FAs for force transduction.

However, amoeboid migrating cells such as leukocytes, are only weakly adhesive and form no FAs [21]. Strikingly, the migration of DCs in 3D environments has been shown to be completely independent of integrins [22] and force transduction is potentially achieved by unspecific intercalation of new protrusions with the environment, providing a footing while the back of the cell contracts [23].

3.4 Aims and initial status

The aim of this study is to clarify the role leading edge protrusions play in leukocyte migration with an emphasis on lamellipodia. As discussed before, the traditional view of lamellipodia as the site of integrin mediated adhesion assembly and force transduction was challenged by the observation that DCs show unimpaired migration in 3D environments in the absence of integrins. Hence, the role of lamellipodial protrusions in leukocyte migration requires clarification.

Following a loss of function approach, we decided to interfere with Arp2/3 dependent branched actin polymerization, which gives rise to lamellipodial protrusions. However, as Arp2/3 depletion leads to embryonic lethally [24], this poses a non-trivial challenge. Although drug inhibition is in principle possible, we decided against it to avoid ambiguous results that could be caused by incomplete Arp2/3 inhibition and aimed for a clear genetic approach. To this end, we decided not to interfere with Arp2/3 directly but with the NPF WAVE. More specifically, we employed a mouse model in which *hem1*, a version of the WAVE complex component Nap1 that is restricted to the hematopoietic system, is deleted [25]. Consequently, these mice are viable but lack WAVE dependent Arp2/3 mediated actin polymerization in leukocytes.

By challenging the resulting DCs in a variety of *in vitro* and *in vivo* assays we were able to draw important conclusions about the role of leading edge protrusions in cell migration.

3.5 **Results – *'Diversified actin protrusions promote environmental exploration but are dispensable for locomotion of leukocytes'*** *– publication in Nature Cell Biology, 2016.*

This work is a joint co-authorship with Alexander Eichner. I performed the experiments for Figures 1a & b; 2c; 3; 4e & f; 5e & f and Supplementary Figures 2D, E, F, G & H; 3A, B & D; 4B, C, D & E.
Additionally, I performed the data analysis for Figures 1d; 2g & h and Supplementary Figure 3C and put together the manuscript.

nature
cell biology

Diversified actin protrusions promote environmental exploration but are dispensable for locomotion of leukocytes

Alexander Leithner[1,8], Alexander Eichner[1,8], Jan Müller[1,2], Anne Reversat[1], Markus Brown[1,3], Jan Schwarz[1], Jack Merrin[1], David J. J. de Gorter[4], Florian Schur[2], Jonathan Bayerl[2], Ingrid de Vries[1], Stefan Wieser[1], Robert Hauschild[1], Frank P. L. Lai[5], Markus Moser[6], Dontscho Kerjaschki[3], Klemens Rottner[5,7], J. Victor Small[2], Theresia E. B. Stradal[4,5] and Michael Sixt[1,9]

Most migrating cells extrude their front by the force of actin polymerization. Polymerization requires an initial nucleation step, which is mediated by factors establishing either parallel filaments in the case of filopodia or branched filaments that form the branched lamellipodial network. Branches are considered essential for regular cell motility and are initiated by the Arp2/3 complex, which in turn is activated by nucleation-promoting factors of the WASP and WAVE families[1]. Here we employed rapid amoeboid crawling leukocytes and found that deletion of the WAVE complex eliminated actin branching and thus lamellipodia formation. The cells were left with parallel filaments at the leading edge, which translated, depending on the differentiation status of the cell, into a unipolar pointed cell shape or cells with multiple filopodia. Remarkably, unipolar cells migrated with increased speed and enormous directional persistence, while they were unable to turn towards chemotactic gradients. Cells with multiple filopodia retained chemotactic activity but their migration was progressively impaired with increasing geometrical complexity of the extracellular environment. These findings establish that diversified leading edge protrusions serve as explorative structures while they slow down actual locomotion.

The flat structure of lamellipodia is usually attributed to their surface adhesiveness, and transmembrane coupling of actin dynamics to substrate adhesions is considered to be the basis of the lamellipodium's role in locomotion[1]. Although interference with Arp2/3 activity consistently led to a loss of lamellipodial structures, the reported effects on actual cell motility are variable, with some cells retaining a certain locomotor activity, while others severely slow down or lose their ability to interpret gradients of guidance cues. A common theme of previous studies is that Arp2/3 controls the organization of adhesive structures and thereby alters motility[2–4]. Notably, most leukocytes are able to migrate in the absence of tight surface adhesions but still form prominent lamellipodia[5]. Hence, the topology of their cytoskeletal organization has a much more immediate impact on cell shape and possibly locomotion, raising the question of if and how lamellipodia contribute to low adhesive leukocyte migration. A prototypic example of rapidly migrating leukocytes is dendritic cells (DCs), which earned their name because of their veiled appearance. Especially in their activated state, these cells extend multiple membrane sheets, creating the lettuce-like appearance of a cell with numerous lamellipodia. DCs are highly migratory *in vivo* and in fibrillar three-dimensional (3D) environments their locomotion is independent of integrins[6]. DCs exist in two states: immature (iDCs) and mature (mDCs). Maturation is a terminal differentiation step triggered by microbial encounter. It is accompanied by substantial remodelling of the DCs' proteome and initiates rapid migration from peripheral tissues to the draining lymph node, where DCs present peripherally acquired antigen to recirculating T cells[7].

In this study we generate DCs from primary or transiently immortalized precursor cells[8]. Transient immortalization allowed us to introduce stable as well as transient genetic changes. First we dynamically mapped actin, Arp2/3 and nucleation-promoting factor

---

[1]Institute of Science and Technology Austria (IST Austria), am Campus 1, 3400 Klosterneuburg, Austria. [2]Institute for Molecular Biotechnology, Austrian Academy of Sciences, Dr. Bohr-Gasse 3, 1030 Vienna, Austria. [3]Clinical Department of Pathology, Medical University of Vienna, Währinger Gürtel 18-20, 1090 Vienna, Austria. [4]Institute for Molecular Cell Biology, University of Münster, Schlossplatz 5, 48149 Münster, Germany. [5]Helmholtz Centre for Infection Research, Inhoffenstrasse 7, 38124 Braunschweig, Germany. [6]Department of Molecular Medicine, Max Planck Institute of Biochemistry, 82152 Martinsried, Germany. [7]Division of Molecular Cell Biology, Zoological Institute, Technische Universität Braunschweig, Spielmannstrasse 7, 38106 Braunschweig, Germany. [8]These authors contributed equally to this work.
[9]Correspondence should be addressed to M.S. (e-mail: Sixt@ist.ac.at)

Received 14 October 2015; accepted 20 September 2016; published online 24 October 2016; DOI: 10.1038/ncb3426

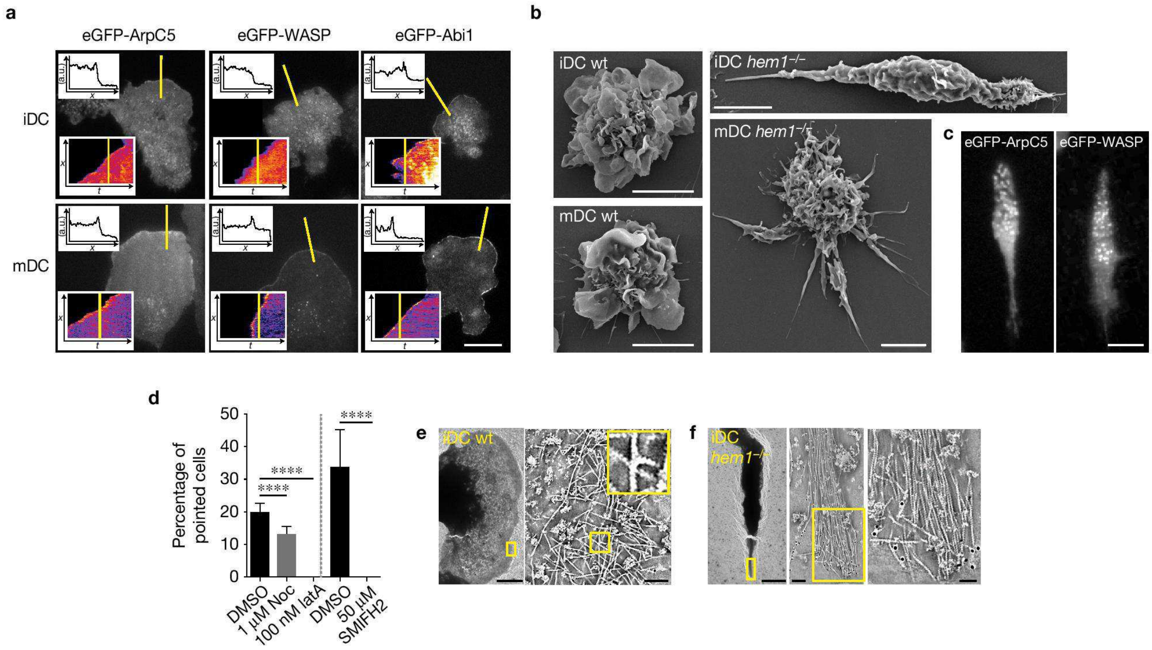

Figure 1 Localization of Arp2/3 activation machinery and morphologies of wild-type (wt) and *hem1*$^{-/-}$ DCs. (**a**) Snapshots using TIRF microscopy of i- and mDCs expressing reporter constructs for ArpC5, WASP and Abi1. The insets show kymographs and histograms of fluorescence intensity along the yellow lines in the main figures. *t*, time; *x*, position. Scale bar, 10 μm. (**b**) Scanning electron microscopy (SEM) pictures of wt and *hem1*$^{-/-}$ i- and mDCs. All scale bars, 5 μm. (**c**) Snapshots using TIRF microscopy of *hem1*$^{-/-}$ iDCs expressing reporter constructs for ArpC5 and WASP. Scale bar, 10 μm. (**d**) Quantification of *hem1*$^{-/-}$ iDC cell shape in suspension following pharmacological treatment; the dotted line denotes separate experiments. Noc, nocodazole; latA, latrunculin A. Mean ± s.d., left: one-way ANOVA, right: two-tailed *t*-test, $^{****}P < 0.0001$. $n = 8$ analysed dishes per treatment pooled from two (left) or three (right) biologically independent experiments. (**e**) Left: electron tomography of wt iDC. Scale bar, 5 μm. Right: section of the lamellipodium marked by the yellow square in the left picture. Scale bar, 100 nm. Inset: detail of the branch junction marked by the yellow square. (**f**) Left: electron tomography of *hem1*$^{-/-}$ iDC. Scale bar, 5 μm. Middle: section of the tip marked by the yellow square in the left picture. Scale bar, 100 nm. Right: detail of parallel actin filaments marked by the yellow square in the middle picture. Scale bar, 20 nm.

localizations in i- and mDCs expressing fluorescent reporters. We focused on WASP and the WAVE complex as the prime candidates to drive Arp2/3 activation at the plasma membrane[9]. Total internal reflection (TIRF) microscopy of i- and mDCs migrating in confined environments revealed dot-like actin, Arp2/3, WASP and WAVE patterns in the mid zone of the cell body (Fig. 1a). At the cell front WASP was absent in iDCs but weakly detectable in mDCs (Fig. 1a). In protruding lamellipodia of i- and mDCs, the presence of Arp2/3 was accompanied by the localization of WAVE components in a fine line at the lamellipodial tip. Here WAVE components were enhanced during protrusion and vanished during phases of stagnation or retraction (Fig. 1a and Supplementary Videos 1 and 2). On the basis of these localization data and the absence of significant shape alterations in WASP-deficient DCs, we genetically targeted the WAVE complex as the likely driver of lamellipodia formation. To this end, we used conditional gene targeting in mice to delete *hem1* (Supplementary Fig. 1), a subunit of the complex that is specific for the haematopoietic system[10,11]. *hem1*$^{-/-}$ DCs showed regular differentiation and none of the three WAVE isoforms was detectable (Supplementary Fig. 2A,B), indicating degradation of the pentameric complex in the absence of *hem1*[12,13]. Strikingly, *hem1*$^{-/-}$ iDCs lacked the usual lamellipodia and displayed an almost linear needle-like shape, with one sharply pointed front and a rounded rear (Fig. 1b and Supplementary Fig. 2C and Supplementary Video 3). Similarly, deletion of WAVE2 (another member of the WAVE complex) by CRISPR-mediated genome editing in transiently immortalized haematopoietic precursor cells phenocopied the needle-like shape, excluding WAVE-independent functions as the origin of the phenotype (Supplementary Fig. 2D). In *hem1*-deficient cells, no Arp2/3 accumulated at the leading edge, while Arp2/3- and WASP-positive dots were still detectable throughout the cell body (Fig. 1c and Supplementary Fig. 2E). Cortical actin appeared unchanged and myosin light chain located to the cell rear as it did in control cells (Supplementary Fig. 2F). Consistent with the loss of lamellipodia, total F-actin levels, as measured by flow cytometric analysis of incorporated phalloidin, were decreased by ~35%. There was no detectable difference in G-actin content (Supplementary Fig. 2G,H).

This indicated that cytoskeletal alterations in the mutant cells were restricted to the leading front. While pharmacological disruption of microtubules only mildly altered the shape of *hem1*$^{-/-}$ cells, interference with F-actin by latrunculin A as well as treatment with the pan-formin inhibitor SMIFH2[14] led to immediate and complete cell rounding (Fig. 1d). This suggested that the pointed extension is driven by formin-mediated actin nucleation. To follow up this notion, we performed electron tomography to trace actin filaments *in situ*. Wild-type cells showed canonical branch points with a 70° configuration

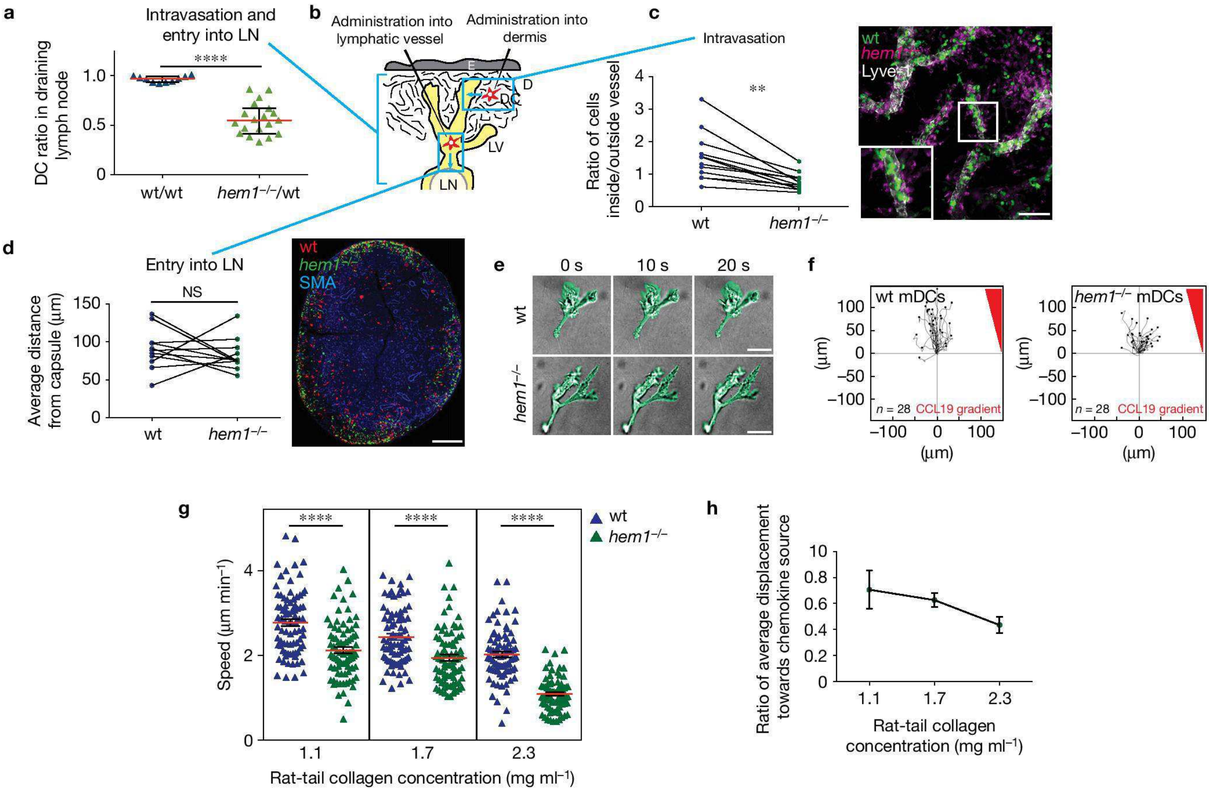

Figure 2 Migratory properties of wt and *hem1*$^{-/-}$ mDCs *in vivo* and *in vitro*. (**a**) Ratio of differentially labelled wt/wt and *hem1*$^{-/-}$/wt mDCs in LNs of wt recipient mice, 24 h after footpad injection. LN, lymph node. Mean (red line) ± s.d. (black bars). Two-tailed *t*-test, $^{****}P < 0.0001$. $n = 10$ LNs (wt/wt), $n = 19$ LNs (*hem1*$^{-/-}$/wt), obtained from one (wt/wt) or pooled from two (*hem1*$^{-/-}$/wt) biologically independent experiments. (**b**) Schematic of the experiments shown in **a**,**c** and **d**. D, dermis; E, epidermis; LV, lymph vessel. (**c**) Left: ratios of wt and *hem1*$^{-/-}$ mDCs inside/outside LVs 2 h after application to ears. Blue and green dots connected with a line represent data from one ear. Two-tailed *t*-test, $^{**}P = 0.0034$. $n = 12$ ears pooled from two biologically independent experiments. Right: *Z* projection of intravasation assay 2 h after application of wt (green) and *hem1*$^{-/-}$ (magenta) mDCs. LVs are stained with Lyve-1 (white). Inset: detail of the region marked by the white square. Scale bar, 100 μm. (**d**) Left: average distance (μm) of differentially labelled wt and *hem1*$^{-/-}$ mDCs from the LN capsule 4.5 h after intralymphatic injection. Blue and green dots connected with a line represent data from one LN. Two-tailed *t*-test (log transformed), not significant (NS) $P = 0.6$. $n = 11$ LNs from one experiment. Right: example of LN 4.5 h after intralymphatic co-injection of wt (red) and *hem1*$^{-/-}$ (green) mDCs. LN is stained for smooth muscle actin (SMA, blue). Scale bar, 300 μm. (**e**) Time-lapse sequence of migrating wt and *hem1*$^{-/-}$ mDCs in response to CCL19 in 3D collagen gels. Cells are pseudo-coloured in green. Scale bars, 20 μm. (**f**) Tracks of wt and *hem1*$^{-/-}$ mDCs in response to CCL19 gradient in 3D collagen gels. (**g**) Single-cell speeds (μm min^{-1}) of wt and *hem1*$^{-/-}$ mDCs in response to CCL19 gradient, depending on increasing rat-tail collagen concentrations. Mean (red line) ± s.e.m. (black bars). Two-tailed *t*-tests (square root transformed for 1.7 mg ml^{-1}), $^{****}P < 0.0001$. $n = 82/80/81$ cells (wt: 1.1/1.7/2.3 mg ml^{-1}), $n = 80/81/80$ cells (*hem1*$^{-/-}$: 1.1/1.7/2.3 mg ml^{-1}) pooled from three biologically independent experiments. (**h**) Ratio of average displacement per frame of *hem1*$^{-/-}$/wt mDCs towards the CCL19 source, depending on increasing rat-tail collagen concentrations. Mean (green dots) ± s.e.m. (black bars). Data stem from the same three biological replicates as in **g**.

distributed across the lamellipodium[15,16] (Fig. 1e and Supplementary Fig. 2I and Supplementary Video 4). In contrast, the pointed tips of *hem1*$^{-/-}$ iDCs contained entirely linear arrays of parallel filaments (Fig. 1f and Supplementary Fig. 2I) with barbed ends oriented towards the pointed cell edge (Supplementary Video 5)[17]. These findings demonstrate that in the absence of Arp2/3 activation, actin branches at the leading edge are lost and filaments arrange into linear arrays, causing the pointed protrusion morphology.

Notably, on maturation, *hem1*$^{-/-}$ DCs lost their linear shape and the cell bodies rounded up. However, instead of the usual broad and veiled lamellipodial protrusions found in control cells, they formed multiple dynamic, thin filopodial extensions and showed a ∼50% reduction in F-actin levels (Fig. 1b and Supplementary Fig. 2C,G and H and Supplementary Video 3). With immature and mature WAVE-complex-deficient DCs, we had two morphologically different cell variants at hand, where lamellipodia were either replaced by one or multiple filopodia. In the following, we utilized these mutants and their respective control counterparts as a tool to dissect the role of lamellipodia and filopodia in guided locomotion within physiological environments.

MDCs use the chemokine receptor CCR7, to sense the two chemokines, CCL19 and CCL21, which guide the cells from the periphery into the draining lymph node[7]. To explore lamellipodial versus filopodial migration *in vivo*, we co-injected *hem1*$^{-/-}$ and

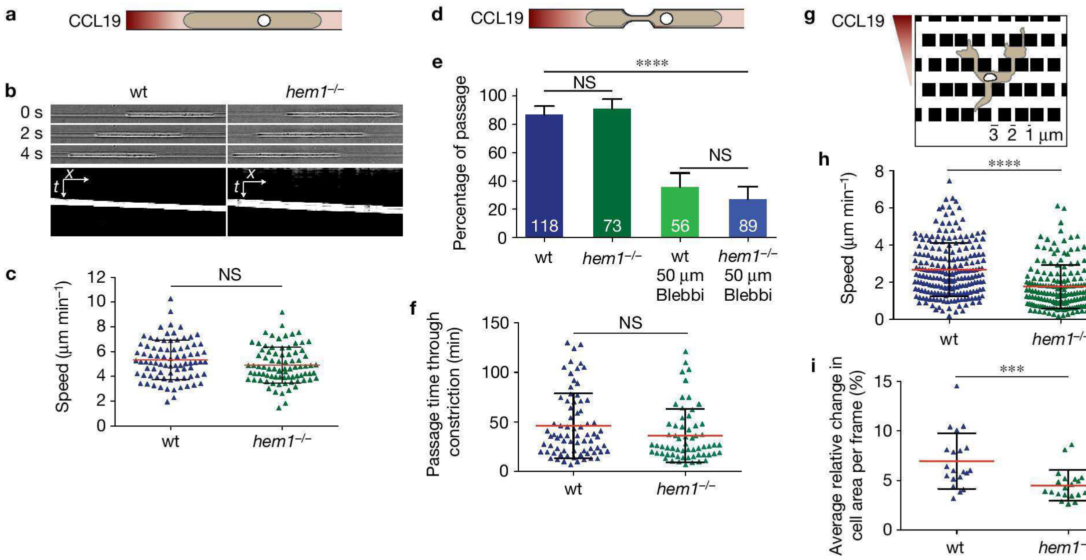

Figure 3 Migratory properties of wt and *hem1*$^{-/-}$ mDCs in microfluidic devices. (**a**) Scheme of the experimental set-up for **b** and **c**. (**b**) Time-lapse sequence and exemplary kymographs of wt and *hem1*$^{-/-}$ mDCs migrating towards the CCL19 source in straight microchannels. (**c**) Single-cell speeds (µm min^{-1}) of wt and *hem1*$^{-/-}$ mDCs in response to CCL19 gradient, migrating in straight microchannels. Mean (red line) ± s.d. (black bars). Two-tailed *t*-test, not significant (NS) $P=0.0773$. $n=82$ cells (wt), $n=83$ cells (*hem1*$^{-/-}$) pooled from two biologically independent experiments. (**d**) Scheme of the experimental set-up for **d** and **f**. (**e**) Percentage of wt and *hem1*$^{-/-}$ mDCs passing the constriction when migrating towards CCL19 gradient in the absence (dark colours) or presence (light colours) of 50 µM blebbistatin (Blebbi). s.d. (black bars). Fisher's exact test, wt ($n=118$ cells) versus *hem1*$^{-/-}$ ($n=73$ cells): NS $P=1$; wt 50 µM Blebbi ($n=56$ cells) versus *hem1*$^{-/-}$ 50 µM Blebbi ($n=89$ cells): NS $P=0.1439$; untreated versus 50 µM Blebbi: $^{****}P<0.0001$. Three biological replicates. (**f**) Single-cell passage times through the constriction of wt and *hem1*$^{-/-}$ mDCs migrating towards CCL19 gradient. Mean (red line) ± s.d. (black bars). Two-tailed *t*-test (log transformed), NS $P=0.0586$. $n=74$ cells (wt), $n=62$ cells (*hem1*$^{-/-}$) pooled from three biological replicates. (**g**) Scheme of 'maze' set-up for **h** and **i**. (**h**) Speeds (µm min^{-1}) of single cell tracks from wt and *hem1*$^{-/-}$ mDCs in response to CCL19 gradient, migrating in a microfluidic 'maze' device. Mean (red line) ± s.d. (black bars). Mann–Whitney test, $^{****}P<0.0001$. $n=214$ tracks (wt), $n=180$ tracks (*hem1*$^{-/-}$) pooled from three biologically independent experiments. (**i**) Mean change in cell area per frame in percentage, relative to the previous frame of single wt and *hem1*$^{-/-}$ mDCs migrating in a microfluidic 'maze' device. Mean (red line) ± s.d. (black bars). Mann–Whitney test, $^{***}P=0.0004$. $n=20$ cells (wt), $n=21$ cells (*hem1*$^{-/-}$). Data stem from the same three biological replicates as in **h**.

control mDCs into mouse footpads and found that *hem1*$^{-/-}$ cells had a competitive disadvantage to reach the draining lymph node (Fig. 2a,b). To determine at which level the cells were impaired we measured migration in mouse ear explants, where chemokine-guided interstitial migration versus entry into the lymphatic vessels can be distinguished. *hem1*$^{-/-}$ cells preferentially accumulated at the lymphatic vessel wall, while control cells located in the vessel lumen (Fig. 2b,c). The perivascular accumulation was pronounced even after extended times of intravasation, indicating that beyond a possible defect in interstitial crawling, the vessel wall represents a rate-limiting barrier for the mutant cells (Supplementary Fig. 3A,B). When we bypassed the peripheral tissue and the vessel wall by directly injecting the cells into afferent lymphatic vessels[18], they equally entered the deep T-cell areas (Fig. 2b and d). This shows that the passage through the loose and primarily cellular environment of the lymph node was intact, whereas *hem1*$^{-/-}$ mDCs had a possible defect in interstitial crawling and a pronounced defect in intravasation. Intravasation begins with the passage through the endothelial basement membrane, which constitutes a perforated sheet, where cells transiently halt and probe the surface to select an appropriate pore for entry[19]. We hypothesized that lamellipodia might act as effective 'analogue' exploratory sensors to sample the geometry of the tissue, whereas filopodia have a limited sampling range due to their 'digital' configuration. To test sampling in complex environments, we measured chemotaxis through collagen gels of increasing density and, thus, decreasing pore size[20]. In accordance with their shape in suspension, *hem1*$^{-/-}$ mDCs migrated with multiple pointed instead of lamellipodial protrusions (Fig. 2e and Supplementary Videos 6 and 7). At low collagen concentrations, both control and mutant cells showed efficient chemotaxis (Fig. 2f and Supplementary Fig. 3C). However, *hem1*$^{-/-}$ mDCs migrated with significantly reduced speed (Fig. 2g). Notably, the disadvantage in speed of *hem1*$^{-/-}$ versus control mDCs increased with the density of the gels and *hem1*$^{-/-}$ mDCs were virtually immobilized at high densities where their wild-type counterparts still effectively migrated (Fig. 2g,h).

These data are compatible with the idea that lamellipodia are required to make optimal decisions when cells have to thread their cell body and nucleus through geometrically complex environments. However, Arp2/3 might also be involved in the cell body/nuclear passage as such[21]. To dissect these possibilities, we devised a series of more reductionist assay systems. We first mimicked barrier and decision-free 1D chemokine-driven migration by placing the cells into linear microfluidic channels with a geometry that completely confined the cells (Fig. 3a)[22]. Under these conditions, both control and *hem1*$^{-/-}$ mDCs migrated efficiently and with no detectable difference in speed (Fig. 3b,c). We next introduced constrictions into the channels, which

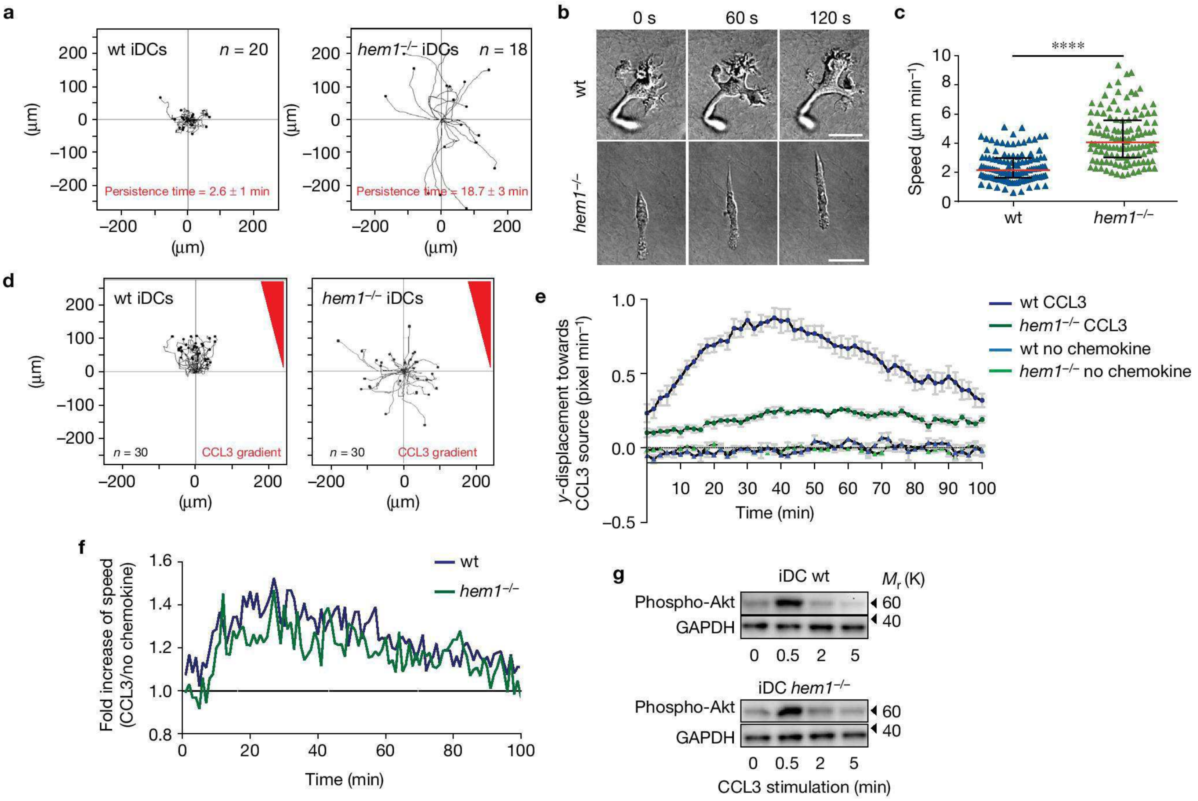

Figure 4 Migratory properties of wt and *hem1*$^{-/-}$ iDCs. (**a**) Single-cell tracks of wt and *hem1*$^{-/-}$ iDCs migrating in 3D collagen gels. (**b**) Time-lapse sequence of migrating wt and *hem1*$^{-/-}$ iDCs migrating in 3D collagen gels. Scale bars, 20 µm. (**c**) Single-cell speeds (µm min^{-1}) of wt and *hem1*$^{-/-}$ iDCs migrating in 3D collagen gel. Mean (red line) ± s.d. (black bars). Two-tailed *t*-test (square root transformed), $^{****}P < 0.0001$. $n = 120$ cells (wt), $n = 120$ cells (*hem1*$^{-/-}$) pooled from three biologically independent experiments. (**d**) Single-cell tracks of wt and *hem1*$^{-/-}$ iDCs in response to CCL3 gradient in 3D collagen gels. (**e**) Average *y*-displacement (pixel min^{-1}) over time (min) of wt (blue) and *hem1*$^{-/-}$ (green) iDCs in the absence of (triangles), or in response to (circles) CCL3 gradient. Mean (dots and triangles) ± s.e.m. (black bars). $n = 6$ collagen gels (wt and *hem1*$^{-/-}$ CCL3) or $n = 3$ collagen gels (wt and *hem1*$^{-/-}$ no chemokine) pooled from three biologically independent experiments. (**f**) Average fold increase in speed over time (min) of wt and *hem1*$^{-/-}$ iDCs in response to CCL3 gradient compared with no chemokine. Mean (green and blue lines). Data stem from the same three biological replicates as in **e**. (**g**) Western blots of wt and *hem1*$^{-/-}$ iDCs stimulated with CCL3 chemokine consecutively stained for phosphorylated Akt and GAPDH.

are at the limiting size to allow nuclear passage (Fig. 3d)[21]. Rates of passage or passage times were not reduced in *hem1*$^{-/-}$ mDCs (Fig. 3e,f). After excluding defects in basic locomotion or nuclear passage in *hem1*$^{-/-}$ mDCs, we sought to test their ability to make directional choices. To this end, we established microfluidic devices that confined the cells in the *z* dimension while the *xy*-field was built of roadblocks positioned with variable spacing. This essentially creates a maze that cells have to negotiate to follow chemokine gradients (Fig. 3g). Control, as well as *hem1*$^{-/-}$, cells efficiently navigated along the gradients, but now *hem1*$^{-/-}$ mDCs were considerably slower than control cells (Fig. 3h and Supplementary Video 8). To measure protrusion dynamics, we determined the average change of cell area per frame. This was significantly reduced for *hem1*$^{-/-}$ cells compared with their wild-type counterparts while overall cell size was unaffected (Fig. 3i and Supplementary Fig. 3D). This suggests that, when confronted with multiple directional choices, their reduced protrusion dynamics gives *hem1*$^{-/-}$ mDCs a competitive disadvantage over control cells in efficiently negotiating complex environments.

We next compared the migration of unipolar *hem1*$^{-/-}$ iDCs with control iDCs. When placed in low-density 3D collagen scaffolds, control cells showed vivid protrusion dynamics, but net displacements were minimal due to frequent directional changes (Fig. 4a,b and Supplementary Video 9). Strikingly, *hem1*$^{-/-}$ cells migrated with substantially increased speed (Fig. 4c) and showed massively increased directional persistence (Fig. 4a and Supplementary Fig. 4A). During migratory phases the cells maintained their linear shape (Fig. 4b and Supplementary Video 10) and the rare directional changes were associated either with transient arrest and rounding or with occasional bifurcation of the leading edge (Supplementary Video 10). Bifurcations consistently caused deceleration (Supplementary Fig. 4B and Supplementary Video 10). Importantly, also control cells showed phases of straight and fast migration and these were associated with elongated morphology. This was shown quantitatively by a correlation between shape index and migratory speed (Supplementary Fig. 4C). These observations support the idea that diversification of the leading edge effectively slows locomotion[23,24]. This might potentially explain

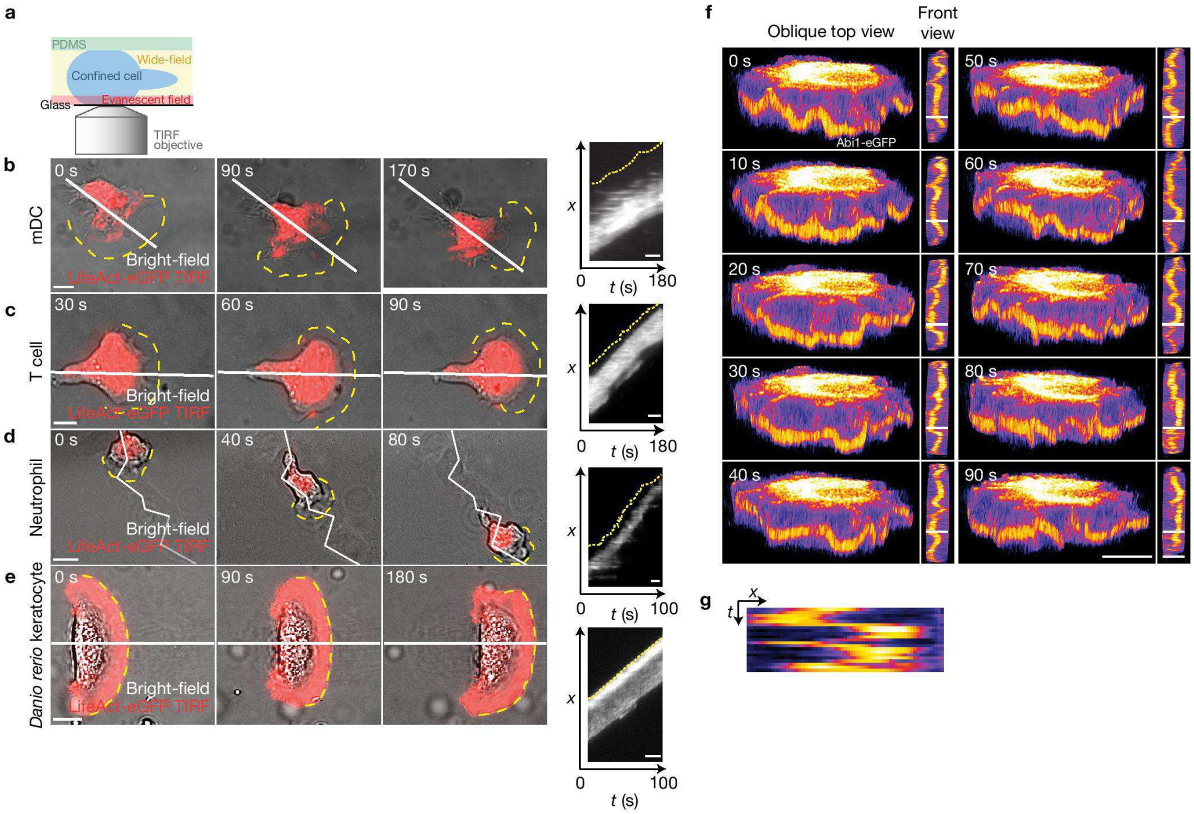

Figure 5 Lamellipodial position of leukocytes during confined migration. (**a**) A schematic depicting the experiments in **b**–**d**. PDMS, polydimethylsiloxane. (**b**–**e**) Bright-field and TIRF (red) time-lapse sequence of a wt mDC (**b**), T cell (**c**), neutrophil (**d**) (migrating under confinement) and fish keratocyte (**e**). The yellow dashed lines outline the rim of the lamellipodium. The white lines mark kymographs plotted on the right. All scale bars, 5 μm. (**f**) Oblique top- and front-view false-colour time-lapse *z*-reconstructions of a wt mDC expressing Abi1-eGFP. Scale bar oblique top view, 10 μm. Scale bar front views, 3 μm. The white lines in the front views mark the kymograph plotted in **g**. (**g**) Kymograph showing the dynamics of the region over time.

the gain in migration speed of unipolar *hem1*$^{-/-}$ iDCs compared with their control counterparts.

To test the chemotactic response of WAVE-complex-deficient iDCs, we incorporated them into 3D collagen gels and exposed them to gradients of CCL3. In contrast to wild-type controls, *hem1*$^{-/-}$ as well as *wave2*-/- iDCs showed only minimal responses to chemotactic gradients (Fig. 4d,e and Supplementary Fig. 4D,E). Notably, the chemokinetic response of both mutants and controls followed the same dynamics, suggesting that chemokine sensing, signalling or signal adaptation was unimpaired (Fig. 4f). In line with these data, signalling following chemokine exposure was unimpaired (Fig. 4g and Supplementary Fig. 4F) when measured biochemically at the level of phosphorylation of downstream targets.

These data suggest that lamellipodia and filopodia primarily serve as directional selectors in these cells[25,26], while the main forces driving actual locomotion might be generated elsewhere. To directly probe the role of lamellipodia in force transduction, we devised a microfluidic set-up where leukocytes migrate confined between two parallel surfaces[27] (Fig. 5a). This reductionist setting allowed cells to efficiently migrate under minimal adhesive conditions in an actin-dependent manner[5]. When migrating DCs expressing an actin reporter were simultaneously imaged with wide-field and TIRF microscopy, it turned out that lamellipodial actin rarely contacted the substrate, while the cell body formed a continuous interface, where retrograde actin flow was minimal compared with the lamellipodial region (Fig. 5b and Supplementary Video 11). We obtained comparable data with migrating lymphoblasts and neutrophil granulocytes (Fig. 5c,d and Supplementary Video 11) but not with adhesively migrating fish keratocytes, which form large lamellipodia in continuous contact with the substrate (5e and Supplementary Video 11). Fast confocal observation of migrating mDCs expressing Abi1-GFP, which decorates the lamellipodial tip, confirmed that lamellipodia are in contact with neither bottom nor top surfaces, thereby largely undulating in the free space between the confining surfaces (Fig. 5f,g and Supplementary Video 12).

Together, we show that in fast-migrating leukocytes, actin-driven protrusions in the form of lamellipodia and filopodia facilitate directional choices and invasion of complex matrices, while actual translocation is driven by the cell body[28] (Supplementary Fig. 5). This mechanism differs from mesenchymal migration[29], where adhesions are born in the lamellipodium and thereby determine cell shape and mediate translocation. Migration with a freely exploring lamellipodium is more in line with bleb-driven locomotion where the (actin free) cell front is unlikely to participate in force transduction and friction with the substrate mainly emerges in the central regions of the cell[30,31]. We therefore suggest that the leukocyte's lamellipodium is rather a sensory organelle than a force-transducing unit. ☐

METHODS

Methods, including statements of data availability and any associated accession codes and references, are available in the online version of this paper.

Note: Supplementary Information is available in the online version of the paper

ACKNOWLEDGEMENTS
This work was supported by the German Research Foundation (DFG) Priority Program SP 1464 to T.E.B.S. and M.S., and European Research Council (ERC GA 281556) and Human Frontiers Program grants to M.S. We thank H. Haecker for his generous help with HoxB8 immortalization, J. Renkawitz for critical reading of the manuscript and the Scientific Service Units of IST Austria for excellent technical support.

AUTHOR CONTRIBUTIONS

A.L. and A.E. devised and performed most experiments. A.R., J.S., I.d.V. and J.Merrin helped with microfluidic approaches. J.Müller, F.S., J.B. and J.V.S. performed electron tomography. M.B. and D.K. performed intralymphatic injections. S.W. and R.H. helped with quantitative analysis. D.J.J.d.G., F.P.L.L., M.M., K.R. and T.E.B.S. generated *hem1*-deficient mice. M.S. initiated and supervised the project and wrote the paper with input from all authors.

COMPETING FINANCIAL INTERESTS

The authors declare no competing financial interests.

1. Skau, C. T. & Waterman, C. M. Specification of architecture and function of actin structures by actin nucleation factors. *Annu. Rev. Biophys.* **44**, 285–310 (2015).
2. Rotty, J. D., Wu, C. & Bear, J. E. New insights into the regulation and cellular functions of the ARP2/3 complex. *Nat. Rev. Mol. Cell Biol.* **14**, 7–12 (2012).
3. Wu, C. *et al.* Arp2/3 is critical for lamellipodia and response to extracellular matrix cues but is dispensable for chemotaxis. *Cell* **148**, 973–987 (2012).
4. Suraneni, P. *et al.* The Arp2/3 complex is required for lamellipodia extension and directional fibroblast cell migration. *J. Cell Biol.* **197**, 239–251 (2012).
5. Renkawitz, J. *et al.* Adaptive force transmission in amoeboid cell migration. *Nat. Cell Biol.* **11**, 1438–1443 (2009).
6. Lämmermann, T. *et al.* Rapid leukocyte migration by integrin-independent flowing and squeezing. *Nature* **453**, 51–55 (2008).
7. Heuzé, M. L. *et al.* Migration of dendritic cells: physical principles, molecular mechanisms, and functional implications. *Immunol. Rev.* **256**, 240–254 (2013).
8. Redecke, V. *et al.* Hematopoietic progenitor cell lines with myeloid and lymphoid potential. *Nat. Methods* **10**, 795–803 (2013).
9. Campellone, K. G. & Welch, M. D. A nucleator arms race: cellular control of actin assembly. *Nat. Rev. Mol. Cell Biol.* **11**, 237–251 (2010).
10. Hromas, R., Collins, S., Raskind, W., Deaven, L. & Kaushansky, K. Hem-1, a potential membrane protein, with expression restricted to blood cells. *Biochim. Biophys. Acta* **1090**, 241–244 (1991).
11. Weiner, O. D. *et al.* Hem-1 complexes are essential for rac activation, actin polymerization, and myosin regulation during neutrophil chemotaxis. *PLoS Biol.* **4**, e38 (2006).
12. Blagg, S. L., Stewart, M., Sambles, C. & Insall, R. H. PIR121 regulates pseudopod dynamics and SCAR activity in dictyostelium. *Curr. Biol.* **13**, 1480–1487 (2003).
13. Kunda, P., Craig, G., Dominguez, V. & Baum, B. Abi, Sra1, and kette control the stability and localization of SCAR/WAVE to regulate the formation of actin-based protrusions. *Curr. Biol.* **13**, 1867–1875 (2003).
14. Rizvi, S. A. *et al.* Identification and characterization of a small molecule inhibitor of formin-mediated actin assembly. *Chem. Biol.* **16**, 1158–1168 (2009).
15. Svitkina, T. M. & Borisy, G. G. Arp2/3 complex and actin depolymerizing factor/cofilin in dendritic organization and treadmilling of actin filament array in lamellipodia. *J. Cell Biol.* **145**, 1009–1026 (1999).
16. Vinzenz, M. *et al.* Actin branching in the initiation and maintenance of lamellipodia. *J. Cell Sci.* **125**, 2775–2785 (2012).
17. Narita, A. *et al.* Direct determination of actin polarity in the cell. *J. Mol. Biol.* **419**, 359–368 (2012).
18. Braun, A. *et al.* Afferent lymph-derived T cells and DCs use different chemokine receptor CCR7-dependent routes for entry into the lymph node and intranodal migration. *Nat. Immunol.* **12**, 879–887 (2011).
19. Pflicke, H. & Sixt, M. Preformed portals facilitate dendritic cell entry into afferent lymphatic vessels. *J. Exp. Med.* **206**, 2925–2935 (2009).
20. Wolf, K. *et al.* Physical limits of cell migration: control by ECM space and nuclear deformation and tuning by proteolysis and traction force. *J. Cell Biol.* **201**, 1069–1084 (2013).
21. Thiam, H.-R. *et al.* Perinuclear Arp2/3-driven actin polymerization enables nuclear deformation to facilitate cell migration through complex environments. *Nat. Commun.* **7**, 1–14 (2016).
22. Heuzé, M. L., Collin, O., Terriac, E., Lennon-Dumenil, A.-M. & Piel, M. *Methods in Molecular Biology* Vol. 769, 415–434 (Humana Press, 2011).
23. Pankov, R. A Rac switch regulates random versus directionally persistent cell migration. *J. Cell Biol.* **170**, 793–802 (2005).
24. Dang, I. *et al.* Inhibitory signalling to the Arp2/3 complex steers cell migration. *Nature* **508**, 281–284 (2013).
25. Insall, R. H. Understanding eukaryotic chemotaxis: a pseudopod-centred view. 1–6 (2010).
26. Arrieumerlou, C. & Meyer, T. A local coupling model and compass parameter for eukaryotic chemotaxis. *Dev. Cell* **8**, 215–227 (2005).
27. Le Berre, M., Zlotek-Zlotkiewicz, E., Bonazzi, D., Lautenschlaeger, F. & Piel, M. *Methods for Two-Dimensional Cell Confinement. Methods in Cell Biology* Vol. 121, 213–229 (Elsevier, 2014).
28. Stanley, P. *et al.* Intermediate-affinity LFA-1 binds α-actinin-1 to control migration at the leading edge of the T cell. *EMBO J.* **27**, 62–75 (2007).
29. Case, L. B. & Waterman, C. M. Integration of actin dynamics and cell adhesion by a three-dimensional, mechanosensitive molecular clutch. *Nat. Cell Biol.* **17**, 955–963 (2015).
30. Kardash, E. *et al.* A role for Rho GTPases and cell–cell adhesion in single-cell motility *in vivo*. *Nat. Cell Biol.* **12**, 47–53 (2009).
31. Bergert, M. *et al.* Force transmission during adhesion-independent migration. *Nat. Cell Biol.* **17**, 524–529 (2015).

METHODS

Cell culture and transgene delivery. R10 medium, consisting of RPMI 1640, supplemented with 10% fetal calf serum (FCS), 2 mM L-glutamine, 100 U ml^{-1} penicillin, 100 µg ml^{-1} streptomycin and 50 µM 2-mercaptoethanol (all Invitrogen), was used as basic medium for all cells unless stated otherwise. All cells were grown and maintained at 37 °C/5% CO$_2$ unless noted otherwise.

No cell lines used in this study were found in the database of commonly misidentified cell lines that is maintained by ICLAC and NCBI biosample. The cell lines were not authenticated. Cell lines tested negative for mycoplasma.

Plasmids and lentivirus production. The following fusion constructs were as described: Lifeact-eGFP[32], eGFP-ArpC5B and eGFP-Abi1[33], eGFP-WASP and eGFP-WAVE2[34], eGFP-WAVE1 and eGFP-WAVE3[35]. MLC-eGFP was a gift from M. Olson (Beatson Institute, UK).

Fusion-protein-coding lentiviruses were produced in LX-293 HEK cells (Clontech) by co-transfection of the expression plasmids (pLenti6.3, Invitrogen) with pCMV-dR8.91 packaging- and pCMV-VSV-G envelope plasmids (a gift from B. Weinberg, MIT, USA, Addgene plasmid no. 8454). To create the lentiviral CRISPR WAVE2 knockout construct, a gRNA (5′-GCAAATGTCATCCGACAGCT-3′) directed against the first exon of the *wasf2* gene was cloned into the LentiCRISPRv1 vector (a gift from F. Zhang (Broad Institute of MIT and Harvard, USA), Addgene plasmid no. 49535).

Animals. All animal experiments are in accordance with the Austrian law for animal experiments. Permission was granted by the Austrian federal ministry of science, research and economy (identification code: BMWF-66.018/0005-II/3b/2012). Mice were bred and maintained at the local animal facility in accordance with the IST Austria ethics commission.

Dendritic cells. Dendritic cells (DCs) were differentiated from bone marrow or transiently immortalized haematopoietic precursors[8], both originating from 6–12-week-old, male or female C57BL/6J wt or *hem1*$^{-/-}$ mice (for description of generation, see Supplementary Fig. 1).

Cells were differentiated in 9 ml R10, supplied with 1 ml in-house-generated granulocyte–macrophage colony stimulating factor (GM-CSF) hybridoma supernatant. On day 3, 8 ml R10, supplied with 2 ml GM-CSF, was added. Half of the medium was replaced on day 6. iDCs were used from day 7 on. For maturation, lipopolysaccharide (LPS) from *Escherichia coli* 0127:B8 (Sigma) was added to an end concentration of 200 ng ml^{-1} overnight.

For transgene delivery, bone marrow-derived DCs were transfected with 4–5 µg DNA, using the Mouse T cell Nucleofector Kit (Lonza). Transfected DCs were used one day after transfection and enriched by FACS for GFP-expressing cells.

Immortalized haematopoietic precursors were spin-infected (1,500*g*, 1 h) with lentiviruses in the presence of 8 µg ml^{-1} Polybrene. Cells were selected with either 10 µg ml^{-1} blasticidin (pLenti6.3) or 4 µg ml^{-1} puromycin (LentiCRISPRv1).

T cells. LMR7.5 Lack T cell hybridoma cells were a gift from A. M. Lennon (U932, Institut Curie, Paris, France) and used with the courtesy of N. Glaichenhaus (IPMC UMR7525, UNS, Sophia-Antipolis, France). The Mouse T cell Nucleofector Kit (Lonza) was used for Lifeact-GFP delivery. Before analysis, cells were cultured for 14 days in R10 supplied with 700 µg ml^{-1} geneticin (G418, Invitrogen).

Neutrophils. Neutrophils were enriched from bone marrow of 6–12-week-old, male or female C57BL/6J mice, heterozygous transgenic for Lifeact-eGFP, using the Easy step mouse neutrophil enrichment kit (Stemcell).

Keratocytes. Scales of adult Tg(actb:lifeact-GFP)[36] fish were transferred to cell culture dishes containing start medium as described previously[37]. After 1 day incubation at 28 °C, monolayers of cells were treated with 1 mM EDTA in running buffer[37] for 45–60 min to release individual cells.

Imaging and geometric confinement of cells. *Confinement.* For imaging of eGFP-ArpC5, eGFP-WASP and eGFP-Abi1, i- and mDCs were injected between PEG-coated glass and an agarose/medium layer as described previously[5]. CCL3 (iDCs) or CCL19 (mDCs) (both Peprotech) was used as chemo attractant.

For eGFP-Abi1 mDCs shown in Fig. 5f,g and all other cells, PDMS micropillars with defined heights were used for confinement. Briefly, the PDMS mixture (elastomer/curing agent ratio 7:1, Sylgard 184 Silicone Elastomer Kit, Dow Corning) was deposited onto a 3- or 4-µm-height micropillar mould produced by photolithography (for initial experiments provided by M. Le Berre, U144, Institut Curie, then produced at IST Austria by J. Merrin). Plasma-cleaned, round 12 mm glass coverslips (Menzel-Gläser, VWR) were placed onto the mould and cured at 95 °C for 15 min. Subsequently, micropillar-bearing coverslips were detached from the mould. For soft PDMS pistons, the PDMS mixture (elastomer/curing agent ratio 30:1, Sylgard 184 Silicone Elastomer Kit, Dow Corning) was cast into a home-made metal mould. Soft pistons were glued to the lid of the dish to apply pressure on the coverslip.

Before imaging, PDMS micropillars were coated with PLL-PEG and placed on the soft piston on the lid. In the case of T cells, coverslips were coated with 25 µg ml^{-1} fibronectin for 1 h. Cells were pipetted onto the coverslip and confined by applying the lid with the attached micropillar. The lid and coverslip were sealed with strong tape.

Dishes with failed confinement, assessed by cell morphology, were excluded from analysis.

Imaging. Confocal microscopy was performed on a motorized and heated stage at 37 °C/5% CO$_2$ with an inverted microscope (Zeiss), equipped with a spinning-disc system (iXon897, Andor), a Plan-Apochromat 100×/1.4 oil objective (Zeiss) and a 488 laser.

Total internal reflection (TIRF) microscopy was performed at 37 °C/5% CO$_2$ or at room temperature in the case of fish keratocytes, using an inverted Axiovert 200 (Zeiss) microscope, a TIRF 488/561-nm laser system (Visitron Systems) and an Evolve EMCCD camera (Photometrics) triggered by VisiView software (Visitron).

ImageJ was used for image- and kymograph analysis. Volocity (Perkin Elmer) was used for 3D reconstructions.

Preparation of scanning electron microscopy (SEM) samples. Wt or *hem1*$^{-/-}$ iDCs were seeded onto plasma-cleaned and poly-L-lysine (Sigma)-coated coverslips in R10 and incubated for 30 min at 37 °C/5% CO$_2$. For fixation, samples were washed with warm, serum-free, RPMI 1640 and fixed, using warm Trump's fixative (1% glutaraldehyde, 4% formaldehyde in 0.1 M phosphate buffer, pH 7.2) followed by 1% osmium tetroxide in water. After rinsing with water, samples were dehydrated in a graded series of acetone and critical point dried in a Balzers CPD 030. Samples were examined with a FEG-SEM Quanta 200 (FEI, Eindhoven, Netherlands) operated at 5 kV and equipped with an Everhart–Thornley detector. At least 10 cells were imaged for each genotype and maturation state. Cells that showed clear morphological defects due to the fixation were excluded from the analysis.

FACS antibody staining of surface markers. All stainings were carried out in FACS buffer (1× PBS, 2 mM EDTA, 1% BSA). Used antibodies are listed in Supplementary Table 1. Prior to staining with primary antibody, Fc receptors were blocked (using anti-mouse CD16/CD32) to prevent unspecific antibody binding. In the case of biotin-labelled primary antibodies, PE-labelled streptavidin was subsequently used for staining. All incubation steps were carried out for 15 min at 4 °C, except CCR7-PE, which was incubated for 30 min at 37 °C. All samples were kept on ice until data acquisition on a FACS Aria III (Beckton Dickinson). All stainings were carried out three times with cells from biologically independent samples.

Total F-actin stain. Wt and *hem1*$^{-/-}$ i- and mDCs (3×10^5) were seeded into a PLL-PEG-coated 12-well plate in 500 µl R10, recovered at 37 °C for 30 min and stained during fixation (4% PFA, 20 µM FITC-phalloidin and 0.5% saponin in PBS, 500 µl, 20 min at 37 °C). Samples were analysed on a FACS Aria III. Stainings were carried out three times with cells from biologically independent samples.

Immunodetection of actin, WAVE proteins and phospho-proteins. For western blotting, wt and *hem1*$^{-/-}$ i- and mDCs were spun down and re-suspended in RIPA buffer (NEB), supplemented with PhosSTOP (Roche) and complete protease inhibitor (Roche). For detection of Akt and phosphorylated Akt after chemokine stimulation, wt and *hem1*$^{-/-}$ iDCs were stimulated with CCL3 (PeproTech, final concentration: 0.625 µg ml^{-1}) for the indicated times.

Cell lysates were prepared according to NEB's protocol and subsequently used for immunodetection. In all cases, GAPDH was used as loading control. Used antibodies are listed in Supplementary Table 1.

Protein lysates were separated by SDS–PAGE on Novex 4–12% Tris-Glycine gradient gels (Invitrogen) and subsequently electrophoretically transferred to a PVDF membrane using the iBlot(R) Western Blotting System (Invitrogen). Membranes were blocked in 5% BSA/TBS-T for one hour before overnight incubation with primary antibodies at 4 °C. In the case of actin, membranes were blocked with 5% non-fat milk/TBS-T and incubated with primary antibody for 1 h at room temperature. After washing with TBS-T, membranes were incubated with secondary horseradish peroxidase (HRP)-coupled antibody for one hour. Enhanced chemiluminescent substrate for HRP (SuperSignal West Femto Chemiluminescent Substrate, Thermo Fisher) was applied to membranes prior to detection of the chemiluminescent signal with the Molecular Imager(R) VersaDoc MP Imaging System (Bio Rad).

Pharmacological disruption of the cytoskeleton. *hem1*$^{-/-}$ iDCs were plated in pre-warmed R10 medium, with end concentrations of 100 nM latrunculin A, 1 µM nocodazole or 50 µM SMIFH2. Cells were incubated at 37 °C/5% CO$_2$ for 30 min prior to imaging (Leica DM IL Led, inverted microscope with attached Leica DFC450 digital camera). For image analysis and quantification the total and number of pointed, needle shaped (defined by an aspect ratio >2) cells were counted and their percentage under the different treatments was determined. The experiment was carried out three times, using cells from biologically independent samples. No sample was excluded from analysis.

Electron tomography. Wt and *hem1*$^{-/-}$ iDCs were seeded onto poly-L-lysine (Sigma)-coated EM-grids (1% formvar-coated 200 mesh hexagonal Au grids with additional carbon, glow discharged, Agar Scientific) for 2 h. Afterwards, cells were simultaneously extracted and fixed with 0.5% Triton X-100 (Fluka) and 0.25% glutaraldehyde (Agar Scientific) in cytoskeleton buffer (10 mM MES, 150 mM NaCl, 5 mM EGTA, 5 mM glucose, and 5 mM $MgCl_2$, pH 6.1). After initial fixation of 1–2 min, post fixation was carried out for 15 min in cytoskeleton buffer containing 2% glutaraldehyde and 1 μg ml^{-1} phalloidin (Life Technologies). Samples were stored in 2% glutaraldehyde with 10 μg ml^{-1} phalloidin at 4 °C before processing for EM.

For electron tomography, gold grids were stained with 5–8% sodium silicotungstate including 1 μg ml^{-1} phalloidin and a 1:10 BSA–gold colloid preparation. Tilt series were acquired on an FEI Tecnai F30 Helium (Polara) microscope, operated at 300 kV and cooled to approximately 80 K. Automated acquisition of tilt series was driven by SerialEM 3.x. For every sample two tilt series around orthogonal axes were recorded on a Gatan UltraScan 4000 CCD camera at magnifications ranging from ×31,000 to ×39,000 with binning 2, giving a typical pixel size of 0.75–0.59 nm. Re-projections from the tilt series were generated using IMOD software from the Boulder Laboratory for 3D Electron Microscopy of Cells (http://bio3d.colorado.edu/imod), using the gold particles as fiducials for alignments. Using IMOD, filaments were manually tracked and models generated. A typical tomogram comprised a z-stack of 75–95 sections of 0.746 nm each (≈56–71 nm in total). The polarity of actin filaments in tomograms of negatively stained samples was determined using a filament straightening protocol and cross-correlation analysis as described previously[17]. The whole procedure was carried out for two cells per genotype. Cells that clearly showed aberrant morphology were excluded from the analysis.

To determine the distribution of filament angles relative to the leading edge, actin filaments were tracked automatically from tomograms. First, a low-pass filter was applied, followed by application of an automated tracking tool[38]. 0° were designated to filaments growing perpendicular to the leading edge while ± 90° were designated to parallel growing filaments. Filaments below 60-nm length were discarded from the analysis.

***In vivo* migration assay.** Wt and *hem1*$^{-/-}$ mDCs were labelled with 10 μM TAMRA or 3 μM Oregon Green (both Invitrogen) respectively, and vice versa. DCs (1×10^6) at a 1:1 ratio were suspended in 25 μl PBS and injected subcutaneously into hind footpads of 8-week-old, female wt C57BL/6J mice. After 24 h, draining popliteal LNs were harvested and cut with scissors in complete DMEM, supplied with 2.5% FCS, 100 U ml^{-1} penicillin, 100 μg ml^{-1} streptomycin, 2 mM L-glutamine (all Invitrogen) and 10 mM HEPES (Sigma-Aldrich). This was followed by digestion with collagenase D and DNase I in the presence of $CaCl_2$ for 30 min at 37 °C (final concentrations: 3 mM $CaCl_2$ (Sigma-Aldrich), 0.5 mg ml^{-1} collagenase D (Roche), 40 μg ml^{-1} DNase I (Roche) EDTA 0.5 M (Sigma-Aldrich)). The reaction was stopped by addition of 10 mM EDTA. Cells were stained for CD11c and MHCII. Flow cytometry was used to identify injected DCs and their ratios were calculated as the absolute number of wt DCs divided by the absolute number of *hem1*$^{-/-}$ DCs. As control, a 1:1 mixture of oppositely labelled wt DCs was used and quantified accordingly. Lymph nodes with very low numbers of recovered DCs (<100 total) were excluded from the analysis.

***Ex vivo* crawl in assay (end point analysis).** The assay was performed as described previously[6]. In brief, 4–6-week-old female C57BL/6J mice were euthanized, ears were split and the cartilage-free ventral half was used as migration matrix. Wt and *hem1*$^{-/-}$ mDCs were labelled with 10 μM TAMRA or 5 μM CFSE (both Invitrogen), respectively, or vice versa, and mixed at a 1:1 ratio. Cells (6×10^4) were applied to invade the ear tissue for 20 min. Non-invaded cells were washed away and ear explants were incubated at 37 °C/5% CO_2 for 2, 4 or 6 h before fixation with 1% (w/v) paraformaldehyde (Sigma). LVs were immunostained (LYVE1 rat Ab, R&D, donkey anti-rat Alexa 647 secondary antibody, Jackson Immuno Research). Labelled DCs within the explants were visualized using a LSM 700 confocal microscope (Zeiss). Ear sheets with a thick fat layer preventing DCs from reaching LVs or ear sheets that ruptured were excluded from the analysis. The localization of DCs relative to LVs was analysed using ilastik v1.1.5 (http://ilastik.org) for segmentation and a custom-made Matlab script.

Intralymphatic injections of differentially labelled wt and *hem1*$^{-/-}$ mDCs. Wt and *hem1*$^{-/-}$ mDCs were labelled with CFSE or TAMRA (10 μM, Invitrogen) respectively, and vice versa. Male, 7–8-week-old, C57BL/6J mice were anaesthetized by intraperitoneal injection of ketamine (10 mg kg^{-1}) and xylazine (90 mg kg^{-1}). After hair removal, a small incision was cut in the skin below the popliteal fossa and the LV draining the popliteal LN was exposed. A volume of 5 μl of a 1:1 cell mixture (60,000 cells total) was injected into the LV in 5 s pulses at 5 kPa pressure, using a micromanipulator-guided injector (PLI-100A, Warner Instruments). The incision was closed using tissue-adhesive glue (LiquiVet).

Popliteal LNs were harvested 4–4.5 h after intralymphatic injection, fixed in 4% PFA overnight and embedded in paraffin. Sections (3–4 μm thick) were fluorescently stained with Alexa-405-labelled anti-SMA antibody and images were acquired with an LSM 700 inverted microscope. Images were analysed using IMARIS imaging software. Based on the SMA staining the LN area was segmented into a single isosurface. A distance transformation was performed within the isosurface, yielding a new (distance-) channel with intensity values directly corresponding to the distance of the nearest edge of the isosurface. CFSE- and TAMRA-labelled cells were represented as dots and distance-channel intensities were used for quantifying the average migratory distance from the LN edge. Heavily damaged lymph nodes, assessed by morphology, were excluded from the analysis.

***In vitro* 3D chemotaxis assays within differently complex collagen matrices.** Fibrillar rat-tail collagen type I (Becton Dickinson) matrices were reconstituted at pH 7.4 (0.345 N NaOH, 20 μM HEPES/MEM (Sigma)). Matrix densities were obtained by dilution of rat-tail collagen stock solution with 0.01 N HCl. mDCs (3×10^5) were mixed with collagen solutions at a ratio of 1:2. Cell-gel suspensions were cast into custom-made migration chambers and polymerized at 37 °C/5% CO_2. Afterwards, gels were overlaid with CCL19 (0.625 μg ml^{-1}, R&D Systems). DC migration was observed via time-lapse video microscopy. Cells were tracked manually, using the ‘Manual tracking Plug-in’ for ImageJ. The ImageJ Chemotaxis tool was used to determine average (frame-to-frame) speed and chemotactic index (distance in gradient direction/total distance). The average ratio of displacement towards the chemokine source per frame was calculated from average displacements for each genotype, obtained by a custom-made script (determination of displacement towards chemokine source, see below).

Gels that failed to polymerize were excluded from the analysis.

Cell migration in straight and constricted microfabricated channels and microfabricated ‘mazes’. The moulds for straight and constricted PDMS microchannels were a gift from M. Piel (Institut Curie, Paris, France). The dimensions of the straight channels are 5 μm width, 5 μm height. The constricted microchannels contain alternating segments of 7 μm width, 5 μm height and 1.5 μm width, 3 μm height, 10 μm length[21]. A detailed description for manufacturing the ‘maze’ mould can be found on Nature protocol exchange[39].

For device production, a 10:1 elastomer/curing agent PDMS mix (Sylgard 184 Silicone Elastomer Kit, Dow Corning) was poured over the moulds, degassed and cured at 85 °C overnight. Subsequently, devices were carefully peeled off the mould. Holes (2 mm diameter) for chemokine solution and cell suspension were punched on opposite sides of the devices. Subsequently, devices were plasma activated and bonded to glass slides at 85 °C for 1 h. Prior to cell loading, devices were plasma activated and equilibrated in R10 for 1 h at 37 °C, 5% CO_2.

For the ‘maze’ assays, cells were stained with 10 μM TAMRA and one drop of ‘NucBlue’ (both Invitrogen) to follow protrusion dynamics and nuclear position. All devices were loaded with 50,000 wt or *hem1*$^{-/-}$ mDCs (untouched or pre-treated for 30 min with 50 μM blebbistatin, Tocris). For gradient generation, the opposite hole was loaded with 10 μl CCL19 (PeproTech, 2.5 μg ml^{-1}). In the case of blebbistatin treatment, the inhibitor was present in all media to an end concentration of 50 μM. DC migration was observed via time-lapse video microscopy.

The average (frame-to-frame) cell speed in the straight microchannel assays was determined using the ‘Kymograph’ plug-in for ImageJ (http://www.embl.de/eamnet/html/body_kymograph.html). The percentage of cells passing the constriction was calculated from the total number of cells that touch the first constriction and the number of cells that touch and pass the first constriction. The passage time was calculated as the time between frames in which a cell touches the first constriction until it passes and loses contact with the constriction. For the ‘maze’ assays, average (frame-to-frame) cell speed was determined by tracking of the nuclei, using the ImageJ plug-in ‘TrackMate’. To determine the cell area in each frame, cells were first segmented according to the TAMRA signal using ilastik v1.1.5 (http://ilastik.org). This resulted in binary images of the cells. Then, the cell area of single cells and its relative change over time was determined using a custom-made Matlab script.

Samples where cells failed to migrate into the microchannels or the maze were excluded from the analysis.

***In vitro* 3D chemotaxis assays.** Chemotaxis assays were performed as described previously[6]. PureCol bovine collagen (INAMED) in 1× minimum essential medium eagle (MEM, Sigma) and 0.4% sodium bicarbonate (Sigma) was mixed with 3×10^5 iDCs in R10 at a 2:1 ratio, resulting in gels with a collagen concentration of 1.6 mg ml^{-1}. Collagen–cell mixtures were cast in custom-made migration chambers. After 45 min of polymerization of collagen fibres at 37° C/5% CO_2, gels were overlaid with CCL3 (PeproTech, 0.6 μg ml^{-1}). DC migration was observed via time-lapse video microscopy and cells were tracked and analysed as described above. An in-house made algorithm was used to determine the mean square displacement (MSD). Subsequently, the data were fitted to Furths formula to determine persistence time as has been described elsewhere[40]. Gels that failed to polymerize were excluded from the analysis.

Determination of displacement towards chemokine source and average speed. The average displacement of all cells towards the chemokine source was calculated with a custom-made script, employing ImageJ. In brief, cell migration image sequences were background corrected by subtracting the average of the sequence. Particle filtering was used to discard objects smaller or larger than the cells. For each image the lateral displacement that optimizes its overlap with the previous frame was determined.

Finally, the displacement towards the chemokine source was calculated from the optimal y-displacement in pixels, divided by the time between two consecutive frames.

To determine the average speed of iDCs in response to, and in the absence of, chemokine, independently of directionality, image sequences were background subtracted. The colour of the sequence was inverted and a maximum intensity filter of 2 pixels was applied. This yields image sequences that can be automatically tracked with the ImageJ plug-in 'TrackMate'. From automated tracking, the average speed for each time point was determined. The fold increase in speed was determined for wt and *hem1*$^{-/-}$ iDCs by dividing the average speed at each time point in the presence of a CCL3 gradient by the average speed at each corresponding time point without chemokine.

Shape analysis of wt iDCs in 3D collagen gel. Wt iDCs were incorporated into collagen gels as described above. Time-lapse acquisition of z-stacks was performed at 37 °C/5% CO_2, using an inverted wide-field Nikon Eclipse microscope, equipped with a 40×/0.8 DIC objective. ImageJ was used to produce image sequences consisting of standard deviation z projections. Cell outlines were drawn manually to obtain the circularity at each time point. The frame-to-frame speed was calculated from the x–y coordinates of each cell outline centroid.

Statistics and reproducibility. Figures where statistics was used represent pooled data from independent biological replicates as indicated in the figure legends. Appropriate controls were conducted for each biological replicate. All replicates were validated independently and pooled only when all showed the same result. Data were tested for normal distribution and, if necessary, transformed (log transformation in Fig. 2d,f sqrt transformation in Figs 2g and 4c, exponential transformation in Supplementary Fig. 3C) to fulfil the criteria for Student's t-test or ANOVA. The Mann–Whitney test was used for non-normal distributions. All analyses were performed with GraphPad Prism.

No statistical method was used to predetermine sample size. The experiments were not randomized and investigators were not blinded to allocation during experiments and outcome assessment.

For imaging of reporter constructs and SEM, 10–20 cells were observed on two different days. Western blots were carried out twice when no technical problems occurred.

Code availability. The script to determine the average displacement of cells towards the chemokine source is publicly available under: https://datarep.app.ist.ac.at/id/eprint/44.

Data availability. All data that support the conclusions are available from the authors on request.

32. Riedl, J. *et al.* Lifeact: a versatile marker to visualize F-actin. *Nat. Methods* **5,** 605–607 (2008).
33. Lai, F. P. L. *et al.* Arp2/3 complex interactions and actin network turnover in lamellipodia. *EMBO J.* **27,** 982–992 (2008).
34. Benesch, S. *et al.* Phosphatidylinositol 4,5-biphosphate (PIP2)-induced vesicle movement depends on N-WASP and involves Nck, WIP, and Grb2. *J. Biol. Chem.* **277,** 37771–37776 (2002).
35. Steffen, A. *et al.* Sra-1 and Nap1 link Rac to actin assembly driving lamellipodia formation. *EMBO J.* **23,** 749–759 (2004).
36. Behrndt, M. *et al.* Forces driving epithelial spreading in zebrafish gastrulation. *Science* **338,** 257–260 (2012).
37. Small, J. V., Herzog, M. & Anderson, K. Actin filament organization in the fish keratocyte lamellipodium. *J. Cell Biol.* **129,** 1275–1286 (1995).
38. Winkler, C., Vinzenz, M., Small, J. V. & Schmeiser, C. Actin filament tracking in electron tomograms of negatively stained lamellipodia using the localized radon transform. *J. Struct. Biol.* **178,** 19–28 (2012).
39. Leithner, A., Merrin, J., Reversat, A. & Sixt, M. Geometrically complex microfluidic devices for the study of cell migration. *Nat. Protoc. Exchange* http://dx.doi.org/10.1038/protex.2016.063 (2016).
40. Maiuri, P. *et al.* Actin flows mediate a universal coupling between cell speed and cell persistence. *Cell* **161,** 374–386 (2015).

DOI: 10.1038/ncb3426

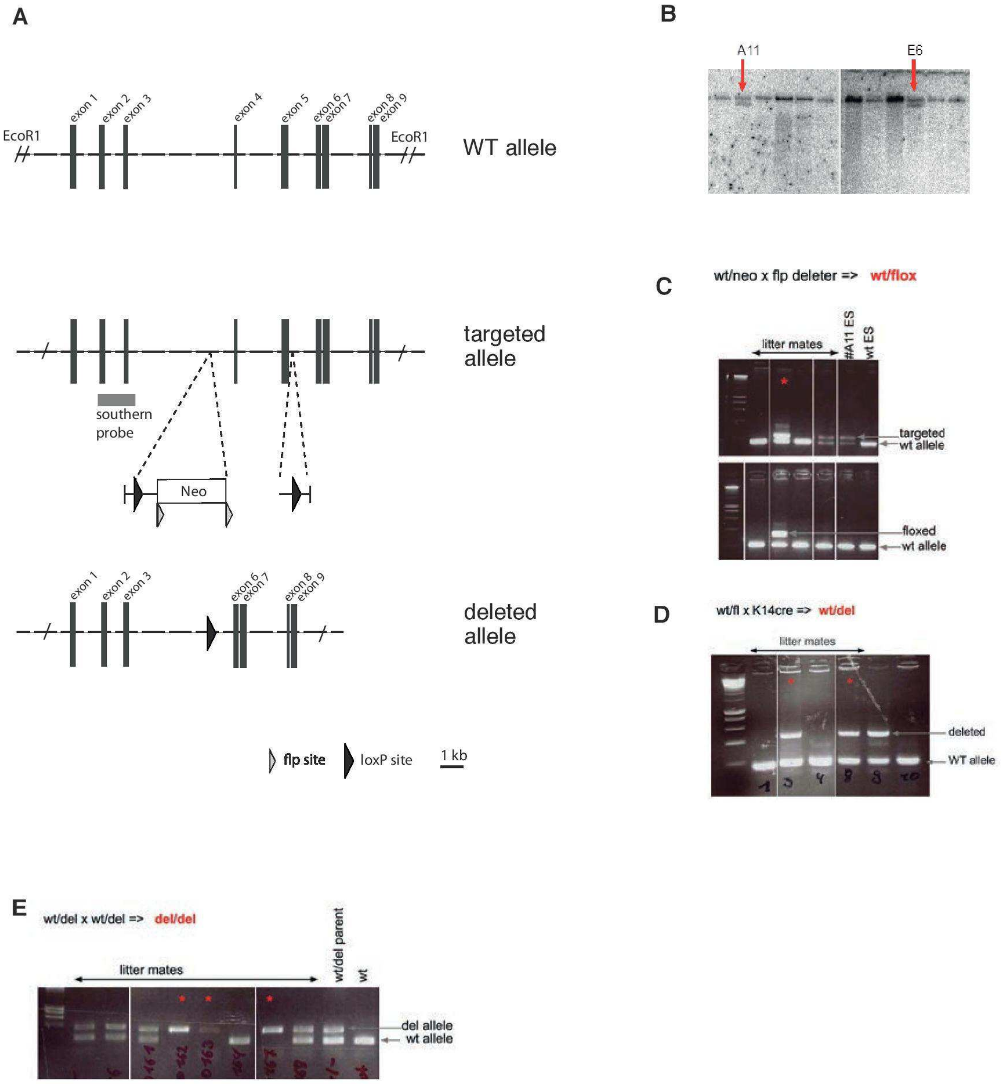

Supplementary Figure 1 Generation of hem1-/- knock-out mice. *Hem1* is located on chromosome 15F3 in the mouse and consists of 31 exons spanning approximately 45 kilobases. (**A**) Exons four and five were flanked by loxP sites, placing an excisable neomycin resistance cassette into the intron before exon 4. A targeting construct harbouring the neomycin cassette (ptHem1-Neo) was used to replace one wt allele in embryonic stem cells (ES line IGD3.2[1]). (**B**) Genomic Southern hybridization and PCR confirmed the presence of the corresponding alleles in isolated ES cell clones. (**C**) ES-cell clone #A11 gave rise to chimeric animals with germ line transmission. Resulting mice harbouring the targeted allele were crossed with a mouse expressing flip-recombinase[2]. Mice carrying the targeted allele and displaying deletion of the neomycin resistance cassette were selected for further backcrossing to C57BL/6J mice until G9. (**D**) Cre-mediated deletion of the targeted allele was achieved by crossing male hem1 fl/wt animals with female Keratin14-cre mice[3] and resulted in animals heterozygously deleted for hem1 (del/wt). (**E**) Heterozygous mice displayed no phenotype and were crossed to produce mice in which *hem1* is deleted on both alleles. For detection of the Hem1 targeted allele, primers b and c (for sequences see Supplementary Table 1.) were used giving rise to products sized 190 bp for wildtype and 220 bp for the targeted allele, respectively. For detecting Hem1 floxed alleles, primers d and e were used to obtain product sizes of 250 bp for wildtype and 350 bp for floxed alleles, respectively. Finally, to detect the deleted allele, primers b, c and e were used, giving rise to a 400 bp product.

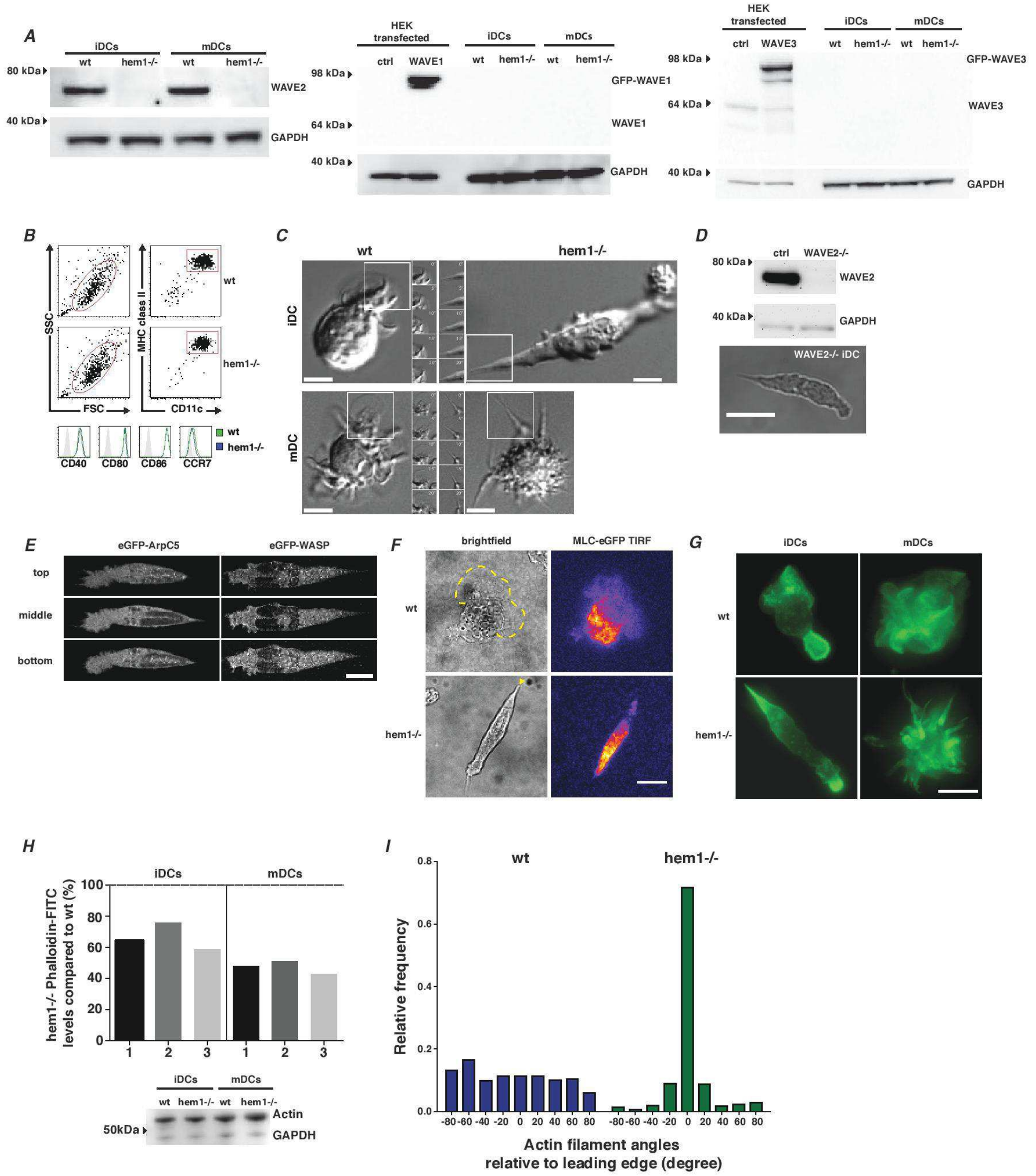

Supplementary Figure 2 Morphological and actin nucleation machinery related characterization of wt and hem1-/- i- and mDCs (**A**) Western Blots of wt and hem1-/- i- and mDC lysates for WAVE 1, 2 and 3. WAVE1/3 – GFP transfected HEK cells were used as positive control for antibodies. GAPDH was used as loading control. In case of WAVE2, blot was consecutively stained for WAVE2 and GAPDH. For WAVE1 and 3 equal sample volumes were loaded on two gels, run together and either stained for GAPDH or WAVE1 or 3. (**B**) Flow cytometry of wt and hem1-/- mDCs for Cd11c, MHCII, CD40, CD80, CD86 and CCR7 levels. (**C**) DIC images of wt and hem1-/- i- and mDCs. Insets show development over 20 sec. of regions marked with white rectangles. Scale bars, 10 µm. (**D**) *top:* Western Blot of control and WAVE2-/- iDCs lysates for WAVE2. GAPDH was used as loading control. Blot was obtained as described for (A). *bottom:* brightfield image shows WAVE2-/- iDC. Scale bar, 10µm. (**E**) Confocal sections of hem1-/- iDCs expressing eGFP-ArpC5 or eGFP-WASP. Scale bar, 10µm. (**F**) Brightfield and TIRF images of wt and hem1-/- iDCs expressing MLC-eGFP. Yellow dotted line marks lamellipodial rim of wt cell. Yellow arrow marks tip of hem1-/- cell. Scale bar, 10µm. (**G**) Representative Z projections of fixed and FITC-phalloidin stained wt and hem1-/- i- and mDCs. Scale bar, 10µm. (**H**) *top:* relative phalloidin-FITC fluorescence levels, measured by flow cytometry, of hem1-/- i- and mDCs compared to wt control. Each bar represents one biological replicate. *bottom:* Western Blots of wt and hem1-/- i- and mDC lysates for total actin. GAPDH was used as loading control. Blot was consecutively stained for Actin and GAPDH (**I**) *Left:* Relative frequency of actin filament angles relative to leading edge in wt (blue) and hem1-/- iDCs (green). *Right:* Automatically tracked actin filaments used to derive data on the left. Black triangles denote position of leading edges. Scale bars, 150nm. Raw data are shown in Fig.1E and F.

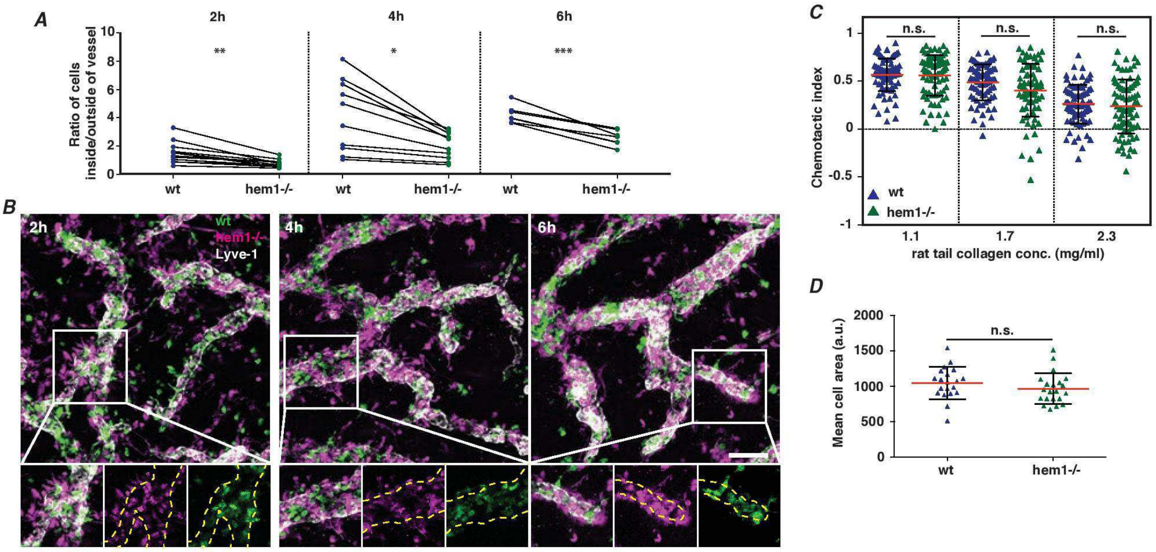

Supplementary Figure 3 Supporting data for mDC *in vivo* and *in vitro* cell migration. (**A**) Ratios of wt and hem1-/- mDCs inside/outside of lymphatic vessels 2, 4 and 6h after application to ear sheets. Blue and green dots, connected with a line represent data from one mouse ear sheet. 2h: Two-tailed t-test, ** P=0.0034. n=12, 4h: Two-tailed t-test, * P=0.0241. n=10, 6h: Two-tailed t-test, *** P=0.0002. All data are pooled from 2 biologically independent experiments. (**B**) Example z-projections of intravasation endpoint assays 2, 4 and 6h after application of wt (green) and hem1-/- (magenta) mDCs, quantified in (**A**). Lymphatic vessels are stained with Lyve-1 (white). Insets: details of regions marked by white squares. Yellow dotted lines mark lymph vessels. (**C**) Single cell chemotactic indices of wt and hem1-/- mDCs in response to CCL19 gradient, depending on increasing rattail collagen concentrations. Mean (red line) ± SD (black bars). Two-tailed t-tests (exponential transformation). 1.1mg/ml: n.s. P=0.9307. n=82 (wt), n=80 (hem1-/-). 1.7mg/ml: n.s. P=0.0587. n=80 (wt), n=81 (hem1-/-). 2.7mg/ml: n.s. P=0.8518. n=81 (wt), n=80 (hem1-/-). Data stem from the same 3 biological replicates as in Fig.2G. (**D**) Mean cell area in arbitrary units of wt and hem1-/- mDCs migrating in microfluidic 'maze' device. Mean (red line) ± SD (black bars). Two-tailed t-test, n.s. P=0.2564. n=20 (wt), n=21 (hem1-/-). Data stem from the same 3 biological replicates as in Fig.3I.

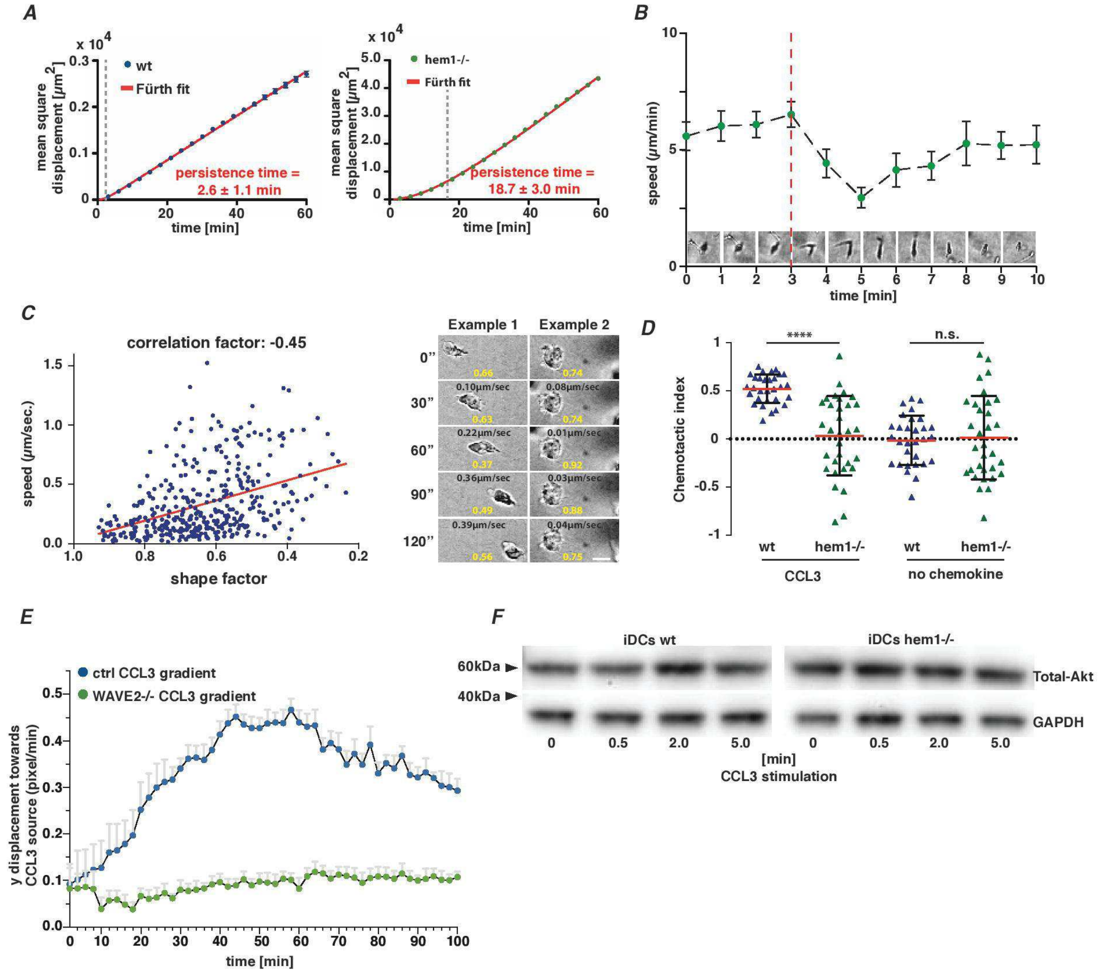

Supplementary Figure 4 Supporting data for iDC *in vitro* cell migration and chemokine sensing. (**A**) Analysis of the mean square displacement (MSD) over time and Fürth fits (red solid line) of wt and hem1-/- iDCs, migrating in 3D collagen gels in Fig. 4A; blue and green circles, average MSD at given time point. (**B**) Speed (µm/min.) of hem1-/- iDCs, migrating in 3D Collagen gel, correlated with cell splitting (appearance of second pointed protrusion) as exemplified in brightfield time-lapse series. Mean (green dot) ± SEM (black bars), n=12. Red dotted line marks time point of splitting events. (**C**) *left:* correlation of frame-to-frame speed (µm/sec.) and shape factor (1= completely round, 0= indefinitely elongated) of wt iDCs, migrating in 3D collagen gel. Red line represents best-fit linear regression. Correlation coefficient = -0.45, **** P<0.0001. n=382 from 34 single cells. *right*: Two example time-lapse series of wt iDCs in collagen gel. Shape factor in respective frame is shown in yellow. (**D**) Single cell chemotactic indices of wt and hem1-/- iDCs, migrating in 3D collagen gel in response or absence of CCL3 gradient. Mean (red line) ± SD (black bars). CCL3: One-way ANOVA, **** P<0.0001. n=30 (wt), n=32 (hem1-/-). No chemokine: One-way ANOVA, n.s. n=30 (wt), n=32 (hem1-/-). Data are pooled from 3 biological replicates. (**E**) Average y-displacement (pixel/min.) over time (min.) of ctrl (blue) and WAVE2-/- (green) iDCs in response to CCL3 gradient. Mean (dots and triangles) ± SEM (black bars). n=6 collagen gels pooled from 3 biologically independent experiments. (**F**) Western blot of wt and hem1-/- iDC lysates from Figure 4G for total-Akt levels after CCL3 chemokine stimulation. GAPDH was used as loading control. Blot was consecutively stained for total Akt and GAPHD.

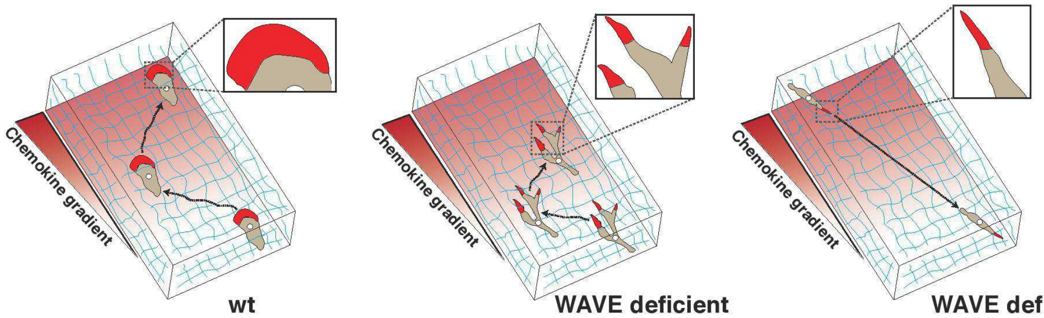

	wt i-/mDCs	WAVE deficient mDCs	WAVE deficient iDCs
Locomotion	+	+	++
Gradient sensing	+	+	+
Navigation	++	+	-

Supplementary Figure 5 Schematic representation of migrating wt and WAVE deficient i- and mDCs. Summary of capabilities of wt and WAVE deficient i- and mDCs regarding (i) general *Locomotion, (ii) gradient sensing* and (*iii)* translation of sensing into *navigation towards chemokine source*. Wt i- and mDCs use their broad lammelipodia to efficiently negotiate complex 3D environments towards the chemokine source. In contrast, the multiple filopodia of WAVE deficient mDCs are inferior in finding optimal paths through complex environments. This slows down cell migration while the basic locomotion and gradient sensing machinery is unaffected. The single, needle shaped protrusion of WAVE deficient iDCs enables high migratory speed but is insufficient to navigate the cell towards chemokine gradients in complex environments.

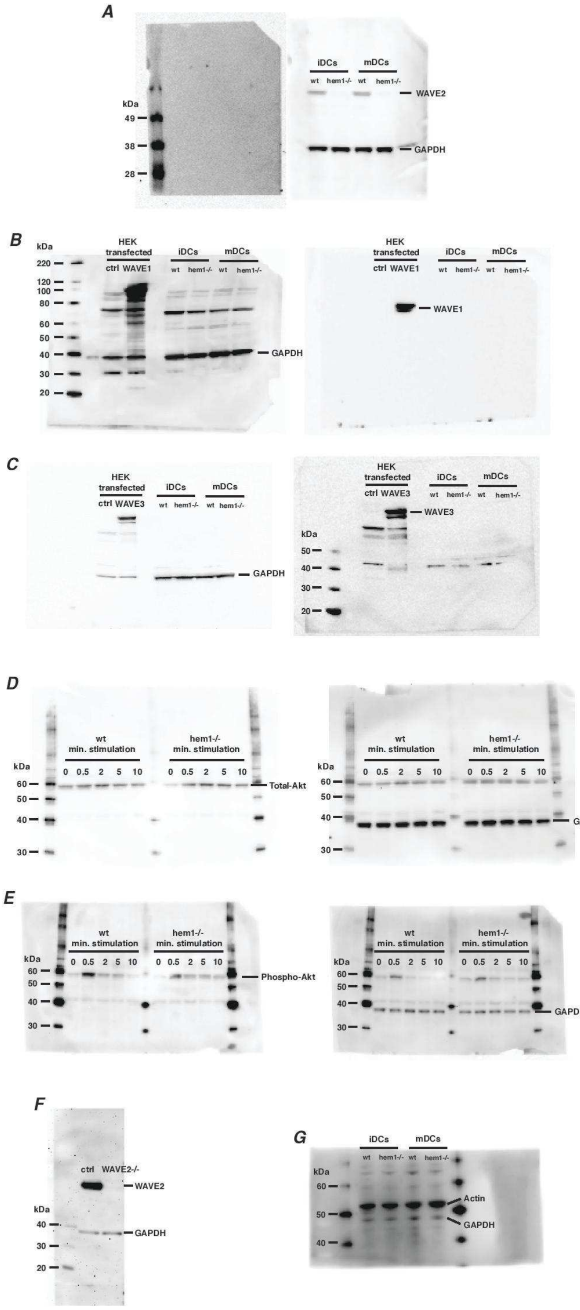

Supplementary Figure 6 Raw data of Western Blots. (**A**) Unprocessed scan of Western Blot for WAVE2 and GAPDH (*right*), shown in Supplementary Figure 2A. *Left:* Marker. (**B**) Unprocessed scan of Western Blot for WAVE1 (*right*) and GAPDH (*left*) shown in Supplementary Figure 2A. (**C**) Unprocessed scan of Western Blot for WAVE3 (*right*) and GAPDH (*left*) shown in Supplementary Figure 2A. (**D**) Unprocessed scan of Western Blot for total Akt (*left*) and GAPDH (*right*) shown in Supplementary Figure 4F. (**E**) Unprocessed scan of Western Blot for phospho-Akt (*left*) and GAPDH (*right*) shown in Figure 4G. (**F**) Unprocessed scan of Western Blot for WAVE2 and and GAPDH shown in Supplementary Figure 2D. (**G**) Unprocessed scan of Western Blot for Actin and GAPDH shown in Supplementary Figure 2H.

Supplementary Table 1. Antibodies & Primers

	Molecule	Isotype	Conjugate	Dilution	Manufacturer	Catalog number	Clone number
FACS antibodies	mouse MHC class II	rat IgG2b κ	eFluor450	1/800	ebioscience	48-5321	M5/114.15.2
	mouse Cd11c	armenian hamster IgG	APC	1/300	ebioscience	17-0114	N418
	mouse CD40	rat IgG2b κ	Biotin	1/200	ebioscience	13-0401	1C10
	mouse CD80	armenian hamster IgG	Biotin	1/200	ebioscience	13-0801	16-10A1
	mouse CD86	rat IgG2b κ	Biotin	1/200	ebioscience	13-0862	GL1
	mouse CCR7	rat IgG2b κ	PE	1/300	ebioscience	12-1971	4B12
	mouse CD16/32	rat IgG2b λ	-	1/100	ebioscience	14-0161	93
	Streptavidin	-	PE	1/400	ebioscience	12-4317	-
Western Blot antibodies	WAVE1	goat IgG	-	1/200	Santa Cruz	sc-10388	polyclonal
	WAVE2	mouse IgG	-	1/10	Innocenti et al., 2004	-	2236.1
	WAVE3	rabbit IgG	-	1/1000	Cell signaling	2806S	polyclonal
	Akt	rabbit IgG	-	1/1000	Cell signaling	4691	C67E7
	phospho-Akt	rabbit IgG	-	1/2000	Cell signaling	4060	D9E
	Actin	rabbit IgG	-	1/500	Cytoskeleton	AAN01	polyclonal
	GAPDH	mouse IgG1	-	1/3000	abcam	ab125247	GA1R
	anti-Rabbit	goat IgG	HRP	1/5000	Bio Rad	170-6515	polyclonal
	anti-Mouse	goat IgG	HRP	1/5000	Bio Rad	170-6516	polyclonal
	anti-Goat	donkey IgG	HRP	1/3000	Santa Cruz	sc-2020	polyclonal
Mouse ear assays	LYVE1	rat IgG2a	-	1/300	R&D	MAB2125	223322
	anti-Rat	donkey IgG	Alexa 647	1/200	Jackson Immuno Research	712-605-153	polyclonal

Primers	**Name**	**Sequence (5' --> 3')**
	b	CGAGCTTTGGTTAGAAATAGCC
	c	ATGTCTACATGGGTGTGTTGG
	d	AAAGATTTTGAAAGTTCTCCATGC
	e	GGTTGCTTCTGGATTTGAGC

Supplementary Table 1 Antibodies and Primers

Supplementary Video Legends

Supplementary video 1 Total internal reflection (TIRF) movies of iDCs migrating on PLL-PEG coated cover slip under agarose in a CCL3 gradient. Cells are expressing eGFP reporters for ArpC5, WASP and Abi1. ArpC5 and Abi1 localize to the lamellipodial edge in phases of expansion while WASP is absent from the leading edge. Time-laps over 180 sec. (60 frames, 12 frames/sec.)

Supplementary video 2 Total internal reflection (TIRF) movies of mDCs migrating on PLL-PEG coated cover slip under agarose in a CCL19 gradient. Cells are expressing eGFP reporters for Lifeact, ArpC5, WASP and Abi1. ArpC5, WASP and Abi1 localize to the lamellipodial edge in phases of expansion. Time-laps over 180 sec. (60 frames, 12 frames/sec.)

Supplementary video 3 Wt and hem1-/- i- and mDCs in suspension, imaged with differential interference contrast (DIC) microscopy. Hem1-/- iDCs have a pointed, needle-like shape while their wild-type (wt) counter parts display a roundish morphology with veil-like lamellipodia. Hem1-/- mDCs round up like their wt counter parts but instead of displaying pronounced lamellipodia they form multiple, finger-like extensions. Time-laps over 1 min. (61 frames, 10 frames/sec.)

Supplementary video 4 Electron tomography of the lamellipodium of a wt iDC. The image series shows a z-stack, followed by a close-up, showing branched actin filaments (red circles). Branch junctions are then marked in red, actin filaments radiating from these points are marked in green.

Supplementary video 5 Electron tomography of the tip of a hem1-/- iDC. The image series shows a z-stack, followed by a polarity analysis of actin filaments. Actin filaments are marked in green, red spheres denote barbed filament ends, showing a linear array of parallel filaments.

Supplementary video 6 Wt mDCs migrating in 3D collagen gel towards a CCL19 gradient. Individual cell tracks within the first 60 min. are marked by different colors. Time-laps over 180 min. (61 frames, 12 frames/sec.). The sequence is followed by a close up of an individual wt mDC migrating in a 3D collagen gel towards a CCL19 gradient. Time-laps over 60 sec. (60 frames, 12 frames/sec.).

Supplementary videoe 7 Hem1-/- mDCs migrating in 3D collagen gel towards a CCL19 gradient. Individual cell tracks within the first 60 min. are marked by different colors. Time-laps over 180 min. (61 frames, 12 frames/sec.). The sequence is followed by a close up of an individual hem1-/- mDC migrating in a 3D collagen gel towards a CCL19 gradient. Time-laps over 60 sec. (60 frames, 12 frames/sec.).

Supplementary video 8 Wt (left) and hem1-/- (right) mDCs migrating in microfluidic 'maze' device towards a CCL19 gradient. Cell bodies are stained with 10μM TAMRA. Nuclei are stained with NucBlue nuclear dye. Time-laps over 100 min. (100 frames, 12 frames/sec.).

Supplementary video 9 Wt iDCs migrating in 3D collagen gel. Time-laps over 60 min. (61 frames, 12 frames/sec.).

Supplementary video 10 Hem1-/- iDCs migrating in 3D collagen gel. Time-laps over 120 min. (61 frames, 12 frames/sec.). The movie also shows examples of the following immature hem1-/- iDC traits: (1) High persistence, (2) Change of direction upon rounding and (3) bifurcations and spiking, followed by a close-up of a migrating hem1-/- DC.

Supplementary video 11 Brightfield and total internal reflection (TIRF, red) microscopy movies of a individual Lifeact-eGFP expressing (1) mDC (time-laps over 170 sec., 18 frames), (2) T cell (time-laps over 117 sec., 40 frames) (3) neutrophil (time-laps over 100 sec., 26 frames) and *D.rerio* keratocyte (time-lapse over 120 sec. 59 frames). Cells are migrating confined under a PLL-PEG coated 4μm micropillar, except *D.rerio* keratocyte that is migrating on a coverslip. In mDCs, T cells and neutrophils the lamellipodium is rarely visible in the TIRF channel (red). This suggests that it is not involved in force transduction. Instead, the cell body itself seems to be the main driver of locomotion. In contrast, the lamellipodia of keratocytes are in tight contact with the substrate, visualized by a constant TIRF signal in the lamellipodium. (12 frames/sec.)

Supplementary video 12 Time-lapse spinning disc confocal z-projection (center) and z-reconstructions (oblique top/bottom- and front view) of eGFP-Abi1 expressing mDC, migrating confined under a 3μm micropillar (time-lapse over 200 sec. 21 frames). The lamellipodium, highlighted by a strong eGFP-Abi1 signal, is not in constant contact with the upper or lower substrate. Instead it shows a highly dynamic, fluctuating behavior. (12 frames/sec.)

References:

1. Hitz, C., Wurst, W. & Kühn, R. Conditional brain-specific knockdown of MAPK using Cre/loxP regulated RNA interference. *Nucleic Acids Res.* **35,** (2007).
2. Rodríguez, C. I. *et al.* High-efficiency deleter mice show that FLPe is an alternative to Cre-loxP. *Nat. Genet.* **25,** 139–140 (2000).
3. Hafner, M. *et al.* Keratin 14 Cre Transgenic Mice Authenticate Keratin 14 as an Oocyte-Expressed Protein. *Genesis* **38,** 176–181 (2004).

3.6 Discussion

In the here presented study, we employed cells with one-, multiple or sheet like protrusions to study their respective role in 3D migration and chemotaxis of leukocytes. We achieved this by exploiting a potentially unique setting in DCs in which WAVE is the sole NPF of Arp2/3 mediated actin branching at the leading edge in immature cells. Under wt conditions, DCs form multiple, sheet-like lamellipodia in their immature- and mature state. However, when the WAVE complex is depleted, this yields cells with only one, needle-like filopodium at the leading edge. Upon maturation, WAVE depleted cells round up and form multiple filopodia. Potentially this is mediated by WASP, which in contrast to the situation in iDCs, localizes to the leading edge of mDCs. Another non-mutually exclusive explanation might be maturation-induced up-regulation of Fascin [26], potentially leading to increased bundling and filopodia formation. Challenging these cells in *in vitro* and *in vivo* settings of varying environmental complexity revealed a surprising role of protrusions in leukocyte migration.

Interestingly, the lamellipodium of leukocytes rarely contacts the substrate but instead undulates in free space, as if scanning the surrounding environment. Additionally, mDCs, which form multiple filopodia, have no cell speed defects in linear channels, suggesting that the lamellipodium has no role in locomotion per se. This stands in sharp contrast to mesenchymal migration where the lamellipodium is an adhesive structure to build new FAs that are used for force transduction. Strikingly, WAVE deficient mDCs begin to show cell speed defects in more complex environments, coinciding with reduced protrusion dynamics while there is no effect on chemotaxis. However, iDCs that only migrate with a single filopodium are unable to interpret chemokine gradients while they show strongly increased migratory speed and persistence. Taken together, these data suggest that protrusions in DCs decrease the speed of cell migration but serve to explore and negotiate complex environments with lamellipodia being superior to multiple filopodia. However, the data suggest that there is no difference in their ability to sense and integrate chemokine gradients. As long as protrusions are *diversified* chemokine gradients can be interpreted with similar high efficiency as opposed to the *single* filopodium of iDCs that fails to mediate chemotaxis.

Our data were partially confirmed by a shortly predating study, showing that mDCs migrate with increased speed, compared to iDCs and that these differences are attributable to two different F-actin pools. In iDCs, Arp2/3 primarily polymerizes F-actin at the front whereas mDCs have a large F-actin pool at the back that is mDia1 dependent. Inhibition of Arp2/3 in iDCs leads to redistribution of F-actin to the back and to an increase in cell speed, comparable to our observations with WAVE deficient iDCs [27]. However, according to this study Arp2/3 deficient mDCs have no disadvantage in terms of cell speed in collagen gels or entry into lymphatic vessels. This stands in stark contrast to our results, especially because an even stronger phenotype would be expected when Arp2/3 itself is inhibited. One explanation might be the different cell sources. While we employ a mouse model where WAVE is constitutively removed in the hematopoietic lineage, drug treatment or tamoxifen inducible removal of Arp2/3 in DC cultures is used in the mentioned study. Potentially, this leads to only incomplete inhibition of Arp2/3 mediated actin branching. Alternatively, the absence of WAVE in our model might lead to deregulation of Arp2/3, resulting in phenotypes that are absent in acute Arp2/3 inhibition. However, in our manuscript knockout of WAVE merely serves as a tool to study the different roles of protrusion types in DC migration. Therefore, it would be first necessary to look at the morphology of Arp2/3 inhibited cells, which has not been reported by Vargas et al. [27]. This would determine if comparable changes in protrusion morphology even exist in these cells, which stand at the base of our study.

Another recent study in macrophages finds that Arp2/3 depletion leads to a more elongated cell shape with multiple filopodia protruding from the leading edge. These cells migrate with slightly increased speed and retain chemotaxis, showing a mixture of phenotypes we observed for i- and mDCs respectively. In contrast, Arp2/3 deficient macrophages are unable to follow haptotactic gradients. These observations are explained by incomplete integrin signaling with intact outside-in but defective inside-out signaling, which requires Arp2/3 mediated actin branching. Consequently, cells are not adhesive enough to interpret surface bound gradients but are faster due to reduced adhesion stability [28]. However, a direct comparison between our studies is difficult since all migration assays were performed in integrin dependent 2D assays, which we did not include in our study.

Finally, another study employing lattice light sheet microscopy, provides further support for the idea of free moving, non-substrate bound leading-edge protrusions in leukocytes, serving as space exploratory structures. HL-60 neutrophils form multiple lamellar elements that eventually converge to build larger rosette-like structures. Importantly, these structures are also formed on the dorsal side of cells migrating in 2D, where they make no contact with the substrate and ‘probe’ their surrounding environment in 3D collagen gels. Consequently, Arp2/3 inhibition in these cells results in reduced lamellar protrusion formation, accompanied by a decrease in cell turning and reduced speed of migration [29].

In summary, although the exact phenotypes might differ depending on the cell type and experimental settings, Arp2/3 interference reveals that leading edge protrusions in leukocytes are adapted to serve as space exploratory organs in complex 3D environments. Consequently, force transduction for locomotion is not generated in the lamellipodium, as in mesenchymal migration, but in the cell body. Future research should aim to determine how this force is generated and how it is coupled to the environment.

4 Immortalized hematopoietic precursor cells – a genetically tractable tool for the study of dendritic cell biology

The study of DC biology relies on the ability to create large numbers of cells *in vitro*. Typically, DCs are differentiated from un-fractioned murine bone marrow (BM DCs) in the presence of granulocyte-macrophage colony stimulating factor (GM-CSF) on non-tissue culture treated petri dishes [30],[31]. Within one week, the result is a non-adherent, terminally differentiated population of immature DCs (iDCs). Upon lipopolysaccharide (LPS) treatment, these cells are activated and become mature DCs (mDCs), characterized by high Cd11c and MHCII levels.

BM DCs have been used in a plethora of studies, shedding light on a variety of biological processes such as antigen processing and presentation and cell migration. However, due to the short life span and terminal differentiation of BM DCs, genetic modifications, such as knockouts or knockins, are very difficult to achieve. Therefore, research in DC biology largely depends on the time- and resource-consuming generation of new genetically modified mice that serve as a source for the generation of BM DCs. To circumvent this problem, several attempts have been made to create stable DC cultures or cell lines, all with their own advantages and disadvantages. However, due to different experimental requirements (such as the ability to migrate or to present antigen), no standard cell line based DC model has emerged.

Recently, exploitation of the prokaryotic clustered regularly interspaced short palindromic repeats (CRISPR)/ CRISPR associated (Cas) system lead to substantial progress in the field of genome editing [32]. Potentially, combination of one of the above mentioned DC cell lines or long term cultures, combined with CRISPR/Cas9 mediated genome editing, might have the potential to generate a tractable platform for the study of DC biology.

The following sections will give an overview over existing DC cell lines, the CRISPR/Cas9 technology and formulate aims for the here presented study.

4.1 DC long-term cultures and cell lines

The generation of DC long-term cultures or cell lines follows three main approaches. These are: (1) growth factor dependent long-term culture of spleen derived DCs, (2) immortalization of DCs with oncogenes and (3) immortalization of a precursor that can be differentiated into DCs.

In the first approach, DCs are differentiated from spleen suspensions in the presence of GM-CSF and fibroblast supernatant. These cells, termed D1 cells, can be grown in culture for months. Treatment with bacterial compounds leads to up-regulation of DC maturation markers and the ability to present antigen to naïve T cells. Migratory properties have been reported but to date have not been compared with GM-CSF

BM DCs [33]. Additionally, it has been shown that these cells can be infected with retroviruses without affecting their maturation state [34].

In the second approach, DCs are immortalized by the expression of oncogenes such as simian-virus 40 large T antigen (SV40). In one study, BM from a mouse with tetracycline inducible SV40 is used to differentiate GM-CSF DCs. Addition of doxycycline to the culture results in a change of morphology to small rounded cells that can be further propagated. Upon doxycycline removal these cells revert back to their DC-like shape and properties [35]. Another study shows immortalization of splenic DCs by SV40 nucleofection, followed by selection of single clones with a DC surface marker expression profile [36]. Cells from both studies mature upon LPS stimulation and are capable to prime naïve T cells. The probably best characterized SV40 based DC cell line is derived from spleen tumors that develop in mice expressing SV40 under the DC specific Cd11c promotor. Isolation, dissociation and cultivation of tumor cells leads to spontaneous immortalization of cells, termed mutuDCs. These cells are closely related to conventional spleen DCs in terms of marker expression, their response to bacterial compounds and their proteome. Additionally, mutuDCs can be genetically modified by lentiviral infection [37]. However, as these cells grow adherently and become even more adherent upon maturation (personal observation) it is highly unlikely that they are able to recapitulate the highly migratory properties of BM DCs. Lastly, sequential infection with retroviruses coding for GM-CSF and *myc* plus *raf* respectively, of BM has been reported to result in DC immortalization. Again these cells can undergo maturation and antigen presentation [38].

The third approach relies on the generation of a stable cell line that serves as a source for the generation of DCs, thereby circumventing the regular use of mice as organ donors. Embryoid bodies, derived from a certain embryonic stem cell (ES) line, cultivated in the presence of GM-CSF and interleukin 3 (IL-3) have been shown to continuously give rise to DCs that respond to maturation stimuli and that are able to prime naïve T cells [39]. Additionally, transgenes that have been transfected into ES cells are retained in the resulting DCs without affecting their ability to mature [40].

Another approach is the conditional immortalization of hematopoietic precursors. To this end, an estrogen-regulated form of the homeobox transcription factor b8 (Hoxb8), shown to increase self-renewal and to arrest cell differentiation, is retrovirally delivered to hematopoietic precursors of the BM in the presence of GM-CSF. Upon estrogen withdrawal and differentiation these cells to some degree resemble DCs but crucially lack the ability to prime naïve T cells [41]. However, when GM-CSF is replaced with fms like tyrosine kinase 3 (Flt3) ligand during immortalization and maintenance the resultant cells, termed Hoxb8-FL cells, have the potential to differentiate to DCs that very closely resemble their BM GM-CSF derived counterparts. Importantly, Hoxb8-FL cells, also have the capability to differentiate into other cell types of the myeloid and lymphoid lineage such as macrophages and

B cells, depending on the culture conditions. Furthermore, they are temporarily capable to reconstitute lethally irradiated mice [42].

4.2 The CRISPR/Cas sytem for genome engineering

The CRISPR/Cas system is a prokaryotic adaptive immune system against plasmids and viruses. It is based on the incorporation of short sequences, called spacers, of the intruders DNA into arrays of the prokaryotic genome, interrupted by short palindromic repeats [43]. Spacers are transcribed into non-coding CRISPR RNAs (crRNAs) that hybridize with a second, non-variable trans-activating CRISPR RNA (tracRNA). Together, they form a complex with proteins of the Cas family and direct them against regions of foreign DNA that are complementary to the crRNA and that are adjacent to a short protospacer adjacent motif (PAM). There, certain Cas proteins exert their nuclease function and cleave the DNA by introducing double-strand breaks (DSBs) in a process termed DNA interference. In prokaryotes, three different CRISPR/Cas subgroups, termed type I, II and III, can be distinguished, based on the presence of signature Cas proteins and phylogenetic information. Whereas type I and III systems require formation of protein complexes, DNA interference in type II systems is solely mediated by Cas9, which recognizes PAMs of the sequence NGG [43]. Consequently, type II systems, mainly derived from *Streptococcus pyogenes* have been adapted for biotechnological applications [32]. In its most widely used form only two components, a guide RNA (gRNA) that is a fusion of the variable crRNA and the invariable tracRNA and Cas9 that recognizes PAMs of the sequence NGG, have to be expressed for the system to be functional in eukaryotic cells. Cas9 can be directed to any region of choice specified by the gRNAs sequence, its only prerequisite being an adjacent PAM in the target region, where it introduces a DSB three nucleotides in 5’ direction from the PAM. DSBs are frequently resolved by the non-homologous end joining (NHEJ)- or to a lesser extent by the homology directed repair (HDR) pathway [44]. NHEJ introduces insertion/deletion mutations of variable length that may lead to gene knockouts e.g. by altering the reading frame, leading to a pre-mature stop codon. HDR on the other hand might induce point mutations or can be used to knock-in reporters such as GFP to tag endogenous genes, provided that DNA containing the desired information can be delivered to the cell. As NHEJ is much more frequent, knock-outs are in general easier to achieve but several methods have been developed to shift the NHEJ-HDR balance to increase the chance of knock-ins e.g. by inhibition of the NHEJ pathway or by synchronization of the cell cycle [44]. Potential off-target effects are considered to be a major caveat of the CRISPR/Cas9 technology. While their frequency and occurrence remains difficult to predict, several studies aim to avoid- or at least reduce off target effects by employing a wide range of methods. This ranges from titrating gRNA-Cas9 ratios to the development of algorithms that aim to identify gRNAs with a low off-target effect probability, based on observed off-target effects with varieties of gRNAs for the same target but with mismatches at varying positions [45],[46]. Furthermore, mutation of certain amino acid residues has lead to the development of Cas9 variants with increases specificity that might reduce potential off-target effects [47].

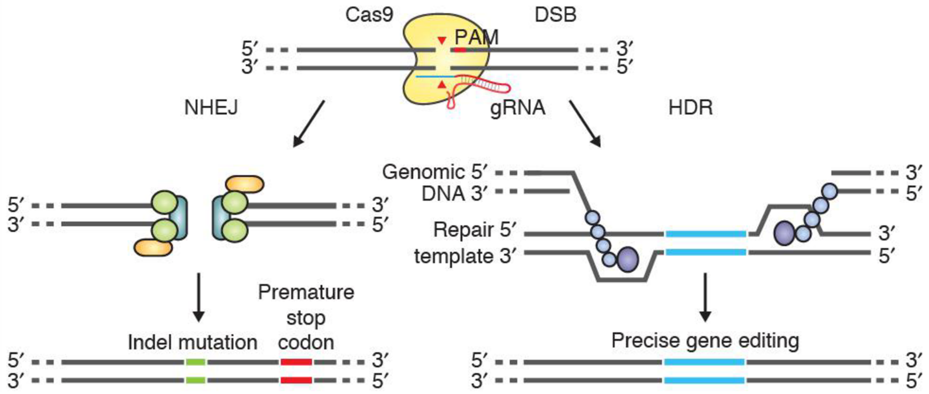

Figure 5. **Repair pathways of CRISPR/Cas9 mediated double strand breaks.** DSBs caused by Cas9 are either resolved via the NHEJ- or the HRD pathway. NHEJ will cause indel mutations that might lead to a premature stop codon and eventually a gene knockout. Provided a DNA template is present, HDR can be exploited to introduce single point mutations or to tag endogenous genes with reporters. Modified after Ran et al., 2013.

4.3 Aims

As pointed out earlier, research in DC biology is hampered by the low genetic tractability of its standard model system, BM derived GM-CSF DCs. Additionally, the routine sacrifice of mice to serve as BM donors is not only resource consuming but also asks for technical improvements in line with the 3R principles (replace, reduce, refine) of ethical animal usage. Consequently, the aim of this study is the development of a genetically tractable, cell culture based system for the study of DC biology that complements and/or replaces the classic derivation of GM-CSF DCs from mouse BM. We solely focus on Hoxb8-FL cells [42], as DCs differentiated from these cells are very similar to BM GM-CSF DCs in terms of marker expression and their ability to prime naïve T cells. Additionally, Hoxb8-FL cells can differentiate into other cell types of the myeloid and lymphoid lineage, which potentially makes the system also valuable for the study of other immune cells. As described earlier, several DC cell lines or long-term cultures exist but the ability to migrate, one of the key properties of DCs, has in general not been described and we failed to induce migration in all cell lines that we tested (personal observation). Therefore, special attention is paid to thoroughly characterize the migratory properties of Hoxb8-FL DCs in comparison to BM DCs. This is followed by proof of principle experiments to demonstrate that knockouts can be generated in Hoxb8-FL cells via the CRISPR/Cas9 system while retaining the cells ability to differentiate to DCs.

4.4 Results – *'Fast and efficient genetic engineering of hematopoietic precursor cells for the study of dendritic cell migration' – manuscript accepted by the 'European Journal of Immunology'*

Dendritic cells (DCs) are sentinels of the adaptive immune system that reside in peripheral organs of mammals. Upon pathogen encounter, they undergo maturation and up-regulate the chemokine receptor CCR7 that guides them along gradients of its chemokine ligands CCL19 and 21 to the next draining lymph node. There, DCs present peripherally acquired antigen to naïve T cells, thereby triggering adaptive immunity [1],[48]. Their high migratory speed and chemotactic prowess, the relative ease in generating large cell numbers in culture and their suitability for *in vitro* and *in vivo* assays has made DCs one of the most powerful tools to study cell migration [49]. Typically, DCs are differentiated from unfractionated bone marrow (BM) in the presence of differentiation-promoting factors such as granulocyte-macrophage colony stimulating factor (GM-CSF) [30]. Once mature, these terminally differentiated BM DCs have a very limited life span, impeding stable genetic modifications. Consequently, research is hampered by time- and resource consuming generation of genetic mouse models.

To overcome these limitations, several methods have been developed to obtain long-term DC cultures. This has been either achieved by differentiation of DCs from embryoid bodies [40], oncoprotein driven immortalization of DCs [6]–[9], or growth factor dependent, long-term culture of splenic DCs [10]. Although migratory properties are considered to be one of the hallmarks of DC biology, we never observed efficient migration in any of these cultures (personal observation).

Recently, Flt3L expanded hematopoietic precursors, transiently immortalized via a retrovirally delivered, estrogen inducible form of the transcription factor Hoxb8 have been introduced (Hoxb8-FL cells) [11]. Upon estrogen withdrawal and GM-CSF culture the resulting DCs closely resemble BM DCs in their transcriptome, cytokine secretion and priming of naïve T cells (Fig. 1A) [11].

For direct comparison we differentiated DCs from BM and Hoxb8-FL cells side-by-side in the presence of GM-CSF [4]. Cells from both origins expressed high levels of the DC markers Cd11c and major histocompatibility complex II (MHCII, Fig. 1B). Importantly, Hoxb8-FL DCs expressed CCR7 [2], albeit at slightly lower levels as compared to BM DCs (Fig. 1B). When incorporated into 3D collagen gels [12] and recorded by time-lapse video microscopy both fractions showed vivid protrusion dynamics and migrated persistently for several micrometers before rounding up and changing direction (Supplementary movie 1). Migratory speeds of Hoxb8-FL DCs were slightly reduced as compared to BM DCs (Fig. 1C). When exposed to gradients of CCL19, HoxB8-FL DCs showed a strong chemotactic response with a slightly reduced chemotactic index compared to BM DCs, potentially attributable to lower levels of CCR7 (Fig. 1D, E and Supplementary movie 1). Finally, we co-injected differently labeled DCs of both origins into mouse footpads and found that they arrive in comparable numbers in the popliteal lymph node 24h after injection (Fig.1F). Taken together, Hoxb8-FL DCs showed robust migratory behavior and chemotaxis *in vitro* and *in vivo*.

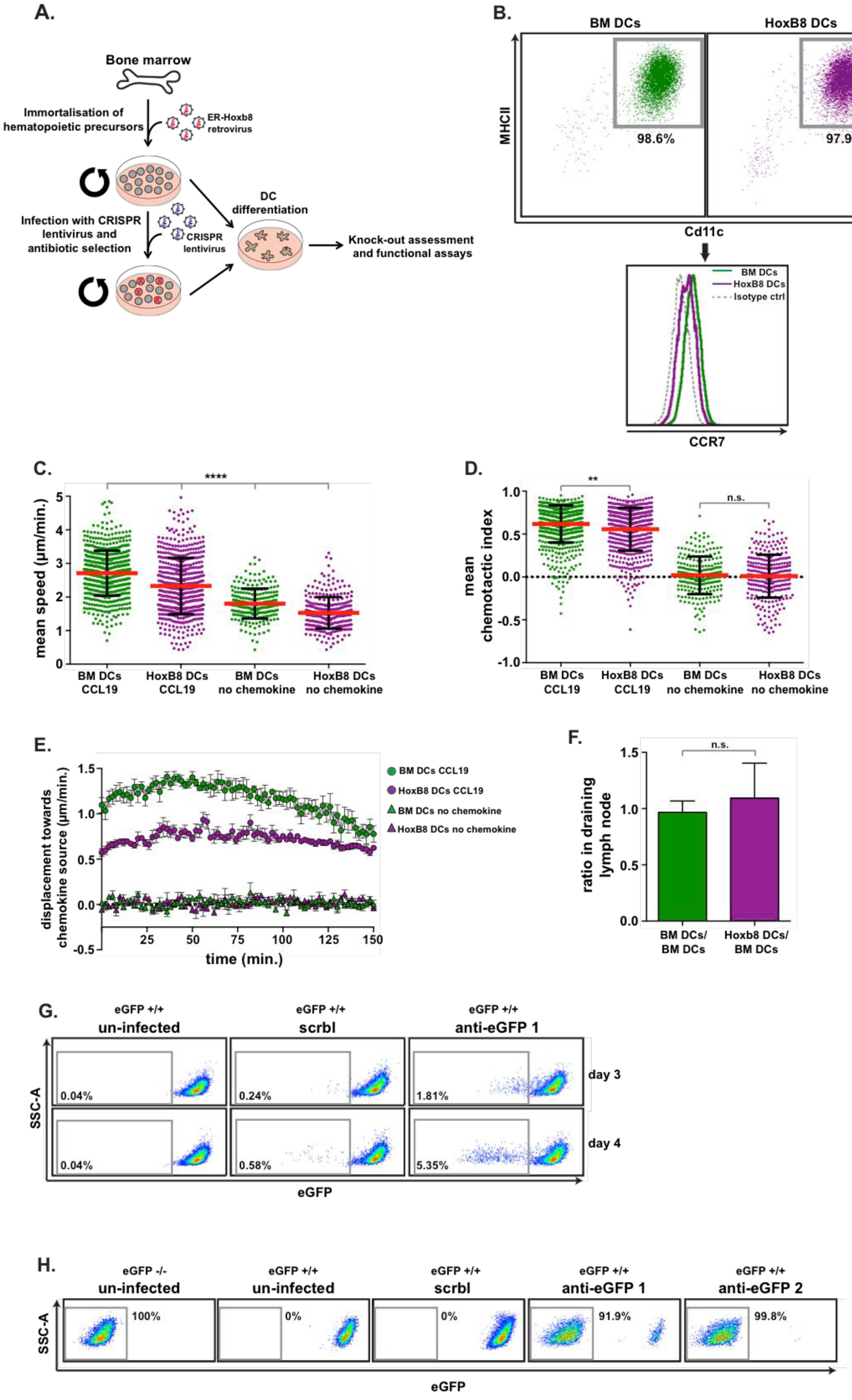

Figure 6. Migratory properties of BM- and Hoxb8-FL DCs in vitro and in vivo. (**A**) Schematic of generation, maintenance, LentiCRISPR infection and differentiation to DCs of Hoxb8-FL cells (**B**) FACS staining of DCs for Cd11c, MHCII and CCR7. CCR7 levels are pre-gated on Cd11c/MHCII high population (grey boxes). (**C**) Mean single cell speeds (μm/min.) of DCs migrating in 3D collagen gels in presence or absence of CCL19 gradient. Mean (red line) ± s.d. (black bars). Kruskal-Wallis test, **** P<0.0001, n=663/567 (BM-/Hoxb8 DCs CCL19), n=235/299 (BM-/Hoxb8 DCs no chemokine), pooled from 3 biologically independent experiments. (**D**) Mean single cell chemotactic indices of cells in (**C**). Kruskal- Wallis test, ** P<0.01. (**E**) Average y-displacement (μm/min.) over time (min.) of BM- and Hoxb8-FL DCs in the presence (circles) or absence (triangles) of CCL19 gradient. Mean (dots/triangles) ± s.e.m. (black bars). n=6 collagen gels (CCL19) or n=3 collagen gels (no chemokine), pooled from 3 biologically independent experiments. (**F**) Ratio of DCs in draining lymph node 24h after injection. S.d. (black bars). unpaired t-test, not significant, P=0.3415. n=6 (BM/BM) or n=17 (Hoxb8/BM), pooled from 2 biologically independent experiments. (**G**) eGFP expression levels of mG Hoxb8-FL cells 3 or 4 days after infection with indicated lentiviruses. (**H**) eGFP expression levels of mG or ctrl Hoxb8-FL cells after infection with indicated lentiviruses and antibiotic selection.

Next, we set out to probe this system's tractability for genetic modifications via the CRISPR/Cas9 system. As a proof of principle we first assessed if a fluorescent reporter (GFP) could be deleted in undifferentiated Hoxb8-FL cells. Hoxb8-FL cells, homozygous for membrane GFP (mG), were infected with lentiviruses coding for puromycin resistance, Cas9 and a guide RNA (gRNA) [13] directed against GFP (anti-GFP-1 or 2) or a scrambled (scrbl) control. GFP negative cells could be detected 3 to 4 days after infection while negligible signal was detected in the GFP negative gate of scrbl infected cells (Fig. 1G). To determine the efficiency of the CRISPR/Cas9 system in Hoxb8- FL cells, we exposed infected mG cells to antibiotic selection and expanded survivors. We found that more than 90% of mG cells infected with gRNA anti- GFP-1 were GFP negative. For gRNA anti-GFP-2 this effect was even stronger, with almost 100% of cells in the GFP negative gate. In contrast, mG cells infected with the scrbl gRNA lentivirus retained their fluorescence (Fig. 1H). These results demonstrate that CRISPR/Cas9 mediated genome editing in HoxB8-FL progenitors is highly efficient.

Next, we wanted to explore if activity of the CRISPR/Cas9 system interferes with the ability of Hoxb8-FL cells to differentiate to DCs and if endogenous genes can be targeted with comparable efficiency. Initially, we focused on the gene *Itgb2*, coding for the leukocyte specific integrin beta 2. Together with integrin alpha x it forms the trans-membrane heterodimer DC marker Cd11c. Beta 2 integrins mediate cell-substrate adhesions and couple the contractile force of the cytoskeleton to the environment [14]. We designed three different gRNAs (anti-*Itgb2*-1-3) directed against *Itgb2*, produced lentiviruses and infected HoxB8-FL cells. After antibiotic selection, cells were expanded and differentiated to DCs. Putative *Itgb2* knockout and control cells were morphologically indistinguishable in suspension (data not shown) and cells infected with the scrbl gRNA showed high Cd11c and MHCII levels (Fig. 2A). DCs derived from cells infected with anti-*Itgb2* showed no Cd11c staining, while retaining high MHCII levels (Fig. 2A). To obtain a functional read-out we coated glass-slides with CCL21, which triggers integrin beta 2 dependent adhesion, polarization and migration trough CCR7 [15]. DCs derived from anti-*Itgb2* Hoxb8-FL cells failed to adhere to CCL21 coated glass slides (Fig. 2B, C and Supplementary movie 2).

As a second endogenous candidate we chose chemokine receptor CCR7. We designed three, *ccr7* specific- (anti-*ccr7*) and one scrambled control gRNA. As in the above-described experiments we observed a relatively low number of infected Hoxb8-FL cells surviving puromycin selection, we compared blasticidin as an antibiotic marker and found that survival rates are increased (data not shown). DCs from all infections showed normal Cd11c and MHCII levels (Fig. 2D). Importantly, cells from all anti-*ccr7* infections showed a drop in their CCR7 levels. In case of anti-*ccr7*-2 and 3, it was almost reduced to isotype control levels, suggesting near complete knockouts (Fig. 2D). In 3D collagen gels DCs derived from anti-*ccr7* infections showed a significantly lower mean speed and entirely failed to migrate towards a CCL19 source (Fig. 2E, F, G and Supplementary movie 3) as would be expected for CCR7 knockouts that are unresponsive to CCL19.

Taken together, we demonstrate that knockouts can be easily and efficiently generated in Hoxb8-FL cells. These cells can be further differentiated to DCs that behave very similar to their BM derived counterparts. Recently, it has been observed that BM GM-CSF cultures, under certain culture conditions, comprise a heterogeneous population of macrophages and DCs, both expressing Cd11c and different levels of MHCII [16]. In our hands GM-CSF cultures from both BM and Hoxb8 origin, express homogenous levels of MHCII and CCR7 (which is not expressed by macrophages [16]) and thus show a homogenous and complete chemotactic response pattern. Genome editing efficiency was high in our hands, although for some gRNAs a certain small percentage of cells retained detectable protein. Residual expression can be easily circumvented by, as shown here, designing multiple gRNAs or by single cell cloning that will also facilitate thorough characterization of the genetic changes. The high efficiency of CRISPR/Cas9 mediated gene knockouts might also allow for infections of Hoxb8-FL cells with pooled gRNA libraries for specific subsets of genes, followed by functional screens. To gain complete control over the Hoxb8-FL genome we are currently establishing knock-in strategies to tag, replace and mutate endogenous genes. This is ideally done with non-integrating vectors, which is challenging due to the relative resistance of Hoxb8-FL cells to transient transfection. Notably, the potential of Hoxb8-FL cells to differentiate into other cell types of the myeloid and lymphoid lineage (e.g. Flt3 DCs, macrophages, B cells and T cells [11]) allows broader utilization of the targeted precursor cells.

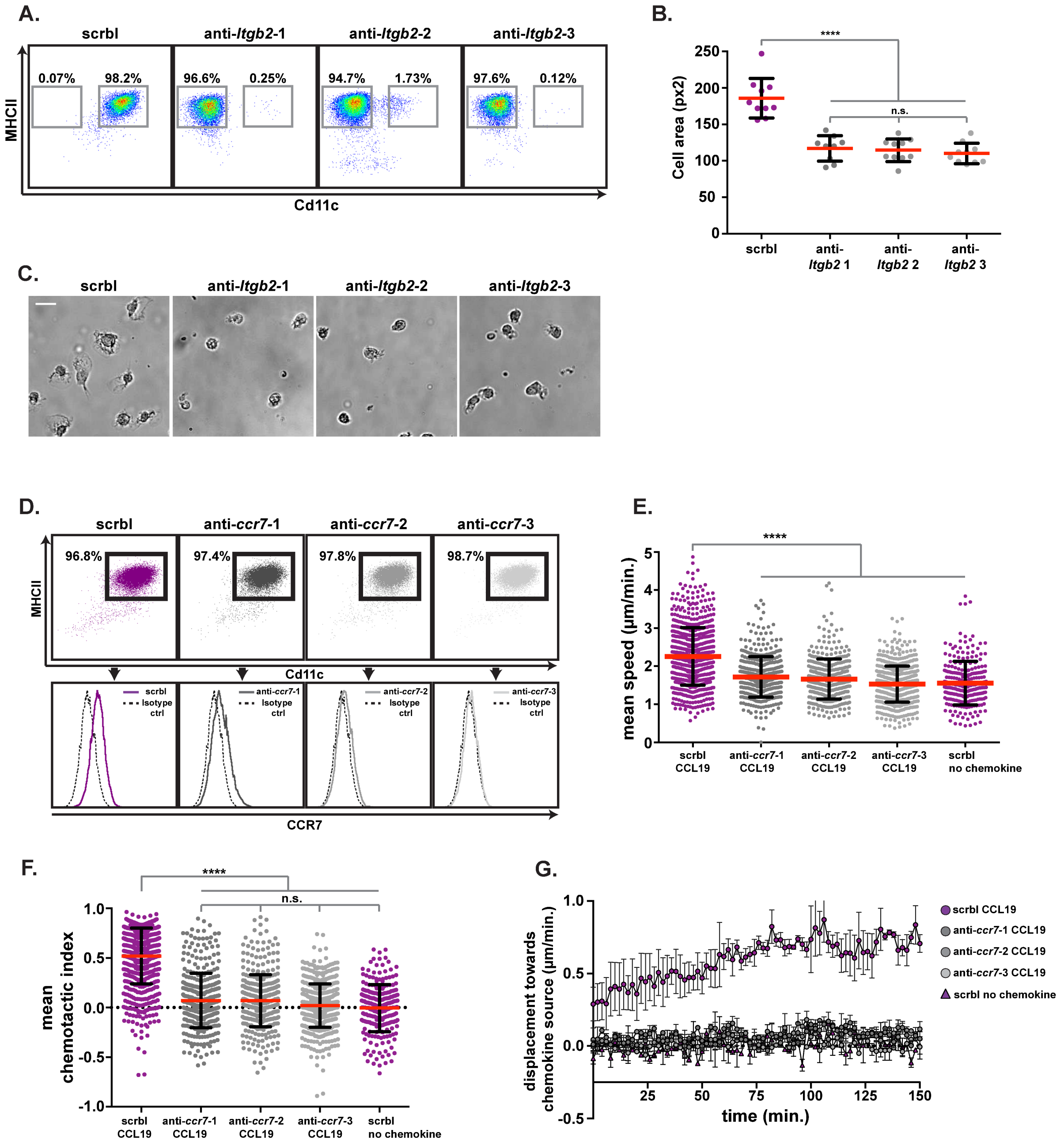

***Figure 7.* Characterization of Hoxb8-FL Itgb2 and ccr7 knockout DCs.** (**A**) FACS staining of putative Itgb2 knockout DCs for Cd11c and MHCII. (**B**) Cell area (pixel^2) of putative Itgb2 knockout DCs, plated on CCL21. Mean (red line) ± s.d. (black bars). ANOVA, **** P<0.0001. n=10 cells from each batch. (**C**) Snapshots of putative Itgb2 knockout DCs plated on CCL21. (**D**) FACS staining of putative ccr7 knockout DCs for Cd11c, MHCII and CCR7. CCR7 levels are pre-gated on Cd11c/MHCII high population (black boxes). (**E**) Mean single cell speeds (µm/min.) of putative ccr7 knockout DCs migrating in 3D collagen gels in CCL19 gradient. Mean (red line) ± s.d. (black bars). Kruskal-Wallis test, **** P<0.0001, n=755/421/406/574/256 (scrbl/anti-CCR7- 1/2/3/scrbl no chemokine), pooled from 3 biologically independent experiments. (**F**) Mean single cell chemotactic indices of cells in (**E**). Kruskal-Wallis test, **** P<0.0001. (**G**) Average y-displacement (µm/min.) over time (min.) of putative ccr7 knockout DCs in the presence (circles) or absence (triangles) of CCL19 gradient. Mean (dots/triangles) ± s.e.m. (black bars). n=3 collagen gels (CCL19) or n=2 collagen gels (scrbl, no chemokine), pooled from 3 biologically independent experiments.

4.5 Discussion

In this study we thoroughly characterized the migratory properties of Hoxb8-FL DCs by comparing them to BM DCs in *in vitro* and *in vivo* assays. Hoxb8-FL DCs show strong chemotaxis along CCL19 chemokine gradients with only a slightly reduced chemotactic index (a measure for the efficiency of migration in a chemokine gradient) compared to BM DCs. This is potentially attributable to slightly lower expression levels of chemokine receptor CCR7. In general, Hoxb8-FL cells migrate with slightly reduced speed in *in vitro* assays, which might indicate that components of the actomyosin polymerization and contraction machinery are differentially expressed in comparison to BM DCs. However, as we did not observe any differences in *in vivo* footpad injections the difference might also be rooted in the artificial environment of collagen gels, preventing Hoxb8-FL DCs from realizing their full migratory potential *in vitro*. In summary, Hoxb8-FL DCs show robust migratory behavior and chemotaxis and since the observed differences are small and not decisive, we think that Hoxb8-FL cells have the potential to largely replace BM derived DCs as a model system.

Furthermore, we show that knockout efficiency in Hoxb8-FL cells via lentivirally delivered CRISPR/Cas9 is extremely high. It is noteworthy that we never observed any indication for single allele knockouts. Instead, of all genes tested both alleles seem to be affected, leading to knockout efficiencies of almost 100%. While this high efficiency is in principle desirable it might arise from the fact that in our system the CRISPR/Cas9 system is permanently integrated into the cells genome. Consequently, it is permanently active and will eventually introduce double-strand breaks at all desired- but potentially also other loci, leading to off-target effects. In our system we designed multiple guide RNAs to control for this effect. We found that all gRNAs for the same gene result in the same phenotype and could not find any obvious evidence for off-target effects that would result in differentiation-, maturation-, or migration defects in DCs. However, as we only used cells of early passages, off-target effects might accumulate and occur over time in later passages. Therefore, future improvements of our system should aim to replace Cas9 with engineered variants with a higher specificity [47]. Alternatively, the CRISPR/Cas9 system might be only expressed transiently from plasmids, which turns out to be challenging as conventional DNA delivery methods show only poor efficiency in Hoxb8-FL cells (personal observation). Additionally, transient expression of the CRISPR/Cas9 system would mean that, in contrast to lentiviral infection, no selection marker is available to enrich for potential knockout cells, making single-cell cloning a necessity. However, the delivery of DNA that serves as template for HDR is a prerequisite for the generation of knock-ins to precisely mutate or tag endogenous genes in Hoxb8-FL cells. In the latter case, the achieved DNA delivery efficiencies of ~1% (personal observation) might be even sufficient as knock-in cells, tagged with fluorescent reporters could be easily isolated and propagated. Nevertheless, current efforts aim to improve DNA delivery to gain full control over the genome of Hoxb8-FL cells.

In summary, we show that (1) gene knockouts can be efficiently introduced in Hoxb8-FL cells via lentiviral delivery of the CRISPR/Cas9 system and (2) that these cells retain their ability to differentiate into migratory DCs, very similar to BM derived DCs. The here-described system is a powerful tool for the study of DC biology but also for the study of other immune cells as Hoxb8-FL cells have the potential to differentiate into other cell types of the myeloid and lymphoid lineage.

4.6 Material and methods

Animals

Mice were bred and maintained at the local animal facility in accordance with the IST Austria ethics commission. All experiments were conducted in accordance with the Austrian law for animal experiments. Permission was granted by the Austrian federal ministry of science, research and economy (identification code: BMWF-66.018/0005-II/3b/2012).

Cell culture

R10 medium, consisting of RPMI 1640, supplemented with 10% Fetal Calf Serum (FCS), 2mM L-Glutamin, 100U/ml Penicillin, 100µg/ml Streptomycin and 50µM 2-Mercaptoethanol (all Thermofisher), was used as basic medium for all cells. Hoxb8-FL precursor cells were grown in 'Hoxb8 media', consisting of R10, 5% supernatant of an Flt3L producing cell line and 1µM estrogen (Sigma, E-2758). All cells were grown and maintained at 37°C/ 5% CO_2.

Retroviral immortalization of hematopoietic precursors

Immortalization was carried out as described previously [12]. In brief, estrogen controlled Hoxb8 encoding, retrovirus was produced in 293T cells according to standard procedures. Bone marrow (BM) was isolated from femur and tibia of a female, 6-week-old C57BL/6J wild type mouse. Cells were pipetted on a Ficoll gradient to remove red blood cells and mature granulocytes. Cells from the supernatant were stimulated to enter the cell cycle by incubating them for 2-3 days in 'stem cell media', consisting of 10ng/ml IL-3 (Peprotech, 213-13), 20ng/ml IL-6 (Thermofisher, 14-8061-62) and 1% supernatant of a stem cell factor (scf) producing B16 melanoma cell line. $3x10^5$ cells were then seeded in 1ml of Hoxb8 media in a 12-well plate. 500µl of retrovirus, together with 1.5µl Lipofectamin (Thermofisher, 18324012) were added and the plate was spun with 1000g for 1h at room temperature. Cells were then maintained in Hoxb8 medium for the next three to fours weeks with regular changes of the medium. After this period of time, the only cells left will be the immortalized hematopoietic precursors that exhibit a round, blast-like appearance and that can be maintained according to standard cell culture procedures.

Generation of mG Hoxb8-FL cells

Hematopoietic precursors of a 6 week old, female C57BL/6J Gt(ROSA)26Sor$^{tm4(ACTB-tdTomato,-EGFP)Luo}$IJ (mTmG, Jackson) mouse were immortalized as described above. Cells were infected with a lentivirus coding for Cre recombinase as described below. The Cre expression plasmid was obtained by cloning iCre (a gift from Rolf Zeller, addgene #26745) into the pLenti6.3 vector (Thermofisher). Cells that changed their fluorescence from red to green were sorted on a FACS Aria III (BD) and used for further experiments.

gRNA design and cloning into LentiCRISPR vector

Anti-GFP gRNAs were described previously [14]. All other gRNAs were designed using the 'Benchling' (https://benchling.com) CRISPR gRNA design tool. gRNAs that bind to early exons and that had good on-/off target predictions were chosen (for sequences see Supplementary Table 1) Oligonucleotides were ordered in HPLC grade and cloned into the LentiCRISPRv1 (a gift from Feng Zhang, addgene #49535) or LentiCRISPRv2 blast (a gift from Brett Stringer, addgene #98293) plasmids as described previously [14]. Plasmids were partially sequenced (U6 primer: 5' GAGGGCCTATTTCCCATGATTCC 3') to confirm correct ligation of the gRNA sequence.

Lentivirus production

LX-293T cells (clontech) were grown in DMEM, high glucose, GlutaMAX, supplied with 10% FCS, 100U/ml penicillin and 100µg/ml streptomycin (all Thermofisher). One day before virus production, cells were seeded into 100mm cell culture dishes (VWR, 734-2321) to obtain a confluence of ~80% on the next day. For virus production, DMEM was taken off and cells were briefly washed with PBS before 5ml serum-free Opti-MEM (Thermofisher) medium was added. To 1ml Opti-MEM, 30µl Lipofectamin 2000 (Thermofisher, 11668027), 5.4µg LentiCRISPR plasmid, 4µg pCMV dR8.2 dvpr packaging plasmid and 2.7µg pCMV-VSV-G envelope plasmid (kind gifts from Bob Weinberg, addgene #8455 and #8454) were added. The mixture was incubated for 20min. at room temperature before it was added drop-wise to the cells. After 4-5h, the medium was changed back to fully supplemented DMEM. On the next day, medium was replaced with fresh DMEM. 48h later, virus in the supernatant was collected, filtered through a 0.45µm syringe filter and then either snap frozen with liquid nitrogen and stored at -80°C or directly used for the infection of Hoxb8-FL cells.

Infection and antibiotic selection of Hoxb8-FL cells

Per infection, $3x10^5$ Hoxb8-FL cells, in 1ml of Hoxb8 media, were seeded in a 12-well plate. 500µl virus and 6µg/ml polybren (Sigma, 107689) were added and the plate was sealed with parafilm. Cells were spun with 1500g for 1h at room temperature. After spinning, 1ml of medium was taken off and 2ml of fresh Hoxb8 media were added. On the next day, 2ml of media were taken off and again replaced with fresh media. Cells were then expanded for one week and transferred to bigger volumes if necessary. For antibiotic selection, 1x10^6 infected Hoxb8-FL cells were transferred to a 6-well plate in 3ml of Hoxb8 media, containing either 4µg/ml puromycin or 10µg/ml blasticidin (both Thermofisher, A1113803 or A1113903). Cells were kept under selection for one week at which point, dividing cells should be clearly visible. Surviving cells were kept in fresh, antibiotic-free Hoxb8 media for expansion and/or differentiation to DCs.

Differentiation of DCs from BM or Hoxb8-FL cells

Cells were grown in 94mm petri dishes (Greiner, 632180) to allow loosely adherent cells to stay in suspension. Per dish, 2x10^6 BM cells from 6-12 week old male or female C57BL/6J wild type mice or 2.5x10^5 Hoxb8-FL cells were seeded in 9ml R10, supplied with 1ml in house generated granulocyte-macrophage colony stimulating factor (GM-CSF) hybridoma supernatant. Before, Hoxb8-FL cells were washed twice with PBS to remove estrogen. On day 3 of the cultures, 8 ml R10, supplied with 2ml GM-CSF, were added. Half of the medium was replaced on day 6. On day 8, non-adherent cells were collected from the supernatant of two dishes and stimulated over night in 150mm cell culture dishes (VWR, 734-2322) in 18ml R10, supplied with 2ml GM-CSF and 200ng/ml lipopolysaccharide (LPS) from *E.coli* 0127:B8 (Sigma, L4516). Cells from the supernatant were used for experiments.

FACS stainings

Following antibodies (all ebioscience) were used in the indicated dilutions: anti-mouse Cd11c-APC (1/300; N418), anti-mouse MHCII-eFluor450 (1/800; M5/114.15.2), anti-mouse CCR7-PE (1/300, 4B12). Stainings were carried out in FACS Buffer (1x PBS, 2mM EDTA, 1% BSA). Prior to staining, Fc receptors were blocked (using anti-mouse CD16/CD32, 1/100, 93) to prevent unspecific antibody binding. All incubation steps were carried out for 15min. at 4°C, except CCR7-PE, which was incubated for 30min. at 37°C. All samples were kept on ice until data acquisition on a FACS Canto II (BD).

Collagen migration assays

Chemotaxis assays were performed as described previously [13]. PureCol bovine collagen, (INAMED) in 1x minimum essential medium eagle (MEM, Sigma) and 0.4% sodium bicarbonate (Sigma) was mixed with 2x10^5 DCs in R10 at a 2:1 ratio, resulting in gels with a collagen concentration of 1.6 mg/ml. Collagen-cell mixtures were cast in custom-made migration chambers. After 60min. of polymerization of collagen fibres at 37°C/5% CO_2, gels were either overlaid with CCL19 in R10 (PeproTech, 250-27B, 0.625µg/ml) or R10 alone. Chambers were sealed with paraffin and time-lapse video microscopy was started immediately with a 10x objective and a frame interval of 2min. at a setup that allows parallel imaging of 6 collagen gels at 37°C/5% CO_2. Tracking was performed using the Fiji plugin

Trackmate [50]. To this end, the mean z-projection of the whole image sequence was subtracted from each frame to remove background. The gray values of the sequence were then inverted and Trackmate was started with the following settings: blob diameter: 20µm, initial thresholding: auto, linking max. distance: 15µm, gap-closing max. frame gap: 1, filter on tracks: duration, auto. A custom-made matlab script (available under https://datarep.app.ist.ac.at/75/) was used to derive chemotactic indices from single cell tracks. The Fiji script to determine average displacement of cells towards the chemokine source has been described previously [51].

CCL21 adhesion assay

Per condition, a small drop (~3µl) of 10µg/ml CCL21 (PeproTech, 250-13) was pipetted on a clean petri dish and left for air-drying. The region was marked with a pen and dishes were washed two times with PBS. 1×10^5 DCs in R10 were introduced and imaging was started immediately. Single images from time-point 15min. were used to determine the area of single cells in pixels^2.

Mouse footpad injections

BM and Hoxb8 DCs were labeled with 10 µM TAMRA or 3 µM Oregon Green 488 (Thermofisher, C1171 and C34555) respectively, and vice versa. A total number of 0.5×10^6 cells in 25µl PBS was injected subcutaneously into hind footpads of 6-8 week old, male or female wt C57BL/6J mice. After 24h mice were sacrificed and the popliteal lymph nodes were collected. Lymph nodes were torn open with needles and incubated in digestion buffer (0.5mg/ml Collagenase D, 40µg/ml DNAseI and 3mM $CaCl_2$ in R10) for 30min. at 37°C. The reaction was stopped by the addition of EDTA to a concentration of 10mM. Fc receptors were blocked and cells were stained for Cd11c and MHCII as described before. Flowcytometry was carried out on a FACS Aria III machine. The ratio of cells was calculated as the absolute number of Hoxb8 DCs divided by the absolute number of BM DCs. Oppositely labeled BM DCs were used as a control to exclude effects of the dyes on migration.

5 The dendritic cell branched F-actin cytoskeleton in immunological synapse formation

The Immunological synapse (IS) is a specialized cell-cell contact that serves as a temporal communication platform between T cells and antigen presenting cells (APCs), but also other types of immune cells [52]. Kupfer and colleagues first coined the term in the 90s of the 20th century, describing highly structured clustering of certain molecules and components of the cytoskeleton in contacts between T- and B cells [53]. Research in the following years provided us with a detailed picture of the processes on the T cell side of the IS. This was made possible by the observation that APCs seemingly play no active role in the formation of the synapse [54] and thus can be replaced by artificial lipid bilayers (ALBs), containing interaction partners for molecules on the T cell surface. This enabled imaging of IS formation in T cells in one plane with very high time resolution, using total internal reflection microscopy (TIRF) [55]. Importantly, it was shown that a dynamic F-actin cytoskeleton in T cells is indispensible for T cell activation. However, it has become clear that in the all-important IS between T cells and DCs, also an intact DC F-actin cytoskeleton is decisive for T cell priming [56]. Consequently, a growing number of studies, including this one, is trying to decipher the role of DC F-actin and its regulatory factors at the IS.

The following chapters will give an overview of IS formation in T cells and summarize current knowledge of T cell – DC synapses *in vitro* and *in vivo.*

5.1 The T cell immunological synapse

The prototypical IS that forms when T cells interact with peptide MHC (pMHC) bearing artificial lipid bilayers or B cells, exhibits a highly organized symmetric structure. It is organized into three concentric rings, each containing a characteristic set of molecules or cytoskeletal components. These are: the central supramolecular activation cluster (cSMAC), the peripheral SMAC (pSMAC) and the distal SMAC (dSMAC). The cSMAC harbors the transmembrane receptors T cell receptor (TCR) complex and depending on the T cell subtype cluster of differentiation (CD) 4 or 8, lymphocyte-specific protein tyrosine kinase (Lck), Zeta-chain-associated protein kinase 70 (ZAP-70) and Phospholipase C, γ1 (PLCγ1). While the cSMAC is largely devoid of F-actin, the pSMAC contains high amounts of F-actin, the integrin Lymphocyte function-associated antigen 1 (LFA-1) and talin, which links integrins to the actin cytoskeleton. The outermost ring, the dSMAC contains CD43, the protein tyrosine phosphatase CD45 and F-actin.

The here-described configuration is readily visible in confocal microscopy of fixed samples. However, in reality the IS is a highly active structure that intimately links the dynamics of its components with TCR signaling. Therefore, TCR signaling will be discussed first, followed by a description of the dynamics at the IS.

5.1.1 T cell receptor signaling

The majority of TCRs in an organism is composed of variable α and β chains, created by somatic mutation during T cell development. Together with the heterodimers CD3ε/δ, CD3γ/ε and the homodimer CD3ζ/ζ they form the octameric TCR complex, which has no catalytic activity by itself. Instead the CD3 subunits exhibit short cytoplasmic tails that contain immunoreceptor tyrosine-based activation motifs (ITAMs). Additionally, the TCR complex is directly connected to the F-actin cytoskeleton via CD3ζ [57]. Upon TCR-pMHC interaction, CD3 ITAMs are phosphorylated by lymphocyte-specific protein tyrosine kinase (Lck), which triggers a chain of downstream phosphorylation events [58]. However, the initial events leading to TCR triggering are currently not fully understood and several non-mutually exclusive models exist [59].

The *kinetic segregation model is* based on the interaction of Lck by CD45. In the ground state, CD45 and Lck frequently co-localize, which inhibits activity of the latter by phosphorylation. Upon TCR-pMHC interaction, through the short ectodomains of both molecules (7nm), close membrane appositions are created. This process is potentially supported by F-actin polymerization that creates protrusions to form regions of close membrane contact. This excludes molecules with very long ectodomains, such as CD45, from the contact site. Consequently, Lck is no longer inhibited and is free to phosphorylate ITAMs on CD3.

In the *kinetic proofreading model* a certain threshold of TCR-pMHC bond lifetime has to be reached to trigger TCR signaling. This threshold can be either achieved by a single, long TCR-pMHC interaction or by several short interactions within a certain time span. Again, force of the F-actin cytoskeleton might play a role in this model as it has been observed that bond lifetime increases when force is applied to the TCR.

The *serial triggering / serial encounter model* takes into account the possibility that a high number of specific TCRs on a single T cell are potentially opposed by a very low number of fitting pMHC molecules. Consequently, a few pMHC molecules have to make consecutive, short-lived interactions with a high number of TCRs. Here, the F-actin cytoskeleton might cluster many TCRs together so they can interact with a single pMHC molecule.

Finally, the *conformational change model* proposes that upon antigen recognition the conformation of the TCR changes and ITAMs get exposed for phosphorylation. Again, F-actin might provide the force that is necessary to change the conformation of the TCR and initiate signaling.

As a consequence of ITAM phosphorylation Zap70 is recruited, which in turn activates the adaptor proteins linker for activation of T cells (LAT) and SH2 domain–containing leukocyte phospho-protein of 76 kDa (SLP-76), forming the backbone of the proximal signaling complex (PSC). Formation of the PSC leads to activation of PLCγ1 that produces the second-messengers inositol trisphosphate (IP_3) and diglyceride (DAG). IP_3 leads to influx of Ca^{2+} from the endoplasmic reticulum (ER) and the extracellular space. This triggers a variety of transcription factors (TFs) e.g. nuclear factor of activated T cells (NFAT) that translocates from the cytoplasm to the nucleus and initiates a variety of transcriptional programs. DAG activates Ras and PKCθ that in turn lead to activation of several TFs downstream of the mitogen-activated protein kinase (MAPK)- and the nuclear factor kappa-light-chain-enhancer of activated B cells (NF-κB) signaling pathway respectively. The convergence of these signaling pathways and transcriptional programs eventually leads to full T cell activation, cytokine production and T cell proliferation [58]. Assembly of the PSC also leads to recruitment of the adaptor protein Non-catalytic region of tyrosine kinase adaptor protein 1 (Nck1) and the GEF Vav guanine nucleotide exchange factor 1 (Vav1). Nck1 recruits WASP while the latter activates Cdc42 and Rac1, leading to WASP/WAVE/Arp2/3 dependent F-actin polymerization at the IS [59].

Signaling from several other molecules, such as LFA-1 and the co-stimulatory molecule CD28, also feeds into T cell activation pathways and F-actin polymerization. LFA-1 is initially activated by signaling downstream of the TCR, termed inside-out signaling. Activated SLP-76 recruits the adaptor molecule adhesion- and degranulation-promoting adaptor protein (ADAP) that in turn, via several other molecules, leads to activation and membrane recruitment of the small GTPase Rap1. Rap1 leads to binding of talin to LFA-1, which brings it from its bended- into its extended state and associates it with the F-actin cytoskeleton [58]. In the extended form, LFA-1 can bind to its ligand intercellular adhesion molecule 1 (ICAM1), which brings it into its signaling competent, high affinity state. This triggers a signaling pathway, termed outside-in signaling, that feeds into the MAPK signaling pathway, thereby contributing to T cell activation. Additionally, LFA-1 also contributes to F-actin polymerization via the SLP-76/ADAP/Vav1 axis [59].

The co-stimulatory molecule CD28, upon binding its ligands CD80 or CD86 on the surface of APCs, initiates a signaling cascade that feeds into the NF-κB and NFAT TF mediated signaling pathways [58]. Additionally, it contributes to SLP-76/Vav1 mediated actin polymerization and is also more directly connected to the F-actin cytoskeleton via Filamin A [59].

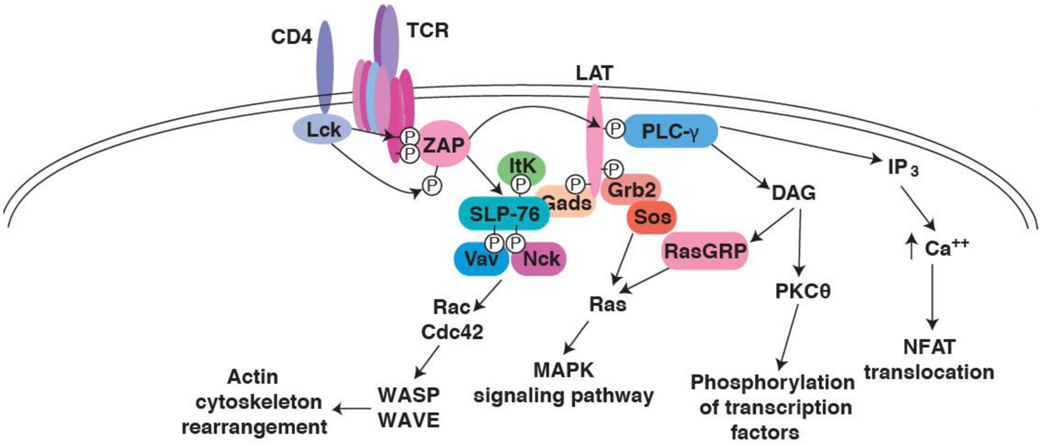

Figure 8. **The induction of T cell receptor signaling.** Upon antigen recognition, TCR ITAM phosphorylation, via ZAP70 and LAT, leads to SLP-76 activation that forms the backbone of the proximal signaling complex (PSC). PSC formation leads to PLC-γ activation and production of DAG and IP_3, which activates a variety of transcription factors and signaling pathways. Rac and Cdc42 are triggered through SLP-76 mediated Vav and Nck activation, leading to WASP and WAVE mediated rearrangement of the actin cytoskeleton. Modified after Love and Hayes, 2010.

5.1.2 Dynamics of the prototypical immunological synapse

The prototypical IS of T cells is a highly dynamic structure. Upon antigen recognition, T cells spread and start to polymerize F-actin in two distinct structures. The first one is a ring-like F-actin network in the dSMAC. This undergoes centripetal movement through the pSMAC towards the cSMAC, which by itself is devoid of F-actin. Myosin appears in the pSMAC and contracts the F-actin cytoskeleton in overlapping regions [60],[61]. TCRs, together with adaptor molecules and kinases such as Zap70 and LAT, appear as discrete clusters in the periphery of the synapse, termed microclusters (TCR-MC) [62]. In resting T cells some components of TCR-MCs are pre-clustered in segregated units and are assembled upon antigen recognition in an F-actin dependent process [63],[64]. Some of the assembled TCR-MCs co-localize with WASP dependent actin foci, which is the second F-actin structure that is formed. Additionally, these actin-TCR foci have been found to co-localize with activated PLCγ1. Specific interference with WASP mediated actin polymerization abrogates Ca^{2+} signaling while initial TCR signaling events are unaffected, showing that the two F-actin structures have distinct roles in T cell activation [65]. Furthermore, each TCR-MC is transiently bordered by a micro-adhesion ring in the initial phase of IS formation, consisting of LFA-1, focal adhesion proteins, F-actin and myosin. This structure seems to support SLP-76 activation via LFA-1 outside-in signaling, which appears to be especially important under low antigen concentrations, potentially to overcome a threshold for TCR signaling [66]. TCR-MCs are then transported from the periphery to the center of the synapse. This movement is coupled to- and critically dependent on the centripetal flow of ring-like F-actin. Consequently, disruption of the F-actin cytoskeleton stops TCR-MC translocation and abrogates TCR signaling [67]. TCR signaling itself takes place in TCR-MCs while they travel

from the periphery towards the cSMAC. At the pSMAC/cSMAC border adaptor molecules and kinases decouple from the TCR [62]. The latter is then loaded on dynein and the microtubule cytoskeleton for transport to the center of the cSMAC as it contains no F-actin [68]. The cSMAC is now mainly seen as a compartment for 'old' TCRs that are either recycled via endocytosis or released via exocytosis [69].
Recently, the localization of the TCR has been linked to the 3D structure of T cells. T cells exhibit numerous microvilli and their tips are highly enriched in TCR. Furthermore, these microvilli are highly dynamic and it seems plausible that they serve a search strategy for pMHC [70],[71]. However, it remains to be elucidated in which context these findings stand to the above-described organization and dynamics of the prototypical T cell IS.

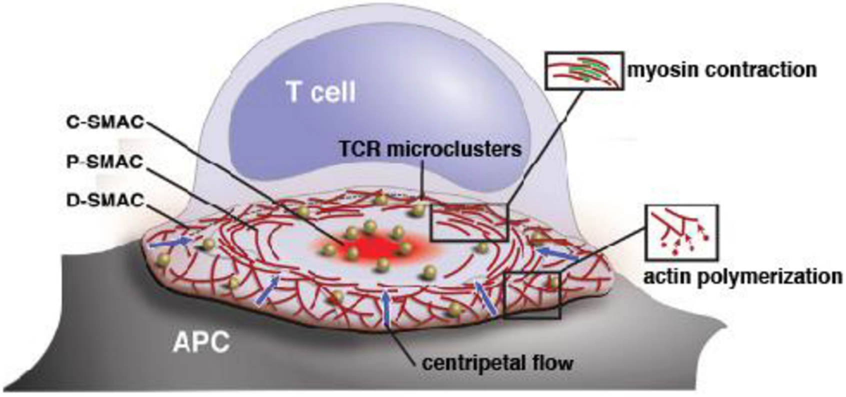

Figure 9. **The prototypical immunological synapse.** The prototypical immunological synapse of T cells is segregated into three distinct domains: the c-, p- and dSMAC. Actin polymerization in the dSMAC leads to centripetal flow that is supported by myosin contraction in the pSMAC. The centripetal flow transports signaling TCR microclusters, which are born in the dSMAC, to the cSMAC that is devoid of actin. Signaling ceases in the cSMAC where TCRs are recycled or exocytosed. Modified after Comrie and Burkhardt, 2016.

5.2 The dendritic cell – T cell immunological synapse

The T cell side of the IS, has been studied in great detail, mainly in the context of ALBs. However, little is known about the molecular dynamics at the DC-T cell IS and it is unclear if above described processes also govern DC-T cell synapses. In contrast, with the advent of multi-photon intravital microscopy (MP-IVM), DC-T cell contacts have been relatively well described *in vivo* although no unified picture has emerged [72]. The following sections will first give an overview over DC-T cell interactions *in vivo* and then summarize our current knowledge of the structure, molecular dynamics and the role of the DC F-actin cytoskeleton at the DC-T cell synapse.

5.2.1 DC – T cell interactions *in vivo*

The first insights into the dynamics of DC-T cell contacts came from an imaging study in collagen gels. There, DCs and T cells make only short contacts of a few minutes. Nevertheless, these transient contacts lead to full T cell activation and proliferation, challenging the view that a stable IS has to be formed to support T cell priming [73]. Following MP-IVM studies in live animals or explanted lymph nodes gave no clear picture of DC-T cell contacts *in vivo* [74]. Instead, two predominant scenarios emerged. In the first one, DC-T cell contacts occur in three different phases. In the first phase, lasting a few hours, DC-T cell contacts are transient and last a few minutes and are accompanied by up-regulation of T cell activation markers. In the second phase, contacts become stable over several hours and T cells start to produce cytokines. In the last phase, contacts become transient again and T cells start to proliferate [75].

In the second scenario, the first DC-T cell encounter immediately leads to stable contact formation that lasts several hours. Contact disruption by antibodies leads to insufficient T cell priming [76]. Given the diversity of observations, it seems plausible that the nature of DC-T cell contacts *in vivo* depends on the precise experimental conditions such as the T cell subset (CD4 or CD8), antigen species and affinity or DC maturation state [72]. However, the existence of short- but productive contacts between DC and T cells in many experimental systems points to a highly dynamic nature of the DC-T cell IS.

5.2.2 Ultrastructure, molecular composition and the role of DC F-actin at the immunological synapse

The membranes at the IS between T cells and ALBs are expected to be flat with very tight appositions at the center of the synapse due to short ectodomains of molecules occurring in the cSMAC. This configuration has been termed *monofocal* IS. In contrast, the IS between DCs and T cells has been shown to be *multifocal*, with multiple regions of tight membrane apposition [77]. Consequently, a Kupfer-type synapse is not formed and molecules that have been shown to be confined to c- or pSMAC, such as the TCR and LFA-1, might co-localize at the DC-T cell IS [77]. This configuration is potentially mediated by the formation of numerous microvilli on both DCs and T cells [78], which is supported by the recent finding that the TCR localizes to dynamic microvilli on T cells [71],[79].

As mentioned earlier, the DC F-actin cytoskeleton is decisive for T cell priming [56]. DCs actively polarize F-actin and fascin towards the IS in an antigen dependent manner and pharmacological interference with F-actin polymerization leads to impairment in T cell priming [80]. DCs initiate T cell contacts by their dynamic protrusions, upon which more protrusions are formed in the direction of the T cell, which is eventually enwrapped by the DC. These protrusions are created by polymerization of branched F-actin and removal of these structures by Rac1/2 knock-out leads to severe defects in DC-T cell contact formation and T cell priming [81].

After contact formation, the DCs microtubule organizing center (MTOC), together with numerous IL-12 containing, vesicle-associated membrane protein 7 (VAMP7) decorated, vesicles trans-locates to the IS in a Cdc42 dependent process [82]. IL-12 is then specifically secreted at the synapse where it is important for the acquisition of T cell effector functions [83].

Farther downstream in the actin polymerization pathway, DC WASP and formin mDia1 have been implicated in IS formation. MDia1 deficient DCs fail to establish long-lasting contacts with T cells, accompanied by T cell proliferation defects *in vivo* and *in vitro*. However, it is unknown if absence of DC mDia1 leads to changes in the molecular organization of the IS [84].

DC WASP has been shown to be critical for the formation of stable DC-T cell contacts and in its absence T cell signaling and proliferation are compromised [85],[86]. This defect has been characterized in more detail, showing that WASP deficient DCs form smaller contacts with T cells accompanied by reduced ICAM1 polarization to the IS and that their F-actin at the IS is less stable. Furthermore, in an ALB system containing antibodies against MHCII and ICAM1 it has been shown that DCs form a central cluster of MHCII surrounded by a ring of ICAM1 that mirrors the prototypical T cell synapse. WASP deficient DCs fail to induce this type of organization, coinciding with a deficiency to form actin rich podosomes at the IS, which might explain their defect in forming stable contacts with T cells [87].

One component underlying some of the above-described defects seems to be the ability of DCs to immobilize and cluster ICAM1 with their F-actin cytoskeleton via talin and α-actinin. Immobilized ICAM1 is ideally suited for stable binding- and conversion of T cell LFA-1 into its high affinity state where it supports signaling and T cell activation. Consequently, impairment of DC F-actin leads to reduced ICAM1 immobilization, clustering and T cell priming [88].

Interestingly, it recently has been shown that excessive stability of DC-T cell contacts also leads to defects in T cell priming. Regulatory T cells have a reduced ability to release ICAM1 bound LFA-1 from their talin mediated F-actin association. Thereby, a strongly adhesive contact is formed that sequesters fascin and F-actin from other regions of the DC and thus prevents it from interacting with other naïve T cells [89].

5.3 Aims and initial status

As laid out before it has become clear that a *dynamic* DC F-actin cytoskeleton is decisive for T cell priming. However, it remains to be elucidated how exactly these dynamics looks like, which F-actin structures are formed and how they support T cell activation. Along these lines, it is unclear if all F-actin at the DC synapse is equally important or if there are different classes, potentially polymerized by different nucleation factors, with distinct roles similar to the situation in T cells [65].

Imaging of the T cell-APC immunological synapses is not trivial as it is very dynamic and requires recording of several stacks, lacking resolution in time and z-dimension, which is one reason why the vast majority of studies replaced APCs by ALBs. Therefore, we decided to develop a new imaging setup for live imaging of the DC-T cell synapse in a single imaging plane. This setup would allow us to study rapid molecular dynamics at the IS. To identify potential F-actin subclasses at the IS we decided to follow a knockout approach. To this end we employed WAVE deficient DCs, which showed severe T cell priming defects in preliminary studies and the previously characterized WASP deficient DCs.

5.4 Results

As laid out in the previous sections the DC F-actin cytoskeleton has been shown to be decisive for T cell priming. However, the study that is typically cited in this context used Cytochalasin D to inhibit actin polymerization in DCs [56], which can be washed out from cells. Thus the observed effect on T cell priming could be partially caused by unwanted effects on actin assembly in T cells. Therefore, we decided to recapitulate these experiments by using DCs we pre-treated with mycalolide B (mycB), which irreversibly de-polymerizes F-actin by covalent sequestration of G-actin monomers [90]. Actin de-polymerization had no effect on Cd11c and MHCII surface levels, several hours after drug treatment. Importantly, there was also no detectable effect on cell survival (Fig. 10A). In CFSE dilution assays, mycB treated DCs had a strong disadvantage in priming naïve T cells, which was also apparent at very high peptide concentrations (Fig.10B). Thus, our data confirm earlier results and further strengthen the view that the DC actin cytoskeleton is decisive for T cell priming.

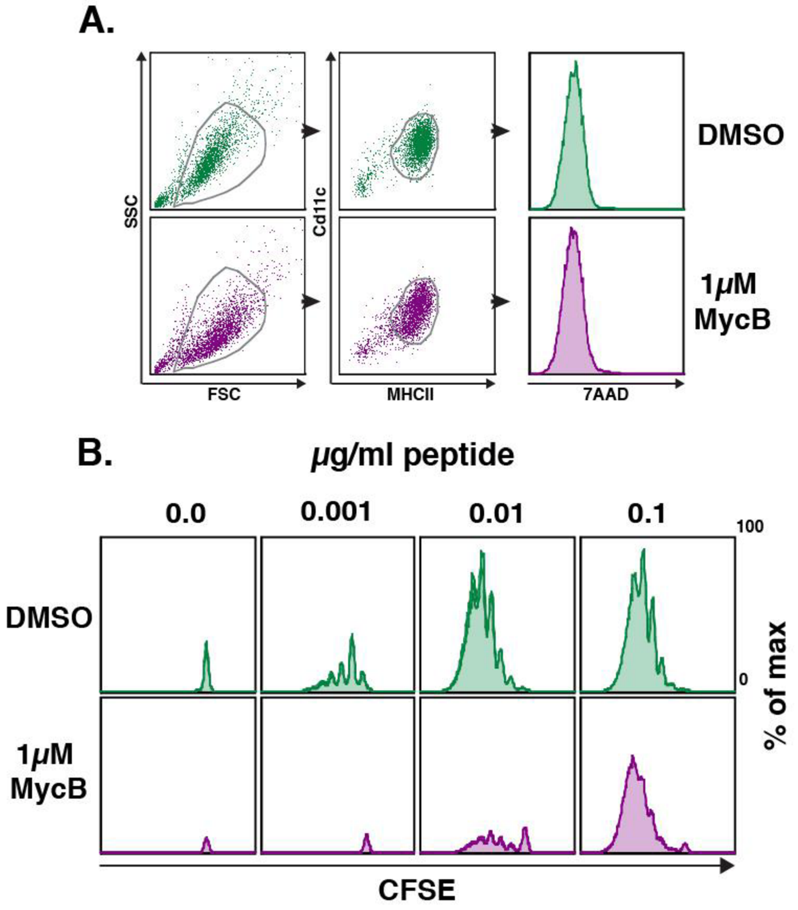

Figure 10. **The effect of actin de-polymerization in DCs on T cell priming.** (**A**) FACS stainings for Cd11c, MHCII and 7AAD life/dead stain in mDCs, 4h after treatment with 1μM MycB or DMSO. (**B**) FACS analysis of CFSE dilution-T cell proliferation assays under varying OVA peptide concentrations, 96h after start of OT-II TCR CD4+, CFSE stained T cell and DC co-culture. DCs were pre-treated with 1μM MycB or DMSO control.

Next, we wanted to image synaptic DC F-actin in high spatial resolution. To this end, we generated narrow chambers of 3-4µm height by confining OVA peptide loaded, Lifeact-eGFP expressing DCs together with TCR transgenic T cells between glass slides and polydimethylsiloxane (PDMS) pillars of a defined height. In this setup, DCs and T cells frequently form immunological synapses in the horizontal plane, making them ideal for imaging by confocal microscopy (Fig.11A). In z-reconstructions, DC F-actin uniformly accumulated at the contact site. However, imaging directly at the contact plane revealed that DC F-actin accumulates in discrete, dot-like foci at the IS (Fig.11B). To exclude that F-actin accumulations are caused by membrane undulations we used DCs derived from Lifeact-eGFP/membrane-targeted Tomato double transgenic mice. Whereas Lifeact-eGFP was strongly enriched at the IS there was no apparent membrane accumulation at the IS (Fig.11C). Thus we conclude that F-actin accumulations are caused by *de-novo* polymerization and not by large-scale membrane rearrangements within the resolution of confocal microscopy. To confirm the existence of F-actin foci at the IS, independently of the Lifeact-eGFP probe we injected DCs and T cells between glass slides and a layer of agarose where similar types of contacts are formed. Staining with phalloidin, followed by superresolution microscopy confirmed the existence of F-actin foci at the IS between DCs and T cells (Fig.11D).

Before we set out to describe the dynamics of DC F-actin at the IS in a wt and knock-out context, we first decided to thoroughly characterize T cell priming defects of hem1-/- DCs. Absence of WAVE in DCs leads to strong impairment in T cell priming, resulting in strongly reduced T cell numbers under all peptide concentrations, 96h after the assay was started (Fig.12A). To determine which stage of T cell priming is affected, we simultaneously stained for the naïve T cell marker CD62L and the early activation marker CD69 at different time-points of DC-T cell interactions. After only two hours, the first time-point assessed, a markedly reduced number of T cells appeared in the CD69^{high} CD62L^{low} gate when they were primed by hem1-/- DCs. This defect was visible at all time-points, culminating at 16h and occurring under all peptide concentrations (Fig.12B and C). Additionally, there was a strong reduction of IL-2 levels in the supernatants of hem1-/- DC-T cell co-cultures (Fig.12D). Taken together, our data show that absence of WAVE in DCs leads to immediate and early T cell priming defects, resulting in a lower number of activated T cells and reduced IL-2 levels that are suboptimal to support full T cell expansion.

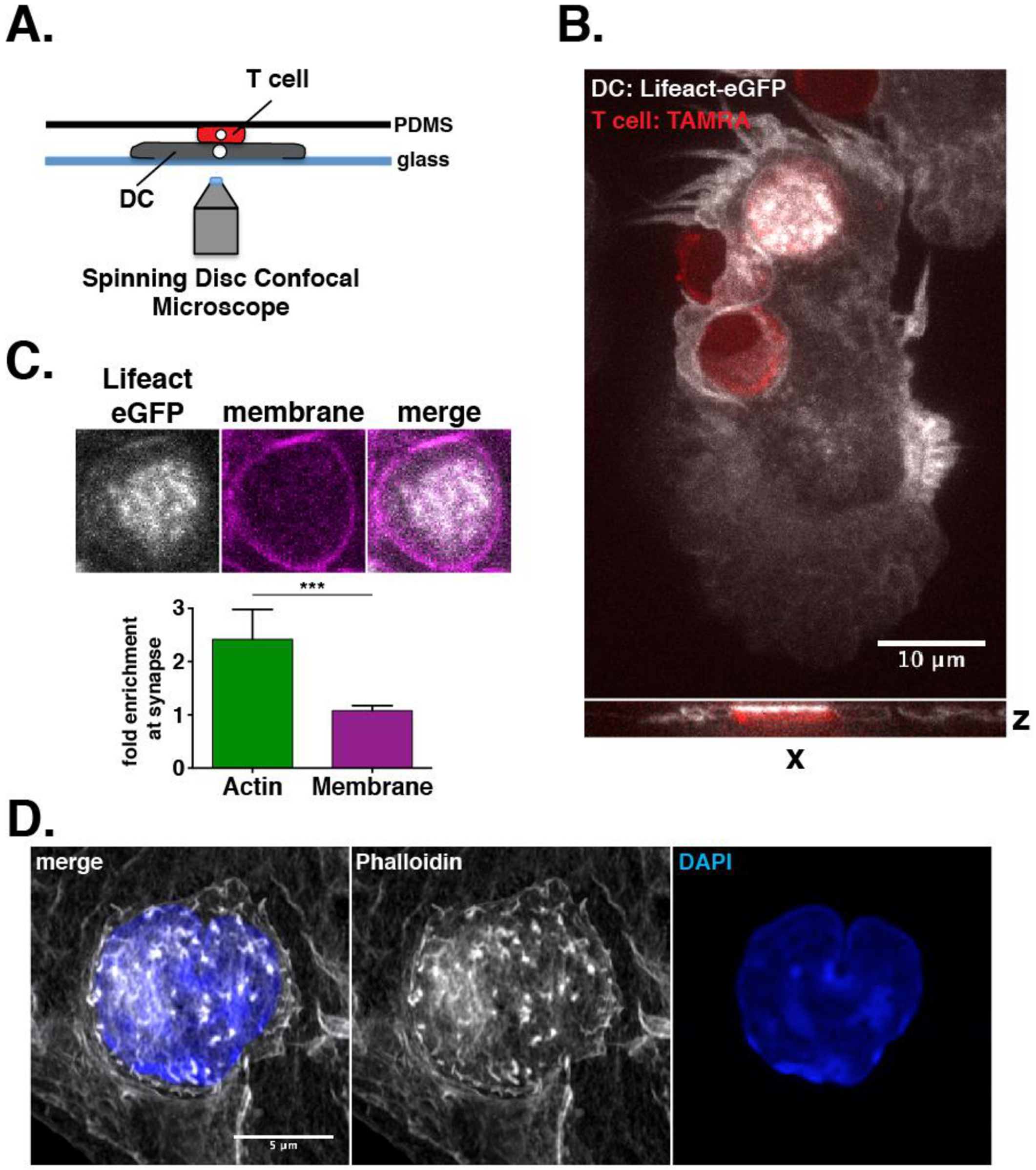

***Figure 11.* Dendritic cell F-actin at the DC-T cell immunological synapse.** (**A**) Scheme of imaging setup. (**B**) *top:* Snapshot of mDC expressing Lifeact-eGFP (grey) interacting with TAMRA stained T cells (red) in 3µm confiner, *bottom:* z-reconstruction of DC-T cell contact formed in the horizontal imaging plane. (**C**) *top:* Snapshots of IS formed between Lifeact-eGFP (grey) and membrane Tomato (magenta) expressing mDC and T cell (not visible), *bottom:* quantification of actin (Lifeact-eGFP) and membrane (membrane Tomato) enrichment at IS relative to non-IS region. Mann-Whitney test, *** p=0.0002, n=8 synapses from 3 different DC-T cell contacts. (**D**) Snapshot of phalloidin and DAPI stained DC-T cell synapse.

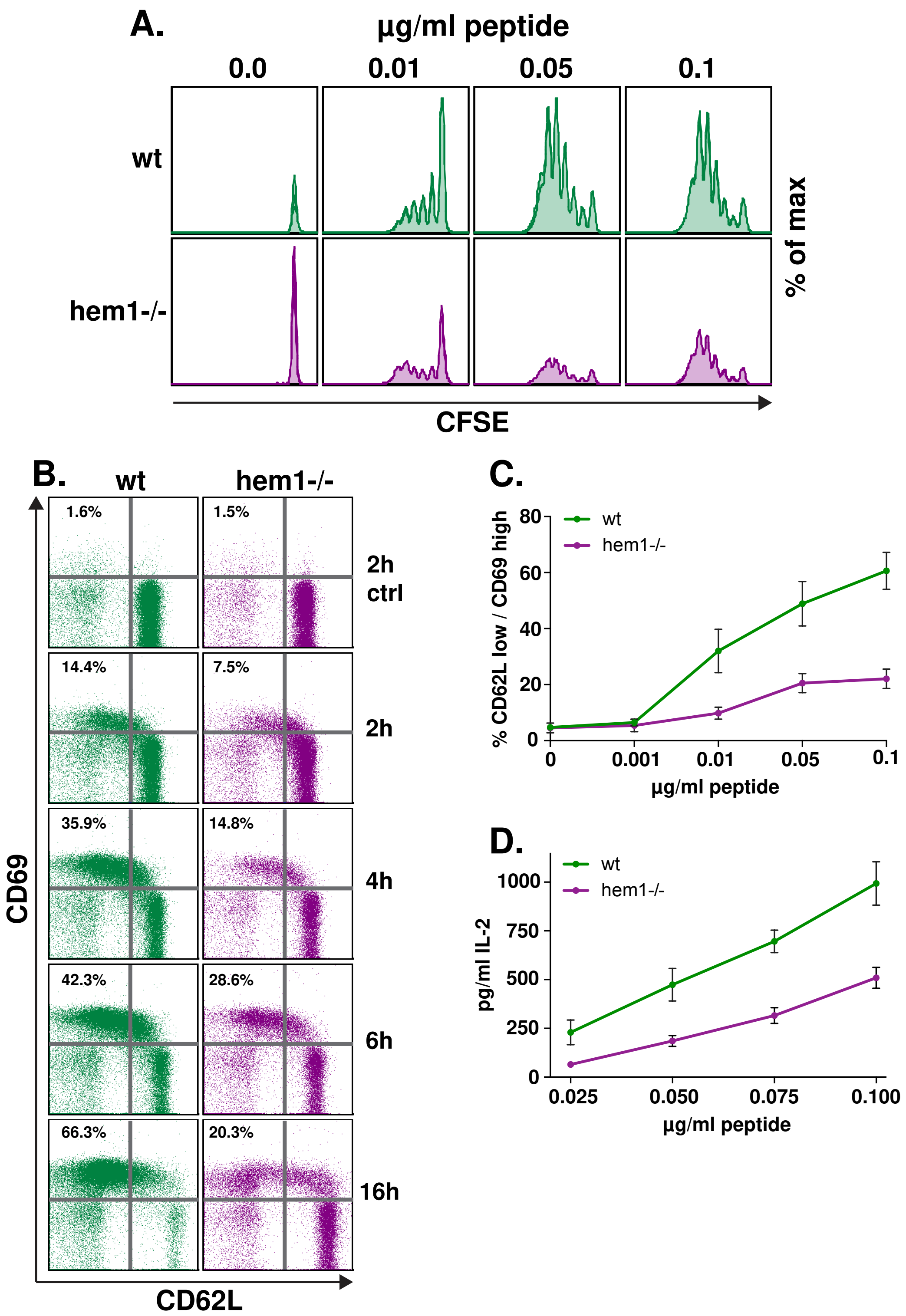

Figure 12. **Characterization of T cell priming defects of hem1-/- DC.** (**A**) FACS analysis of CFSE dilution-T cell proliferation assays under varying OVA peptide concentrations, 96h after start of OT-II TCR CD4+, CFSE stained T cell and wt or hem1-/- mDC co-culture. (**B**) FACS stainings for CD62L and CD69, pre-gated on CD4, 2, 4, 6 or 16h after start of wt or hem1-/- DC-T cell co-cultures in the presence of 0.1µg/ml OVA peptide. (**C**) Quantification of CD62L and CD69 stainings shown in (B) under varying peptide concentrations, 16h after start of co-culture. Pooled from three biologically independent experiments. (**D**) Supernatant IL-2 levels 16h after start of wt or hem1-/- mDC-T cell co-cultures, measured by ELISA. Data were pooled from three biologically independent experiments

Next, we turned to the dynamics of DC F-actin at the IS, employing fast confocal imaging of synapses formed between Lifeact-eGFP expressing DCs and T cells in our confiner setup. This revealed that F-actin foci exhibit variable lifetimes of a few seconds up to the whole imaging period of about three minutes. F-actin foci are formed throughout the whole synaptic interface and there is no centripetal flow towards an actin-free central region as has been described for the prototypical T cell synapse (Fig.13A). Importantly, Arp2/3 appears in similar structures, suggesting that synaptic F-actin is mainly branched (Fig.13B). Interestingly, we could not observe any apparent changes in F-actin foci dynamics at synapses formed between WAVE or WASP depleted DCs and T cells. However, we detected a clear overall reduction of DC F-actin enrichment at these synapses (Fig.13A and C). To determine the organization and dynamics of T cell- in relation to DC F-actin we imaged synapses formed between Lifeact-mCherry expressing wt DCs and TCR transgenic T cells expressing Lifeact-eGFP. T cell F-actin appears in similar foci as in DCs but importantly seems to be anti-correlated with actin polymerization in DCs (Fig.13C).

Interestingly, T cells form numerous actin-dependent microvilli that recently have been shown to rapidly scan surfaces for ligands in the form of pMHC [70],[91]. Together with the notion that DC-T cell synapses are multifocal [77], this intrigued us to ask the question if the observed F-actin foci in both cell types correspond to regions of microvilli formation. Potentially, this could generate tightly interlocked synapses with a large surface area. We further speculated that the reduced synaptic F-actin levels in WAVE deficient DCs might lead to ultra structural changes that potentially explain their T cell priming defects. To test these hypotheses we decided to resolve the ultrastructure of wt and hem1-/- DC-T cell synapses by electron microscopy. Cells were allowed to interact for two hours on glass slides and were then fixed by high pressure freezing (HPF), which leads to far better preservation of membranes compared to chemical fixation [92]. After freeze-substitution and resin embedding 70nm sections were cut and imaged, using an automated serial sectioning system followed by a semi-automated imaging procedure. This allowed us to fully reconstruct the ultra structure of synapses formed between wt or hem1-/- DCs and T cells. DCs appeared to entangle T cells, reminiscent of previous observations (Fig.14A and D) [81]. Furthermore, T cell microvilli were readily visible in conjugates formed with wt DCs and sometimes penetrated deeply into the DCs cell body. However, we could not observe microvilli emanating from the DC. Instead, the DC cell membrane appeared relatively flat and in close apposition to the T cell membrane, except where it was invaginated by T cell protrusions (Fig.14B-D). Surprisingly, we could not observe any T Cell microvilli formation in conjugates with hem1-/- DCs and the cell membranes appeared to be flat and in very close apposition (Fig.14D-G).

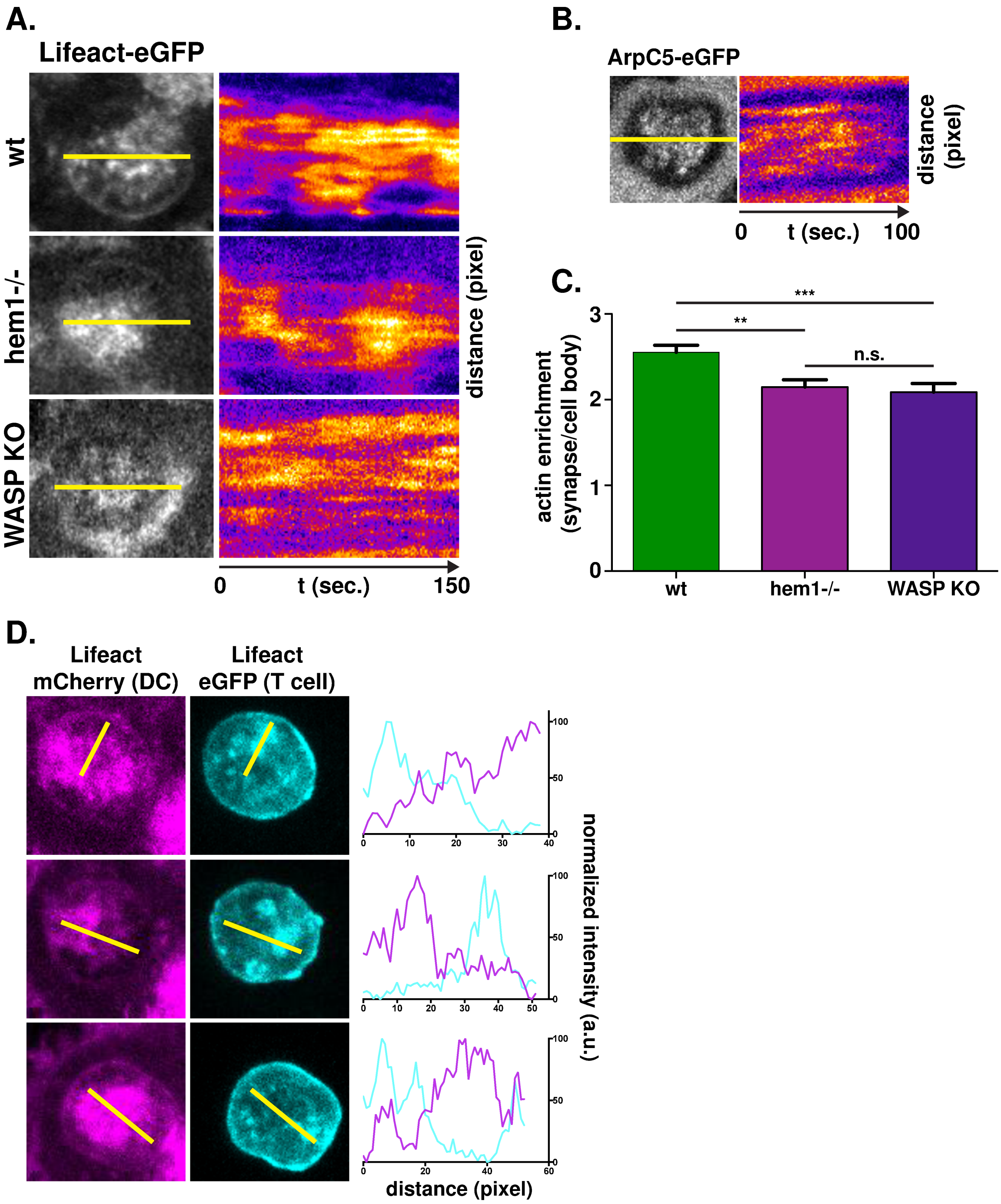

Figure 13. **F-actin dynamics at the DC-T cell immunological synapse.** (**A**) *left:* Snapshots of time-lapse movies of ISs formed between wt, hem1-/- or WASP KO Lifeact-eGFP expressing mDCs and T cells in 3µm confiner. *right*: kymographs along yellow lines on the left, showing F-actin foci dynamics over time. (**B**) *left:* Snapshot of time-lapse movie of IS formed between wt ArpC5-eGFP expressing mDC. *right*: kymograph along yellow line on the left, showing ArpC5-eGFP dynamics over time. (**C**) Quantification of F-actin enrichment relative to the cell body at synapses of Lifeact-eGFP expressing wt, hem1-/- or WASP KO mDCs and T cells. Kruskal-Wallis test, ** p<0.001 (wt vs. hem1-/-), *** p<0.0001 (wt vs. WASP KO), n=81/58/59 (wt/hem1-/-/WASP KO) individual synapses. (**C**) *left and middle:* Snapshots of time-lapse movie of IS formed between Lifeact-mCherry expressing mDC and Lifeact-eGFP expressing T cell. *right:* normalized Lifeact- mCherry or eGFP intensities along yellow lines shown on the left and middle.

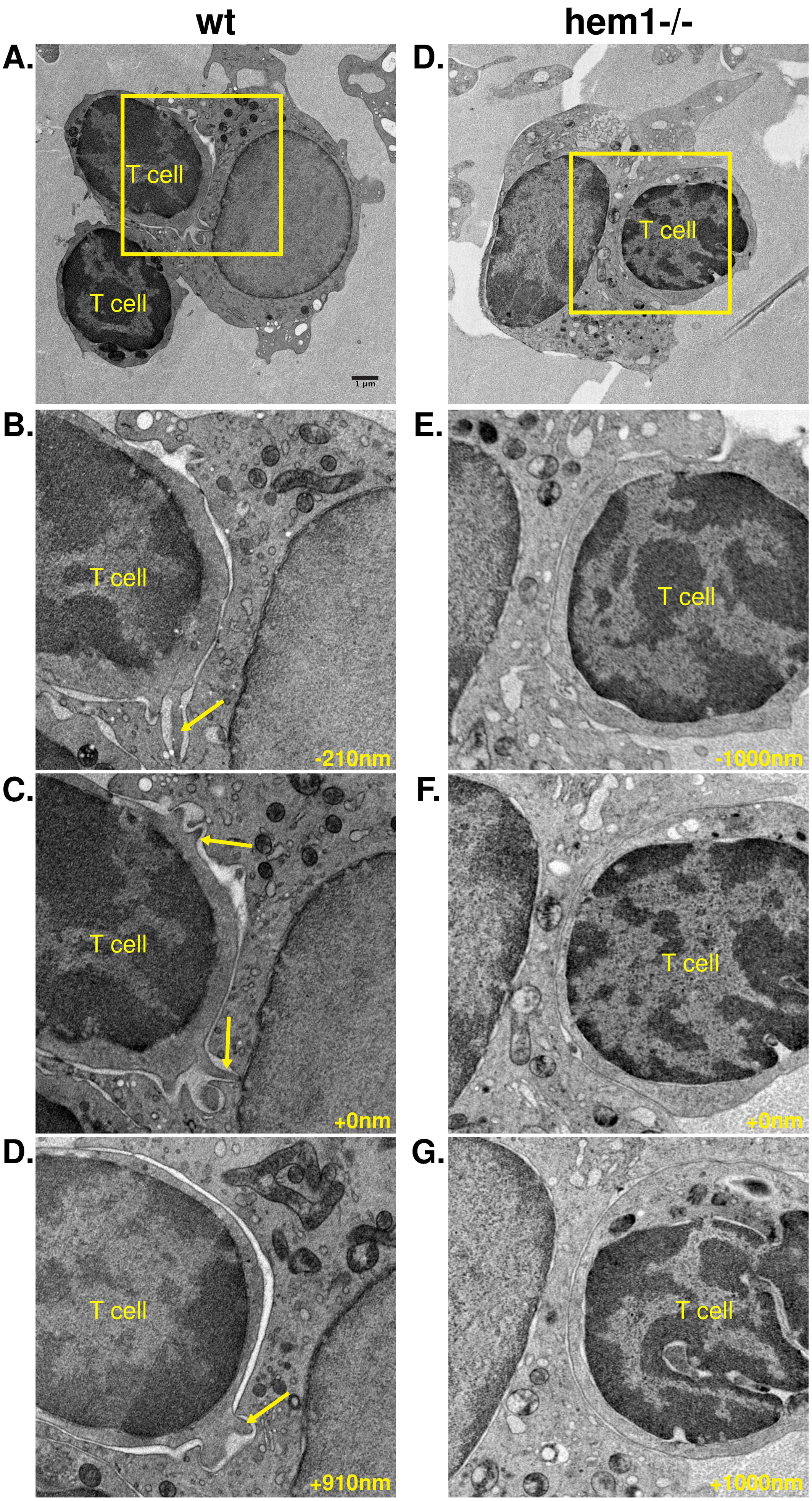
wt
hem1-/-
A.
T cell
T cell
1 µm
D.
T cell
B.
T cell
-210nm
E.
T cell
-1000nm
C.
T cell
+0nm
F.
T cell
+0nm
D.
T cell
+910nm
G.
T cell
+1000nm

Figure 14. **Electron microscopy of wt and hem1-/- DC-T cell immunological synapses.** (**A,D**) Representative overview images of one serial section of wt or hem1-/- mDC-T cell immunological synapse. (**B-G**) Magnified regions corresponding to yellow box in (A, wt) or (D, hem1-/-) at different z-positions relative to (C) or (F). Yellow arrows highlight protrusion formation.

These results lead us to hypothesize that altered mechanical properties of hem1-/- DCs might be the explanation for the observed phenotype. Consequently, we used atomic force microscopy to pull tethers from wt and hem1-/- DCs to determine their membrane tension. Interestingly, hem1-/- DCs had a significantly higher membrane tension, which might prevent T cells from protruding microvilli into the DCs cell body.

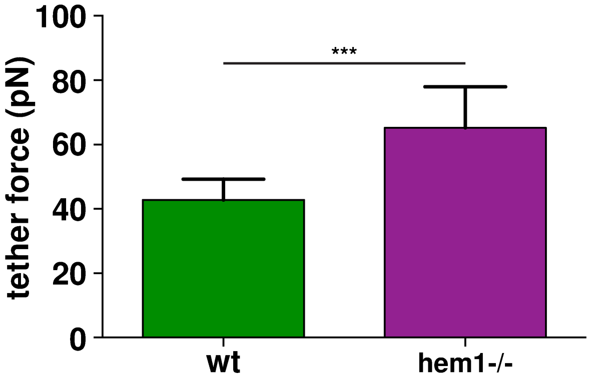

Figure 15. **Membrane tension of wt and hem1-/- DCs.** Tether force as a measure for membrane tension in wt and hem1-/- mDCs. unpaired t-test, *** $p<0.0001$, n=11/7 (wt/hem1-/-) individual cells from 3 biologically independent experiments, conducted by Alba Diz-Munoz, EMBL Heidelberg.

5.5 Discussion and future directions

In this study we used a novel imaging approach to study F-actin dynamics at the immunological synapse for the first time. Confinement of DCs and T cells leads to preferential formation of the IS in one horizontal imaging plane that is ideally suited for fast confocal imaging. DC and T cell F-actin appears throughout the whole synaptic interface in foci that are dynamic, but do not undergo centripetal flow as has been described for the prototypical T cell IS. Arp2/3 appears in similar structures at the IS, suggesting that branched actin networks play an important role in F-actin foci formation. Consequently, DCs that lack the NPF WAVE show severe T cell priming defects that correlate with reduced F-actin levels at the IS, which can be also observed in WASP deficient DCs. In both cases F-actin foci are still formed and thus our data suggest that WASP and WAVE cooperatively activate Arp2/3 to nucleate actin at the IS. Recent observations of actin dependent, TCR bearing microvilli on T cells intrigued us to test if the observed F-actin foci in our setup correspond to microvilli formation by T cells and DCs at the IS. To this end we resolved the IS ultrastructure by EM. Interestingly, we found that T cell microvilli deeply invaginate the DC membrane but could not detect DC membrane protrusions at the IS. These results stand in conflict to earlier EM studies of the DC-T cell IS that either detected only small scale membrane undulations [77] or that found T cell microvilli, but no deep invaginations of the DC membrane [78]. However, we want to point out that these studies used room temperature fixation for sample preparation. In contrast, HPF, which was our method of choice, is supposed to give far better results in terms of membrane structure preservation. In support of this idea, a HPF EM study of T cell – CH27 B cell lymphoma synapses could also identify T cell microvilli that deeply penetrate into the APC [93]. Strikingly, we found that T cells fail to form microvilli in conjugation with hem1-/- DCs and no invaginations were formed, coinciding with higher membrane tension of the WAVE deficient DCs.

These results raise three main questions: (1) what is the cause for higher membrane tension in WAVE depleted DCs, (2) what is the functional importance of T cell microvilli at the IS, (3) what is the role DC F-actin if not protrusion formation.

We recently showed that hem1-/- DCs have a lower level of F-actin compared to wt DCs [94]. Therefore, one explanation for the elevated membrane tension in WAVE depleted DCs might be an imbalance between F-actin and myosin, making these cells more contractile. Potentially, T cells are unable to overcome the increased resistance and fail to form microvilli against the DCs plasma membrane. To test this hypothesis we aim to artificially increase membrane tension of wt DCs, followed by ultrastructural characterization of the synapses formed with T cells.

Although it has been suggested that microvilli serve to increase the surface area between APC and T cell it has been recently shown that the TCR mainly localizes to the tips of microvilli. Therefore, the formation of microvilli in T cells might be required to form regions with high membrane curvature that allows clustering of TCR signaling components as has been recently suggested [79]. Conversely, membrane invagination might lead to local clustering of MHCII or ICAM-1 on the DC side of the synapse. Consequently, one of our immediate aims is to determine their localization and to test if TCR complex components fail to cluster in synapses formed between T cells and hem1-/- DCs.

The so far discussed results shed light on the overall importance of cell mechanics and force balance in T cell priming by DCs. In contrast, the exact role of DC F-actin, directly at the IS remains unknown and we ruled out the possibility that it corresponds to protrusion formation. However, the correlation we found between F-actin enrichment at the IS and T cell priming efficiency is in line with a model of DC ICAM-1 immobilization mentioned earlier [88]. In this model, the DC F-actin cytoskeleton serves to immobilize and cluster ICAM-1, which serves as binding partner for LFA-1 on T cells. F-actin flow in T cells, which is linked to LFA-1, keeps it in its high affinity signaling state. This requires a counter force, provided by immobilized ICAM-1. In the framework of this model, reduced F-actin levels at the synapses of WAVE depleted DCs lead to reduced clustering of ICAM-1 and thus impairment of LFA-1 signaling, which we aim to test by determining the localization of ICAM-1 as mentioned before.

Another intriguing possibility is that DC F-actin has a role in endocytosis and recycling of MHCII or ICAM1 at the IS. It is firmly established that maturation of DCs leads to stalling of MHCII biosynthesis and re-distribution of the intracellular pool to the cell surface for antigen presentation where it undergoes extremely slow turnover [95]. However, it has been shown that encounter with primed T cells or antibody crosslinking leads to rapid endocytosis and depletion of MHCII from the DCs membrane [96]. Although our results were exclusively obtained with naïve T cells it is possible that there is some role for endocytosis in these early phases of T cell priming that ensures turnover of MHCII or other molecules. Therefore, we also aim to perform pioneering experiments in this direction by co-localizing F-actin foci with early endosome markers.

5.6 Material and methods

Cell culture

R10 medium, consisting of RPMI 1640, supplemented with 10% Fetal Calf Serum (FCS), 2mM L-Glutamin, 100U/ml Penicillin, 100µg/ml Streptomycin and 50µM 2-Mercaptoethanol (all Thermofisher), was used as basic medium for all cells if not noted otherwise.

Mice

OT-II (B6.Cg-Tg(TcraTcrb)425Cbn/J, Jackson), WASP and hem1 knock-out mice have been described previously and were bred to Lifeact-eGFP mice in the C57BL/6 background [51],[97]–[99]. To obtain Lifeact-eGFP – membrane Tomato double transgenics, Lifeact-eGFP mice were bred to mTmG (Gt(ROSA)26Sor$^{tm4(ACTB\text{-}tdTomato,\text{-}EGFP)Luo}$IJ, Jackson) animals.

Dendritic cell generation

DCs were differentiated from the bone marrow of male or female 6-12 week old mice as described previously [30]. In brief, 2x10^6 (1.25x10^6 in case of hem1-/-) bone marrow cells were seeded into 94mm petri dishes in 9ml R10 and 1ml in-house generated supernatant of a granulocyte-macrophage colony stimulating factor (GM-CSF) producing hybridoma cell line. Cells were collected from the supernatant on day 8 or 9 and stimulated with LPS over night. Only cells from the supernatant were used for experiments.

Lentiviral infection of bone marrow

The Lifeact-mCherry plasmid was obtained by replacing eGFP with mCherry on a previously described plasmid [100]. The ArpC5-eGFP was as described [101]. Both reporter constructs were PCR amplified with primers that contained gateway sites to first integrate them into pDONR221, which was then used to obtain pLenti6.3 expression plasmids (both Thermofisher). Viruses were produced in LX-293T cells according to standard procedures. 4x10^6 bone marrow cells per well from a freshly sacrificed wt mouse were seeded in a 12-well dish in 900µl R10 and 100µl GM-CSF and incubated over night in an incubator. On the following day, 500µl virus together with 8µg/ml polybren were added and plates were spun with 2000rpm. for 2h at 37°C. After centrifugation, 500µl were taken off and cells from one well were re-suspended in 9ml R10 and 1ml GM-CSF in a petri dish. Cells were then treated like a regular DC culture. FACS sorting was used to enrich for fluorescent cells before experiments.

T cell isolation

CD4+ T cells were isolated from male or female 6-12 week old OT-II mice by negative selection, using the ‘EasySep Mouse CD4+ T cell isolation’ kit (Stemcell). For some assays, T cells were stained with 2.5µM 5-(and-6)-Carboxytetramethylrhodamine (TAMRA, Thermofisher) or 1µM Carboxyfluoresceinsuccinimidylester (CFSE) in PBS for 10min. at room temperature (TAMRA) or at 37°C (CFSE).

FACS stainings

All stainings were carried out in FACS Buffer (1x PBS, 2mM EDTA, 1% BSA) for 15min. at 4°C. Antibodies and reagents were obtained from ebioscience and used in the following dilutions: rat anti-mouse CD62L-PE (MEL-14), 1/1500; armenian hamster anti-mouse CD69-APC-eFluor780 (H1.2F3), 1/200; rat anti-mouse CD4-eFluor450 (GK1.5), 1/800; armenian hamster anti-mouse Cd11c-APC (N418), 1/300; rat anti-mouse MHCII-eFluor450 (M5/114.15.2), 1/800; 7-amino-actinomycin D (7AAD), 1/200. Prior to staining of DCs, Fc receptors were blocked (using anti-mouse CD16/CD32, 1/100, 93) to prevent unspecific antibody binding.

T cell proliferation and activation assays

T cell proliferation assays were carried out in 96-well round bottom plates by co-incubation of 10.000 DCs with 50.000 freshly isolated and CFSE stained CD4+ OT-II cells in the presence of varying concentrations of homemade OVA 323-339 peptide. For some assays, DCs were pre-treated with 1µM mycalolide B at 37°C for 15min., followed by three washes with R10. After 96h plates were spun down and cells were stained with 7AAD and for CD4+. Analysis was carried out on a BD FACS Canto II, equipped with an automated high throughput sampler.

T cell activation assays were carried out in a similar way at respective time-points by staining for CD62L and CD69. In this case cells were not stained with CFSE or 7AAD. To determine IL-2 levels, 100µl of supernatant were removed after 16h and analyzed using the IL-2 mouse ELISA kit (Thermofisher).

Light microscopy

For live-cell imaging, 0.1µg/ml OVA peptide loaded DCs and T cells were confined between glass slides and 3µm PDMS pillars that have been described previously [51] and placed in an incubator for 1h. Microscopy was then carried out on a motorized and heated stage at 37°C and 5% CO_2 with an inverted microscope (Zeiss), equipped with a spinning-disc system (iXon897, Andor), a Plan-Apochromat 100×/1.4 oil objective (Zeiss) and a 488 laser. For fixed sample preparation, DCs and T cells were injected between glass slides and a layer of agarose as has been described previously [102]. After 2h cells were fixed with 3% PFA and the agarose layer was carefully removed. Cells were then permeabilized with 0.2% TritonX-100 in PBS for 15min. and blocked with 1% BSA in PBS for 1h. Samples were then stained for 20min. with 1/40 diluted Alexa488 conjugated phalloidin and mounted with DAPI containing Fluoromount-G (all Thermofisher). Super resolution imaging was performed on an airyscan equipped LSM880 confocal microscope (Zeiss).

Lifeact-eGFP or membrane Tomato enrichment was calculated by dividing background subtracted mean grey values of synaptic- by the mean grey values of non-synaptic regions. Fiji [103] was used for all image handling, processing and quantification.

Electron microscopy

Sapphire discs were coated with carbon land markings and incubated with 0.001% Poly-L-Lysine (Sigma) in water over night at 4°C. On the next day, discs were placed in a 12-well dish, rinsed twice with water and dried for 4h at room temperature. T cells and 0.1µg/ml OVA peptide loaded wt or hem1-/- DCs were seeded in R10 and allowed to interact for 2h. Samples were mildly pre-fixed with 1% PFA for 10min. and then immediately transferred to a Baltec HPM010 machine for high pressure freezing. Freeze substitution was carried out in an automated Leica EMAFS machine according to the following protocol: 23.5h at -82°C with acetone and 0.1% tannic acid, followed by a change to acetone, 1% osmium tetroxide and 0.2% uranylacetate and incubation for another 7h. In the next 1.5h the temperature was then raised to -60°C, held for 3h and then raised to -30°C over the course of 2h. The temperature was then raised to 0°C. Embedding was started by acetone washes and infiltration of the samples with resin/propylene oxide mixtures with increasing amounts of resin. Samples were infiltrated with pure resin over night and then allowed to polymerize at 60°C for 2-3 days. Serial sections of 70nm were cut with an automated tape collecting ultra microtome (ATUMtome, RMC) and placed on a waiver for semi-automated image collection with a Merlin compact VP field-emission scanning electron microscope (Zeiss). The Fiji plugin ‘TrakEM2’ [104] was used for image alignment.

Atomic force microscopy

Membrane tension was measured by pulling tethers of wt and hem1-/- DCs as has been described previously [105]. To this end, cells were seeded onto poly-L-lysine coated cover slips and tethers were pulled with the cantilever of an atomic force microscope until they ruptured and the tether force, a readout for membrane tension was recorded.

6 Concluding remarks

In the here presented thesis we studied the role of branched actin networks in the context of two aspects of dendritic cell biology: migration and antigen presentation. The NPFs WAVE and WASP are non-redundant and show differences in their localization in DCs. While WAVE always localizes to lamellipodia of DCs, WASP is completely absent from the leading edge of immature DCs. Although it is currently unclear what leads to this sub compartmentalization it is a remarkable example for how branched actin polymerization is directed to certain compartments to construct different structures. While WAVE nucleates branched F-actin to construct lamellipodia, WASP has been shown to be involved in the formation of podosomes that facilitate antigen uptake [106]. Upon maturation, antigen uptake ceases and thus WASP is redirected for a new function in migration at the leading edge. However, this precise function in mature DCs remains to be elucidated and again seems to be non-redundant with WAVE as WASP is not able to restore lamellipodia formation in mature DCs while WASP deficient DCs exhibit lamellipodia (personal observation) but show defective migration [86],[107].

The different roles of WAVE and WASP in different maturation stages of DCs allowed us to generate cells with different types and numbers of protrusions and to study their role in migration. Our results challenge the paradigm of lamellipodia as force transducing units and show that they rather serve a sensory function in leukocyte migration.

Once DCs begin to present antigen to T cells in the lymph node the actin nucleation machinery is re-directed to this new task. Again branched actin networks play a decisive role as interference with WASP or, as shown here, WAVE leads to severe defects in T cell priming [86],[107]. However, the precise role of the two NPFs at the DC IS remains unknown. We observed a less severe T cell priming defect of WASP deficient- compared to WAVE deficient DCs (personal observation), which indicates that the two NPFs have not completely redundant functions at the IS. However, according to our imaging data in both, WAVE and WASP deficient DCs, there is a comparable reduction of F-actin enrichment at the IS but no clear structural change (e.g. loss of actin foci) was apparent. This might indicate that DC branched actin merely constructs a local anchorage platform with ICAM-1 [88]. In this scenario the concerted action of WAVE and WASP would be necessary to reach optimal branched F-actin enrichment for T cell anchorage and priming. Super resolution microscopy of actin and other factors in WAVE and WASP deficient DC-T cell synapses might help to resolve these open questions.

Finally, we found that WAVE deficient DCs show an increase in membrane tension that correlates with the absence of T cell microvilli at the IS. Although much work remains to be done to thoroughly characterize this phenotype, we think it might point towards an exciting but previously underappreciated role of cellular mechanics in T cell priming.

References

1. **Banchereau J**, **Steinman RM**. Dendritic cells and the control of immunity. *Nature*. 1998; **392**:245–52. Available at: http://www.ncbi.nlm.nih.gov/pubmed/9521319.DOI: 10.1038/32588.

2. **Förster R**, **Davalos-Misslitz AC**, **Rot A**. CCR7 and its ligands: balancing immunity and tolerance. *Nat. Rev. Immunol.* 2008; **8**:362–71. Available at: http://www.ncbi.nlm.nih.gov/pubmed/18379575 [Accessed November 12, 2012].DOI: 10.1038/nri2297.

3. **Blanchoin L**, **Boujemaa-Paterski R**, **Sykes C**, **Plastino J**. Actin dynamics, architecture, and mechanics in cell motility. *Physiol. Rev.* 2014; **94**:235–63. Available at: http://www.ncbi.nlm.nih.gov/pubmed/24382887 [Accessed December 21, 2015].DOI: 10.1152/physrev.00018.2013.

4. **Pollard TD**, **Borisy GG**, **Haven N**. Cellular Motility Driven by Assembly and Disassembly of Actin Filaments. 2003; **112**:453–465.

5. **Welch MD**, **Mullins RD**. Cellular control of actin nucleation. *Annu. Rev. Cell Dev. Biol.* 2002; **18**:247–88. Available at: http://www.ncbi.nlm.nih.gov/pubmed/12142287 [Accessed May 31, 2013].DOI: 10.1146/annurev.cellbio.18.040202.112133.

6. **Takenawa T**, **Suetsugu S**. The WASP-WAVE protein network: connecting the membrane to the cytoskeleton. *Nat. Rev. Mol. Cell Biol.* 2007; **8**:37–48. Available at: http://www.ncbi.nlm.nih.gov/pubmed/17183359 [Accessed March 1, 2013].DOI: 10.1038/nrm2069.

7. **Chesarone MA**, **Dupage AG**, **Goode BL**. Unleashing formins to remodel the actin and microtubule cytoskeletons. *Nat. Rev. Mol. Cell Biol.* 2010; **11**:62–74. Available at: http://dx.doi.org/10.1038/nrm2816.DOI: 10.1038/nrm2816.

8. **Vicente-Manzanares M**, **Ma X**, **Adelstein RS**, **Horwitz AR**. Non-muscle myosin II takes centre stage in cell adhesion and migration. *Nat. Rev. Mol. Cell Biol.* 2009; **10**:778–790. Available at: http://dx.doi.org/10.1038/nrm2786.DOI: 10.1038/nrm2786.

9. **Craig R**, **Woodhead JL**. Structure and function of myosin filaments. *Curr. Opin. Struct. Biol.* 2006; **16**:204–12.DOI: 10.1016/j.sbi.2006.03.006.

10. **Artemenko Y**, **Swaney KF**, **Devreotes PN**. *Cell Migration*. 2011.DOI: 10.1007/978-1-61779-207-6_20.

11. **Lämmermann T, Bader BL, Monkley SJ, Worbs T, Wedlich-Söldner R, Hirsch K, Keller M, *et al.*** Rapid leukocyte migration by integrin-independent flowing and squeezing. *Nature*. 2008; **453**:51–5. Available at: http://www.nature.com/doifinder/10.1038/nature06887%5Cnhttp://www.ncbi.nlm.nih.gov/pubmed/18451854.DOI: 10.1038/nature06887.

12. **Van Haastert PJM**, **Devreotes PN**. Chemotaxis: Signalling the way forward.

Nat. Rev. Mol. Cell Biol. 2004; **5**:626–634.DOI: 10.1038/nrm1435.

13. **Ridley AJ, Schwartz M a, Burridge K, Firtel R a, Ginsberg MH, Borisy G, Parsons JT, *et al.*** Cell migration: integrating signals from front to back. *Science*. 2003; **302**:1704–9. Available at: http://www.ncbi.nlm.nih.gov/pubmed/14657486 [Accessed February 27, 2013].DOI: 10.1126/science.1092053.

14. **Charest PG**, **Firtel RA**. Feedback signaling controls leading-edge formation during chemotaxis. *Curr. Opin. Genet. Dev.* 2006; **16**:339–347.DOI: 10.1016/j.gde.2006.06.016.

15. **Mitchison TJ**, **Cramer LP**. Actin-based cell motility and cell locomotion. *Cell*. 1996; **84**:371–379.DOI: 10.1016/S0092-8674(00)81281-7.

16. **Hynes RO**. Integrins: Bidirectional, allosteric signaling machines. *Cell*. 2002; **110**:673–687.DOI: 10.1016/S0092-8674(02)00971-6.

17. **Case LB**, **Waterman CM**. Integration of actin dynamics and cell adhesion by a three-dimensional, mechanosensitive molecular clutch. *Nat. Cell Biol.* 2015; **17**:955–963. Available at: http://dx.doi.org/10.1038/ncb3191.DOI: 10.1038/ncb3191.

18. **Suraneni P**, **Rubinstein B**, **Unruh JR**, **Durnin M**, **Hanein D**, **Li R**. The Arp2/3 complex is required for lamellipodia extension and directional fibroblast cell migration. *J. Cell Biol.* 2012; **197**:239–251.DOI: 10.1083/jcb.201112113.

19. **Wu C, Asokan SB, Berginski ME, Haynes EM, Sharpless NE, Griffith JD, Gomez SM, *et al.*** Arp2/3 is critical for lamellipodia and response to extracellular matrix cues but is dispensable for chemotaxis. *Cell*. 2012; **148**:973–87. Available at: http://www.pubmedcentral.nih.gov/articlerender.fcgi?artid=3707508&tool=pmcentrez&rendertype=abstract [Accessed March 1, 2016].DOI: 10.1016/j.cell.2011.12.034.

20. **Wu C, Haynes EM, Asokan SB, Simon JM, Sharpless NE, Baldwin AS, Davis IJ, *et al.*** Loss of Arp2/3 induces an NF-ŻB–dependent, nonautonomous effect on chemotactic signaling. 2013; **203**:907–916.DOI: 10.1083/jcb.201306032.

21. **Friedl P**, **Wolf K**. Plasticity of cell migration: A multiscale tuning model. *J. Cell Biol.* 2010; **188**:11–19.DOI: 10.1083/jcb.200909003.

22. **Lämmermann T, Bader BL, Monkley SJ, Worbs T, Wedlich-Soldner R, Hirsch K, Keller M, *et al.*** Rapid leukocyte migration by integrin independent flowing and squeezing. *Nature*. 2008; **453**:51.DOI: 10.1038/nature06887.

23. **Lämmermann T**, **Sixt M**. Mechanical modes of ‘amoeboid’ cell migration. *Curr. Opin. Cell Biol.* 2009; **21**:636–44. Available at: http://www.ncbi.nlm.nih.gov/pubmed/19523798 [Accessed March 1, 2016].DOI: 10.1016/j.ceb.2009.05.003.

24. **Yae K, Keng VW, Koike M, Yusa K, Kouno M, Uno Y, Kondoh G, *et al.*** Sleeping Beauty Transposon-Based Phenotypic Analysis of Mice: Lack of Arpc3 Results in Defective Trophoblast Outgrowth. *Mol. Cell. Biol.* 2006; **26**:6185–6196.

Available at: http://mcb.asm.org/cgi/doi/10.1128/MCB.00018-06.DOI: 10.1128/MCB.00018-06.

25. **Park H, Staehling-Hampton K, Appleby MW, Brunkow ME, Habib T, Zhang Y, Ramsdell F, *et al.*** A point mutation in the murine Hem1 gene reveals an essential role for Hematopoietic protein 1 in lymphopoiesis and innate immunity. *J. Exp. Med.* 2008; **205**:2899–913. Available at: http://www.pubmedcentral.nih.gov/articlerender.fcgi?artid=2585840&tool=pmcentrez&rendertype=abstract [Accessed April 24, 2013].DOI: 10.1084/jem.20080340.

26. **Yamakita Y, Matsumura F, Lipscomb MW, Chou P -c., Werlen G, Burkhardt JK, Yamashiro S.** Fascin1 Promotes Cell Migration of Mature Dendritic Cells. *J. Immunol.* 2011; **186**:2850–2859. Available at: http://www.jimmunol.org/cgi/doi/10.4049/jimmunol.1001667.DOI: 10.4049/jimmunol.1001667.

27. **Vargas P, Maiuri P, Bretou M, Sáez PJ, Pierobon P, Maurin M, Chabaud M, *et al.*** Innate control of actin nucleation determines two distinct migration behaviours in dendritic cells. *Nat. Cell Biol.* 2015; **18**:43–53. Available at: http://www.nature.com/doifinder/10.1038/ncb3284.DOI: 10.1038/ncb3284.

28. **Motility IV, Rotty JD, Brighton HE, Craig SL, Asokan SB, Cheng N, Ting JP, *et al.*** Arp2 / 3 Complex Is Required for Macrophage Integrin Functions but Is Dispensable for FcR Phagocytosis Article Arp2 / 3 Complex Is Required for Macrophage Integrin Functions but Is Dispensable for FcR Phagocytosis and In Vivo Motility. *Dev. Cell.* 2017:1–16. Available at: http://dx.doi.org/10.1016/j.devcel.2017.08.003.DOI: 10.1016/j.devcel.2017.08.003.

29. **Fritz-Laylin LK, Riel-Mehan M, Chen BC, Lord SJ, Goddard TD, Ferrin TE, Nicholson-Dykstra SM, *et al.*** Actin-Based protrusions of migrating neutrophils are intrinsically lamellar and facilitate direction changes. *Elife*. 2017; **6**:1–25.DOI: 10.7554/eLife.26990.

30. **Lutz MB, Kukutsch N, Ogilvie a L, Rössner S, Koch F, Romani N, Schuler G.** An advanced culture method for generating large quantities of highly pure dendritic cells from mouse bone marrow. *J. Immunol. Methods*. 1999; **223**:77–92. Available at: http://www.ncbi.nlm.nih.gov/pubmed/10037236.

31. **Inaba K, Inaba M, Romani N, Aya H, Deguchi M, Ikehara S, Muramatsu S, *et al.*** Generation of large numbers of dendritic cells from mouse bone marrow cultures supplemented with granulocyte/macrophage colony-stimulating factor. *J. Exp. Med.* 1992; **176**:1693–702. Available at: http://www.ncbi.nlm.nih.gov/pubmed/1460426.

32. **Sander JD, Joung JK.** CRISPR-Cas systems for editing, regulating and targeting genomes. *Nat. Biotechnol.* 2014; **32**:347–55. Available at: http://dx.doi.org/10.1038/nbt.2842.DOI: 10.1038/nbt.2842.

33. **Winzler C, Rovere P, Rescigno M, Granucci F, Penna G, Adorini L, Zimmermann VS, *et al.*** Maturation stages of mouse dendritic cells in growth factor-dependent long-term cultures. *J. Exp. Med.* 1997; **185**:317–28. Available at: http://www.pubmedcentral.nih.gov/articlerender.fcgi?artid=2196118&tool=pmcentrez

&rendertype=abstract.DOI: 10.1084/jem.185.2.317.

34. **Gasperi C**, **Rescigno M**, **Granucci F**, **Citterio S**, **Matyszak MK**, **Sciurpi MT**, **Lanfrancone L**. Retroviral gene transfer , rapid selection , and maintenance of the immature phenotype in mouse dendritic cells. 1999; **66**:263–267.

35. **Richter C**, **Thieme S**, **Bandoła J**, **Laugsch M**, **Anastassiadis K**, **Brenner S**. Generation of inducible immortalized dendritic cells with proper immune function in vitro and in vivo. *PLoS One*. 2013; **8**:e62621. Available at: http://www.pubmedcentral.nih.gov/articlerender.fcgi?artid=3633827&tool=pmcentrez &rendertype=abstract [Accessed June 7, 2013].DOI: 10.1371/journal.pone.0062621.

36. **Ruiz S**, **Beauvillain C**, **Mevelec MN**, **Roingeard P**, **Breton P**, **Bout D**, **Dimier-Poisson I**. A novel CD4-CD8alpha+CD205+CD11b- murine spleen dendritic cell line: establishment, characterization and functional analysis in a model of vaccination to toxoplasmosis. *Cell Microbiol*. 2005; **7**:1659–1671. Available at: http://www.ncbi.nlm.nih.gov/pubmed/16207252%5Cnhttp://onlinelibrary.wiley.com/store/10.1111/j.1462-5822.2005.00583.x/asset/j.1462-5822.2005.00583.x.pdf?v=1&t=hj899g1w&s=95bcdb303d48a052ac6bc97b657fff7ba71aa30f.DOI: 10.1111/j.1462-5822.2005.00583.x.

37. **Fuertes Marraco S a**, **Grosjean F**, **Duval A**, **Rosa M**, **Lavanchy C**, **Ashok D**, **Haller S**, ***et al.*** Novel murine dendritic cell lines: a powerful auxiliary tool for dendritic cell research. *Front. Immunol.* 2012; **3**:331. Available at: http://www.pubmedcentral.nih.gov/articlerender.fcgi?artid=3491238&tool=pmcentrez &rendertype=abstract [Accessed March 9, 2013].DOI: 10.3389/fimmu.2012.00331.

38. **Shen Z**, **Reznikoff G**, **Dranoff G**, **Rock KL**. Cloned dendritic cells can present exogenous antigens on both MHC class I and class II molecules. *J. Immunol.* 1997; **158**:2723–30. Available at: http://www.jimmunol.org/content/158/6/2723%5Cnhttp://www.jimmunol.org/%5Cnhttp://www.ncbi.nlm.nih.gov/pubmed/9058806.

39. **Fairchild PJ**, **Brook F a.**, **Gardner RL**, **Graça L**, **Strong V**, **Tone Y**, **Tone M**, ***et al.*** Directed differentiation of dendritic cells from mouse embryonic stem cells. *Curr. Biol.* 2000; **10**:1515–1518.DOI: 10.1016/S0960-9822(00)00824-1.

40. **Fairchild PJ**, **Nolan KF**, **Cartland S**, **Graça L**, **Waldmann H**. Stable lines of genetically modified dendritic cells from mouse embryonic stem cells. *Transplantation*. 2003; **76**:606–608.DOI: 10.1097/01.TP.0000074318.96235.B3.

41. **Rosas M**, **Osorio F**, **Robinson MJ**, **Davies LC**, **Dierkes N**, **Jones SA**, **Reis E Sousa C**, ***et al.*** Hoxb8 conditionally immortalised macrophage lines model inflammatory monocytic cells with important similarity to dendritic cells. *Eur. J. Immunol.* 2011; **41**:356–365.DOI: 10.1002/eji.201040962.

42. **Redecke V**, **Wu R**, **Zhou J**, **Finkelstein D**, **Chaturvedi V**, **High AA**, **Häcker H**. Hematopoietic progenitor cell lines with myeloid and lymphoid potential. *Nat. Methods*. 2013; **10**:795–803. Available at: http://www.nature.com/doifinder/10.1038/nmeth.2510.DOI: 10.1038/nmeth.2510.

43. **Bhaya D**, **Davison M**, **Barrangou R**. CRISPR-Cas systems in bacteria and

archaea: versatile small RNAs for adaptive defense and regulation. *Annu. Rev. Genet.* 2011; **45**:273–97. Available at: http://www.ncbi.nlm.nih.gov/pubmed/22060043 [Accessed October 19, 2013].DOI: 10.1146/annurev-genet-110410-132430.

44. **Wang H, La Russa M, Qi LS**. CRISPR/Cas9 in Genome Editing and Beyond. *Annu. Rev. Biochem.* 2016; **85**:227–264. Available at: http://www.annualreviews.org/doi/10.1146/annurev-biochem-060815-014607.DOI: 10.1146/annurev-biochem-060815-014607.

45. **Hsu PD, Scott D a, Weinstein J a, Ran FA, Konermann S, Agarwala V, Li Y, *et al.*** DNA targeting specificity of RNA-guided Cas9 nucleases. *Nat. Biotechnol.* 2013; **31**:827–32. Available at: http://www.ncbi.nlm.nih.gov/pubmed/23873081 [Accessed March 19, 2014].DOI: 10.1038/nbt.2647.

46. **Doench JG, Hartenian E, Graham DB, Tothova Z, Hegde M, Smith I, Sullender M, *et al.*** Rational design of highly active sgRNAs for CRISPR-Cas9-mediated gene inactivation. *Nat. Biotechnol.* 2014; **32**:1262–1267. Available at: http://dx.doi.org/10.1038/nbt.3026.DOI: 10.1038/nbt.3026.

47. **Slaymaker IM, Gao L, Zetsche B, Scott DA, Yan WX, Zhang F**. Rationally engineered Cas9 nucleases with improved specificity. *Science (80-.).* 2016; **351**:84–88.DOI: 10.1126/science.aad5227.

48. **Förster R, Schubel A, Breitfeld D, Kremmer E, Renner-Müller I, Wolf E, Lipp M**. CCR7 coordinates the primary immune response by establishing functional microenvironments in secondary lymphoid organs. *Cell.* 1999; **99**:23–33.DOI: 10.1016/S0092-8674(00)80059-8.

49. **Vargas P, Barbier L, Sáez PJ, Piel M**. Mechanisms for fast cell migration in complex environments. *Curr. Opin. Cell Biol.* 2017; **48**:72–78.DOI: 10.1016/j.ceb.2017.04.007.

50. **Tinevez JY, Perry N, Schindelin J, Hoopes GM, Reynolds GD, Laplantine E, Bednarek SY, *et al.*** TrackMate: An open and extensible platform for single-particle tracking. *Methods*. 2017; **115**:80–90. Available at: http://dx.doi.org/10.1016/j.ymeth.2016.09.016.DOI: 10.1016/j.ymeth.2016.09.016.

51. **Leithner A, Eichner A, Müller J, Reversat A, Brown M, Schwarz J, Merrin J, *et al.*** Diversified actin protrusions promote environmental exploration but are dispensable for locomotion of leukocytes. *Nat. Cell Biol.* 2016; **18**:1253–1259. Available at: http://www.nature.com/doifinder/10.1038/ncb3426.DOI: 10.1038/ncb3426.

52. **Krummel MF, Davis MM**. Dynamics of the immunological synapse : finding , establishing and solidifying a connection. :66–74.

53. **Monks CRF, Freiberg BA, Kupfer H, Sciaky N, Kupfer A**. Three-dimensional segregation of supramolecular activation clusters in T cells. *Nature*. 1998; **395**:82–86. Available at: http://www.nature.com/articles/25764.DOI: 10.1038/25764.

54. **Wülfing C**, **Sjaastad MD**, **Davis MM**. Visualizing the dynamics of T cell activation: intracellular adhesion molecule 1 migrates rapidly to the T cell/B cell interface and acts to sustain calcium levels. *Proc. Natl. Acad. Sci. U. S. A.* 1998; **95**:6302–7. Available at: http://www.ncbi.nlm.nih.gov/pubmed/9600960.

55. **Grakoui a.** The Immunological Synapse: A Molecular Machine Controlling T Cell Activation. *Science (80-.).* 1999; **285**:221–227. Available at: http://www.sciencemag.org/cgi/doi/10.1126/science.285.5425.221 [Accessed March 5, 2013].DOI: 10.1126/science.285.5425.221.

56. **Al-Alwan M**, **Rowden G**. Cutting edge: the dendritic cell cytoskeleton is critical for the formation of the immunological synapse. *J. Immunol.* 2001.

57. **Klieger Y, Almogi-hazan O, Ish-shalom E, Pato A, Pauker MH, Barda-saad M, Wang L, *et al.*** Unique ζ-chain motifs mediate a direct TCR-actin linkage critical for immunological synapse formation and T-cell activation. 2014:58–68.DOI: 10.1002/eji.201243099.

58. **Smith-Garvin JE**, **Koretzky G a**, **Jordan MS**. T cell activation. *Annu. Rev. Immunol.* 2009; **27**:591–619. Available at: http://www.pubmedcentral.nih.gov/articlerender.fcgi?artid=2740335&tool=pmcentrez&rendertype=abstract [Accessed March 1, 2013].DOI: 10.1146/annurev.immunol.021908.132706.

59. **Comrie WA**, **Burkhardt JK**. Action and traction: Cytoskeletal control of receptor triggering at the immunological synapse. *Front. Immunol.* 2016; **7**:1–25.DOI: 10.3389/fimmu.2016.00068.

60. **Yi J**, **Wu XS**, **Crites T**, **Hammer JA**, **Pollard TD**. Actin retrograde flow and actomyosin II arc contraction drive receptor cluster dynamics at the immunological synapse in Jurkat T cells. 2012.DOI: 10.1091/mbc.E11-08-0731.

61. **Babich A**, **Li S**, **O'Connor RS**, **Milone MC**, **Freedman BD**, **Burkhardt JK**. F-actin polymerization and retrograde flow drive sustained PLCγ1 signaling during T cell activation. *J. Cell Biol.* 2012; **197**:775–87. Available at: http://www.pubmedcentral.nih.gov/articlerender.fcgi?artid=3373411&tool=pmcentrez&rendertype=abstract [Accessed March 1, 2016].DOI: 10.1083/jcb.201201018.

62. **Yokosuka T, Sakata-sogawa K, Kobayashi W, Hiroshima M, Hashimoto-tane A, Tokunaga M, Dustin ML, *et al.*** Newly generated T cell receptor microclusters initiate and sustain T cell activation by recruitment of Zap70 and SLP-76. 2005; **6**:1253–1262.DOI: 10.1038/ni1272.

63. **Sherman E, Barr V, Manley S, Patterson G, Balagopalan L, Akpan I, Regan CK, *et al.*** Functional nanoscale organization of signaling molecules downstream of the T cell antigen receptor. *Immunity*. 2011; **35**:705–720. Available at: http://dx.doi.org/10.1016/j.immuni.2011.10.004.DOI: 10.1016/j.immuni.2011.10.004.

64. **Lillemeier BF**, **Mörtelmaier MA**, **Forstner MB**, **Huppa JB**, **Groves JT**, **Davis MM**. TCR and Lat are expressed on separate protein islands on T cell membranes and concatenate during activation. *Nat. Immunol.* 2010; **11**:90–96.DOI: 10.1038/ni.1832.

65. **Kumari S, Depoil D, Martinelli R, Judokusumo E, Carmona G, Gertler FB, Kam LC, *et al.*** Actin foci facilitate activation of the phospholipase C-γ in primary T lymphocytes via the WASP pathway. *Elife*. 2015; **4**:1–31. Available at: http://www.pubmedcentral.nih.gov/articlerender.fcgi?artid=4355629&tool=pmcentrez&rendertype=abstract [Accessed March 1, 2016].DOI: 10.7554/eLife.04953.

66. **Tane AH**, **Sakuma M**, **Ike H**, **Yokosuka T**, **Kimura Y**, **Ohara O**, **Saito T**. Micro – adhesion rings surrounding TCR microclusters are essential for T cell activation. 2016:1–17.DOI: 10.1084/jem.20151088.

67. **Comrie W a**, **Babich A**, **Burkhardt JK**. F-actin flow drives affinity maturation and spatial organization of LFA-1 at the immunological synapse. *J. Cell Biol.* 2015; **208**:475–91. Available at: http://www.pubmedcentral.nih.gov/articlerender.fcgi?artid=4332248&tool=pmcentrez&rendertype=abstract [Accessed February 4, 2016].DOI: 10.1083/jcb.201406121.

68. **Hashimoto-Tane A**, **Yokosuka T**, **Sakata-Sogawa K**, **Sakuma M**, **Ishihara C**, **Tokunaga M**, **Saito T**. Dynein-Driven Transport of T Cell Receptor Microclusters Regulates Immune Synapse Formation and T Cell Activation. *Immunity*. 2011; **34**:919–931. Available at: http://dx.doi.org/10.1016/j.immuni.2011.05.012.DOI: 10.1016/j.immuni.2011.05.012.

69. **Choudhuri K, Llodrá J, Roth EW, Tsai J, Gordo S, Wucherpfennig KW, Kam LC, *et al.*** Polarized release of T-cell-receptor-enriched microvesicles at the immunological synapse. *Nature*. 2014; **507**:118–23. Available at: http://www.ncbi.nlm.nih.gov/pubmed/24487619 [Accessed March 20, 2014].DOI: 10.1038/nature12951.

70. **Cai E, Marchuk K, Beemiller P, Beppler C, Rubashkin MG, Weaver VM, Gérard A, *et al.*** Visualizing dynamic microvillar search and stabilization during ligand detection by T cells. *Science (80-.).* 2017; **356**. Available at: http://science.sciencemag.org/content/356/6338/eaal3118.full.DOI: 10.1126/science.aal3118.

71. **Jung Y, Riven I, Feigelson SW, Kartvelishvily E, Tohya K, Miyasaka M, Alon R, *et al.*** Three-dimensional localization of T-cell receptors in relation to microvilli using a combination of superresolution microscopies. *Proc. Natl. Acad. Sci. U. S. A.* 2016; **113**:E5916–E5924. Available at: http://www.ncbi.nlm.nih.gov/pubmed/27647916.DOI: 10.1073/pnas.1605399113.

72. **Cavanagh LL**, **Weninger W**. Dendritic cell behaviour in vivo: lessons learned from intravital two-photon microscopy. *Immunol. Cell Biol.* 2008; **86**:428–38. Available at: http://www.ncbi.nlm.nih.gov/pubmed/18431356 [Accessed April 17, 2013].DOI: 10.1038/icb.2008.25.

73. **Gunzer M, Weishaupt C, Hillmer A, Basoglu Y, Friedl P, Dittmar KE, Kolanus W, *et al.*** A spectrum of biophysical interaction modes between T cells and different antigen-presenting cells during priming in 3-D collagen and in vivo. *Blood*. 2004; **104**:2801–9. Available at: http://www.ncbi.nlm.nih.gov/pubmed/15256430 [Accessed October 22, 2013].DOI: 10.1182/blood-2004-03-1193.

74. **Bousso P**. T-cell activation by dendritic cells in the lymph node: lessons from the movies. *Nat. Rev. Immunol.* 2008; **8**:675–84. Available at: http://www.ncbi.nlm.nih.gov/pubmed/19172690 [Accessed May 27, 2013].DOI: 10.1038/nri2379.

75. **Mempel TR**, **Henrickson SE**, **Von Andrian UH**. T-cell priming by dendritic cells in lymph nodes occurs in three distinct phases. *Nature*. 2004; **427**:154–9. Available at: http://www.ncbi.nlm.nih.gov/pubmed/14712275.DOI: 10.1038/nature02238.

76. **Celli S**, **Lemaître F**, **Bousso P**. Real-Time Manipulation of T Cell-Dendritic Cell Interactions In Vivo Reveals the Importance of Prolonged Contacts for CD4+ T Cell Activation. *Immunity*. 2007; **27**:625–634.DOI: 10.1016/j.immuni.2007.08.018.

77. **Brossard C**, **Feuillet V**, **Schmitt A**, **Randriamampita C**, **Romao M**, **Raposo G**, **Trautmann A**. Multifocal structure of the T cell - dendritic cell synapse. *Eur. J. Immunol.* 2005; **35**:1741–53. Available at: http://www.ncbi.nlm.nih.gov/pubmed/15909310 [Accessed March 1, 2013].DOI: 10.1002/eji.200425857.

78. **Fisher PJ**, **Bulur P a**, **Vuk-Pavlovic S**, **Prendergast FG**, **Dietz AB**. Dendritic cell microvilli: a novel membrane structure associated with the multifocal synapse and T-cell clustering. *Blood*. 2008; **112**:5037–45. Available at: http://www.ncbi.nlm.nih.gov/pubmed/18805966 [Accessed April 9, 2013].DOI: 10.1182/blood-2008-04-149526.

79. **Cai E, Marchuk K, Beemiller P, Beppler C, Rubashkin MG, Weaver VM, Gérard A, *et al.*** Visualizing dynamic microvillar search and stabilization during ligand detection by T cells. *Science*. 2017; **356**. Available at: http://www.ncbi.nlm.nih.gov/pubmed/28495700.DOI: 10.1126/science.aal3118.

80. **Al-Alwan MM**, **Liwski RS**, **Haeryfar SM**, **Baldridge WH**, **Hoskin DW**, **Rowden G**, **West KA**. Cutting edge: dendritic cell actin cytoskeletal polarization during immunological synapse formation is highly antigen-dependent. *J. Immunol. (Baltimore, Md 1950)*. 2003; **171**:4479–4483. Available at: papers://83acc47a-068c-4c1c-ab9f-591275e2fa6d/Paper/p1005.

81. **Benvenuti F, Hugues S, Walmsley M, Ruf S, Fetler L, Popoff M, Tybulewicz VLJ, *et al.*** Requirement of Rac1 and Rac2 expression by mature dendritic cells for T cell priming. *Science*. 2004; **305**:1150–3. Available at: http://www.ncbi.nlm.nih.gov/pubmed/15326354 [Accessed March 20, 2013].DOI: 10.1126/science.1099159.

82. **Pulecio J, Petrovic J, Prete F, Chiaruttini G, Lennon-Dumenil A-M, Desdouets C, Gasman S, *et al.*** Cdc42-mediated MTOC polarization in dendritic cells controls targeted delivery of cytokines at the immune synapse. *J. Exp. Med.* 2010; **207**:2719–32. Available at: http://www.pubmedcentral.nih.gov/articlerender.fcgi?artid=2989776&tool=pmcentrez&rendertype=abstract [Accessed March 20, 2013].DOI: 10.1084/jem.20100007.

83. **Chiaruttini G, Piperno GM, Jouve M, De Nardi F, Larghi P, Peden AA, Baj G, *et al.*** The SNARE VAMP7 Regulates Exocytic Trafficking of

Interleukin-12 in Dendritic Cells. *Cell Rep.* 2016; **14**:2624–2636.DOI: 10.1016/j.celrep.2016.02.055.

84. **Tanizaki H, Egawa G, Inaba K, Honda T, Nakajima S, Moniaga CS, Otsuka A, *et al.*** Rho-mDia1 pathway is required for adhesion, migration, and T-cell stimulation in dendritic cells. *Blood*. 2010; **116**:5875–84. Available at: http://www.ncbi.nlm.nih.gov/pubmed/20881208 [Accessed April 17, 2013].DOI: 10.1182/blood-2010-01-264150.

85. **Pulecio J**, **Tagliani E**, **Scholer A**, **Prete F**, **Fetler L**, **Burrone OR**, **Benvenuti F**. Expression of Wiskott-Aldrich syndrome protein in dendritic cells regulates synapse formation and activation of naive CD8+ T cells. *J. Immunol.* 2008; **181**:1135–42. Available at: http://www.ncbi.nlm.nih.gov/pubmed/18606666.

86. **Bouma G**, **Mendoza-Naranjo A**, **Blundell MP**, **de Falco E**, **Parsley KL**, **Burns SO**, **Thrasher AJ**. Cytoskeletal remodeling mediated by WASp in dendritic cells is necessary for normal immune synapse formation and T-cell priming. *Blood*. 2011; **118**:2492–501. Available at: http://www.ncbi.nlm.nih.gov/pubmed/21690559 [Accessed March 14, 2013].DOI: 10.1182/blood-2011-03-340265.

87. **Malinova D, Fritzsche M, Nowosad CR, Armer H, Munro PMG, Blundell MP, Charras G, *et al.*** WASp-dependent actin cytoskeleton stability at the dendritic cell immunological synapse is required for extensive, functional T cell contacts. *J. Leukoc. Biol.* 2016; **99**:699–710. Available at: http://www.jleukbio.org/cgi/doi/10.1189/jlb.2A0215-050RR.DOI: 10.1189/jlb.2A0215-050RR.

88. **Comrie WA**, **Li S**, **Boyle S**, **Burkhardt JK**. The dendritic cell cytoskeleton promotes T cell adhesion and activation by constraining ICAM-1 mobility. 2015:457–473.DOI: 10.1083/jcb.201406120.

89. **Chen J, Ganguly A, Mucsi AD, Meng J, Yan J, Detampel P, Munro F, *et al.*** Strong adhesion by regulatory T cells induces dendritic cell cytoskeletal polarization and contact-dependent lethargy. *J. Exp. Med.* 2017; **214**:327–338. Available at: http://www.jem.org/lookup/doi/10.1084/jem.20160620.DOI: 10.1084/jem.20160620.

90. **Saito SY**, **Watabe S**, **Ozaki H**, **Fusetani N**, **Karaki H**. Mycalolide B, a novel actin depolymerizing agent. *J. Biol. Chem.* 1994; **269**:29710–29714.

91. **Majstoravich S**, **Zhang J**, **Nicholson-Dykstra S**, **Linder S**, **Friedrich W**, **Siminovitch KA**, **Higgs HN**. Lymphocyte microvilli are dynamic, actin-dependent structures that do not require Wiskott-Aldrich syndrome protein (WASp) for their morphology. *Blood*. 2004; **104**:1396–1403.DOI: 10.1182/blood-2004-02-0437.

92. **Moor H**. *Cryotechniques in biological electron microscopy.* 1987.DOI: OL2393773M.

93. **Ueda H**, **Morphew MK**, **McIntosh JR**, **Davis MM**. CD4+ T-cell synapses involve multiple distinct stages. *Proc. Natl. Acad. Sci. U. S. A.* 2011; **108**:17099–104. Available at: http://www.pubmedcentral.nih.gov/articlerender.fcgi?artid=3193211&tool=pmcentrez

&rendertype=abstract [Accessed August 24, 2013].DOI: 10.1073/pnas.1113703108.

94. **Leithner A, Eichner A, Müller J, Reversat A, Brown M, Schwarz J, Merrin J, *et al.*** Diversified actin protrusions promote environmental exploration but are dispensable for locomotion of leukocytes. *Nat. Cell Biol.* 2016; **18**:1253. Available at: http://dx.doi.org/10.1038/ncb3426.

95. **Roche P a, Furuta K**. The ins and outs of MHC class II-mediated antigen processing and presentation. *Nat. Rev. Immunol.* 2015; **15**:203–216. Available at: http://www.ncbi.nlm.nih.gov/pubmed/25720354.DOI: 10.1038/nri3818.

96. **Furuta K, Ishido S, Roche PA**. Encounter with antigen-speci fi c primed CD4 T cells promotes MHC class II degradation in dendritic cells. 2012:1–6.DOI: 10.1073/pnas.1213868109/-/DCSupplemental.www.pnas.org/cgi/doi/10.1073/pnas.1213868109.

97. **Barnden MJ, Allison J, Heath WR, Carbone FR**. Defective TCR expression in transgenic mice constructed using cDNA-based alpha- and beta-chain genes under the control of heterologous regulatory elements. *Immunol. Cell Biol.* 1998; **76**:34–40.DOI: 10.1046/j.1440-1711.1998.00709.x.

98. **Riedl J, Flynn KC, Raducanu A, Gärtner F, Beck G, Bösl M, Bradke F, *et al.*** Lifeact mice for studying F-actin dynamics. *Nat. Methods*. 2010; **7**:168–169.DOI: 10.1038/nmeth0310-168.

99. **Snapper SB, Rosen FS, Mizoguchi E, Cohen P, Khan W, Liu CH, Hagemann TL, *et al.*** Wiskott-Aldrich syndrome protein-deficient mice reveal a role for WASP in T but not B cell activation. *Immunity*. 1998; **9**:81–91. Available at: http://www.ncbi.nlm.nih.gov/pubmed/9697838.DOI: S1074-7613(00)80590-7 [pii].

100. **Riedl J, Crevenna AH, Kessenbrock K, Yu JH, Neukirchen D, Bradke F, Jenne D, *et al.*** Lifeact: a versatile marker to visualize F-actin. 2008; **5**:605–607.DOI: 10.1038/NMETH.1220.

101. **Lai FPL, Szczodrak M, Block J, Faix J, Breitsprecher D, Mannherz HG, Stradal TEB, *et al.*** Arp2/3 complex interactions and actin network turnover in lamellipodia. *EMBO J.* 2008; **27**:982–92. Available at: http://www.pubmedcentral.nih.gov/articlerender.fcgi?artid=2265112&tool=pmcentrez&rendertype=abstract [Accessed March 1, 2016].DOI: 10.1038/emboj.2008.34.

102. **Renkawitz J, Schumann K, Weber M, Lämmermann T, Pflicke H, Piel M, Polleux J, *et al.*** Adaptive force transmission in amoeboid cell migration. *Nat. Cell Biol.* 2009; **11**:1438–43. Available at: http://www.ncbi.nlm.nih.gov/pubmed/19915557 [Accessed November 16, 2012].DOI: 10.1038/ncb1992.

103. **Schindelin J, Arganda-Carreras I, Frise E, Kaynig V, Longair M, Pietzsch T, Preibisch S, *et al.*** Fiji: An open-source platform for biological-image analysis. *Nat. Methods*. 2012; **9**:676–682.DOI: 10.1038/nmeth.2019.

104. **Cardona A, Saalfeld S, Schindelin J, Arganda-Carreras I, Preibisch S, Longair M, Tomancak P, *et al.*** TrakEM2 software for neural circuit reconstruction. *PLoS One*. 2012; **7**.DOI: 10.1371/journal.pone.0038011.

105. **Diz-Muñoz A**, **Thurley K**, **Chintamen S**, **Altschuler SJ**, **Wu LF**, **Fletcher DA**, **Weiner OD**. Membrane Tension Acts Through PLD2 and mTORC2 to Limit Actin Network Assembly During Neutrophil Migration. *PLoS Biol.* 2016; **14**.DOI: 10.1371/journal.pbio.1002474.

106. **Baranov M V**, **Ter Beest M**, **Reinieren-Beeren I**, **Cambi A**, **Figdor CG**, **van den Bogaart G**. Podosomes of dendritic cells facilitate antigen sampling. *J. Cell Sci.* 2014; **127**:1052–64. Available at: http://www.ncbi.nlm.nih.gov/pubmed/24424029 [Accessed April 15, 2014].DOI: 10.1242/jcs.141226.

107. **Pulecio J**, **Tagliani E**, **Scholer A**, **Prete F**, **Fetler L**, **Burrone OR**, **Benvenuti F**. Expression of Wiskott-Aldrich syndrome protein in dendritic cells regulates synapse formation and activation of naive CD8+ T cells. *J. Immunol.* 2008; **181**:1135–1142.DOI: 10.4049/jimmunol.181.2.1135.